INCLUSIVE DIRECT PHOTON PRODUCTION IN THE CENTRAL AND FORWARD RAPIDITY REGIONS IN PROTON-ANTIPROTON COLLISIONS AT A CENTER OF MASS ENERGY OF 1800 GEV

By

Steven A. Jerger

A DISSERTATION

Submitted to
Michigan State University
in partial fulfillment of the requirements
for the degree of

DOCTOR OF PHILOSOPHY

Department of Physics and Astronomy

1997

ABSTRACT

INCLUSIVE DIRECT PHOTON PRODUCTION IN THE CENTRAL AND FORWARD RAPIDITY REGIONS IN PROTON-ANTIPROTON COLLISIONS AT A CENTER OF MASS ENERGY OF 1800 GEV

By

Steven A. Jerger

A study of isolated direct photon production in proton-antiproton collisions at a center of mass energy $\sqrt{s}$ = 1800 GeV is reported, as measured at the DØ Detector at the Fermilab Tevatron. Cross sections for the central $(0 \le |\eta| \le 0.9)$ and forward $(1.6 \le |\eta| \le 2.5)$ rapidity regions are presented as a function of photon E_T $(15 \text{ GeV} \le E_T \le 150 \text{ GeV})$, and compared with a next-to-leading order QCD calculation. In the central region, the data and theory are consistent in both shape and normalization; however, in the forward region the data are consistently above the theory, especially in the E_T region below ~ 30 GeV. A preliminary measurement of the correlation between the rapidity of the photon and that of the leading jet in the event shows qualitative agreement between the data and the theoretical prediction.

To David and Janice Jerger

ACKNOWLEDGEMENTS

My thanks to my friends: Gian, Kate, Terry, etc... there are too many people who have helped me get through life to make a long list and risk leaving someone out. If you think your name belongs here, past or present, it does. Thanks.

Thanks to Anne Kernan, Steve Wimpenny, and John Ellison at UC Riverside for giving me the chance to get started down this path as an undergraduate, and to Dave, Kevin, and Mike for their teachings which helped me through grad school (and life).

Thanks to Chip, Scotty, Packy, Dean, Bruce, and especially all the kids of the Waubonsie Valley and Neuqua Valley bands - you gave me another home where I could go for a little sanity or insanity, whichever I needed. Hope this explains protons &... stuff.

Thanks to the direct photon group, especially Sal Fahey, who paved the road and looked out for me; and Steve Linn for reminding me I am allowed to sit at the big table with the grownups. Most of all I thank John Womersley, for his guidance and endless patience - while I doubt I could ever match it, he has always defined for me the level of excellence for which I should strive.

Finally, I give my appreciation to my advisor, Bernard G. Pope, for his wisdom and his uncanny ability to remind me of what's really important. I will always remember a big green shamrock on my desk one stressful morning, a symbol of the unfailing support he has given me through thick and thin times for both of us. Thanks, Bernard.

TABLE OF CONTENTS

LIST OF TABLES

LIST OF FIGURES

Chapter 1

Introduction

This thesis presents a measurement of the production of direct photons in proton-antiproton collisions, using the DØ Detector at the Fermilab Tevatron collider. The rate at which single, isolated photons are produced in such collisions is considered over a range of photon energies, and for two separate ranges of photon polar angle. In addition, the structure of direct photon events is considered by measuring the angular correlation between the photon and the other particles in the event. In both cases, the experimental results are compared with theoretical predictions. Direct photon measurements have historically played a role in the modeling of the Strong force which binds nuclei together (for a review of early direct photon experiments, see [1]), and this thesis continues that tradition by extending the measurement to the highest photon energies available in the world. As such, this thesis serves as an extension to and improvement upon previous DØ direct photon measurements [2][3].

The structure of the thesis is as follows: in Chapter 2, an introduction to basic particle

physics is given, along with a brief explanation of the theory of the Strong force and of the theoretical calculation of direct photon production. Chapter 3 describes the DØ Detector, while Chapter 4 describes the way photons are identified in the detector, as well as the efficiencies with which photons are identified. Chapter 5 presents a discussion of the backgrounds to the direct photon signal, and describes the method by which the level of photon signal was determined. Finally, Chapter 6 presents the results of the measurement of the direct photon production rate, while Chapter 7 presents results from a study of direct photon event structure. The results are summarized in Chapter 8.

The reader will note that extensive use is made of Appendices. This is done in order to avoid excessive detail during the description of the measurement; however, it also serves to partition detailed subjects, so that the Appendices may be more useful to those who may use this thesis as a reference.

Chapter 2

Theory

2.1 The Standard Model

In order to set the framework to which the study of direct photons contributes, we briefly consider the known elementary particles and the forces which govern their interactions. This set of particles, their antiparticle counterparts, and the physical laws they obey are known as the Standard Model. As its name implies, the Standard Model is a stable and consistent structure which has developed over time, and which explains most of the fundamental behavior of particles and forces quite well.

In the Standard Model, all matter is composed of point-like particles which have half-integer values of spin. These are classified as *fermions*, and can be further divided into the *lepton* (Table 2.1) and *quark* families (Table 2.2) [4]. Both the lepton and quark families can be grouped into three "generations," each generation having identical properties except for mass. The reason for these generations is still unknown - most matter in the

Table 2.1: The three generations of leptons.

Particle	Symbol	Charge	Mass (MeV/c^2)
electron	e	-1	0.511
electron neutrino	ν_e	0	< 5.10 E-6
muon	μ	-1	105.6
muon neutrino	ν_μ	0	< 0.17
tau	τ	-1	1777
tau neutrino	ν_τ	0	< 24

Table 2.2: The three generations of quarks.

Particle	Symbol	Charge	Mass (MeV/c^2)
up	u	+2/3	2-8
down	d	-1/3	5-15
charm	c	+2/3	1000-1600
strange	s	-1/3	100-300
top	t	+2/3	180000
bottom	b	-1/3	4100-4500

universe appears to be composed of particles from the first generation: up and down quarks combine to form protons (*uud*) and neutrons (*uud*) that make up the nuclei of atoms; and electrons orbit the nuclei, giving atoms their chemical and material properties.

Governing how these particles interact are the four known forces: the Electromagnetic, Weak, and Strong forces and the Gravitational force. Each of these forces is mediated by a spin 1 particle, classified as a *boson*; the bosons are listed in Table 2.3. Particles with

Table 2.3: Vector bosons and the forces they mediate.

Boson	Symbol	Force	Charge	Mass (MeV/c^2)
photon	γ	Electromagnetic	0	0
W	W	Weak	± 1	80300
Z	Z	Weak	0	91187
gluon	g	Strong	0	0
graviton	?	Gravity	?	?

electric charge interact through the Electromagnetic force and its carrier, the photon; Weak interactions proceed through exchange of W or Z bosons. In very high energy interactions, where the mass of the W or Z becomes negligible, the Electromagnetic and Weak force are actually the same; therefore, the two forces are treated theoretically as two aspects of one Electroweak force. While the Gravitational force was known before any of the other forces, there is as yet no well-developed quantum theory of Gravity, and therefore no standard Gravitational boson.

The Strong force acts between quarks - for example, it is the Strong force which holds the nucleus of an atom together. The Strong force is mediated by the gluon, and introduces a new type of quantum number called color, analogous to Electromagnetic charge but with three facets rather than the one of electromagnetism. Thus, quarks can be "red", "green" or "blue" (or antired, antigreen, or antiblue), and gluons carry these characteristics in color-anticolor pairs in order to exchange color between two quarks. Note that this is markedly different than in Electromagnetism, where photons do not carry charge themselves. Also,

only colorless particles are allowed to exist free in nature - therefore, quarks only exist in quark-antiquark states called *mesons* (in which color charges cancel) and in three quark states (such as protons or neutrons) called *baryons* (in which red, green, and blue form a colorless combination). Note that these groupings also eliminate the possibility of states with fractional charge. The more general term *hadron* is used to refer to any particle composed of quarks, whether meson or baryon.

Historically, the framework of the Standard Model was laid out during the 1960's and 1970's [5], with experimental evidence accumulating in the following decades which confirmed the model [6]:

- experimental evidence of point-like scattering centers inside nucleons, which led to the association with quarks (1969) [7]
- observation of weak interactions through the exchange of a Z boson (1973) [8]
- observation of the charm and bottom quarks (1974, 1977) [9]
- observation of jet structure and gluon radiation (1979) [10]
- direct observation of the W and Z bosons (1983) [11]
- observation of the top quark (1995) [12]

Increasingly precise measurements of particle properties and interactions have followed these discoveries, as physicists seek not only to confirm the building blocks of the model, but also to refine and extend our understanding of how those building blocks interact.

2.2 QCD Interactions

While the theory of the Electromagnetic force, known as Quantum Electrodynamics (QED), is now well understood and well tested experimentally, the equivalent theory for the Strong force, Quantum Chromodynamics (QCD), is less completely understood, and is thus a very active theoretical field. This thesis studies the production of direct photons in proton-antiproton (i.e., hadron-hadron) collisions - interactions involving the Strong force. Thus it is important to consider the workings of QCD in more detail.

If we consider a proton-antiproton collision, we might imagine a very complicated picture. We have essentially a bag of three quarks interacting with another bag of three (anti)quarks, all the while exchanging gluons as necessary for the quarks to stay bound together. While these gluons generally have only a small amount of the momentum of the proton, they are plentiful. In addition, because of the quantum nature of QCD, some number of quark-antiquark pairs (called *sea* quarks) are being created and then annihilated from the vacuum in addition to the 3 *valence* quarks. How do we keep track of all that goes on between all these different particles?

The answer lies in one of the more curious aspects of the Strong force. Because the gluons carry color, and thus couple to themselves, the strength of the Strong force (expressed as the coupling constant of the Strong force, α_s) actually gets weaker as the energy of the collision gets higher (or alternatively, the distance scale gets shorter). This is the reverse of everyday experience, such as in Electromagnetism or Gravity where increased energy (shorter distance) means a stronger effect. This can be roughly imagined by considering that since the gluons can couple to themselves, they can emit other gluons

which increase the color force. Thus the quicker and shorter the interaction, the less chance there is for gluons to radiate, and the smaller the strength of the field.

Using this fact, known as *asymptotic freedom*, we are therefore free to consider the collision between a proton and an antiproton as an interaction between one component quark or gluon (generically called a *parton*) of each. Also, we can use the methods of perturbation theory to calculate the interaction in orders of α_s, since at higher energies α_s becomes small enough to decrease the importance of higher orders. Generally we calculate a *cross section* (σ), measured in units of area, which indicates how likely it is that a given interaction will occur; this is analogous to the classical cross section, where a larger surface area with which to collide means a larger chance of a collision.

In order to give an overview of the process, consider the sample interaction shown in Figure 2.1, in which a quark and a gluon (or more generally, two partons) collide to produce a photon and a quark (or parton). Looking first at the center of the figure, we see the "hard scattering" part of the calculation. Here we consider just the two partons scattering off each other - to calculate the cross section for photon production perturbatively, we consider all the possible outcomes involving a photon and partons. To leading order, this is simply a photon plus a single parton. Notice, however, that we might also have a gluon radiated off the final state parton (shown as "jet 2"); this requires another strong interaction, and hence another factor of α_s. We must continue to sum such possible higher order terms, as well as sum over all the different quark/gluon types which the "partons" might specifically be, and integrate over all possible parton momenta in order to produce a total cross section.

However, because of the complexity of the calculation, it is not possible to sum to all

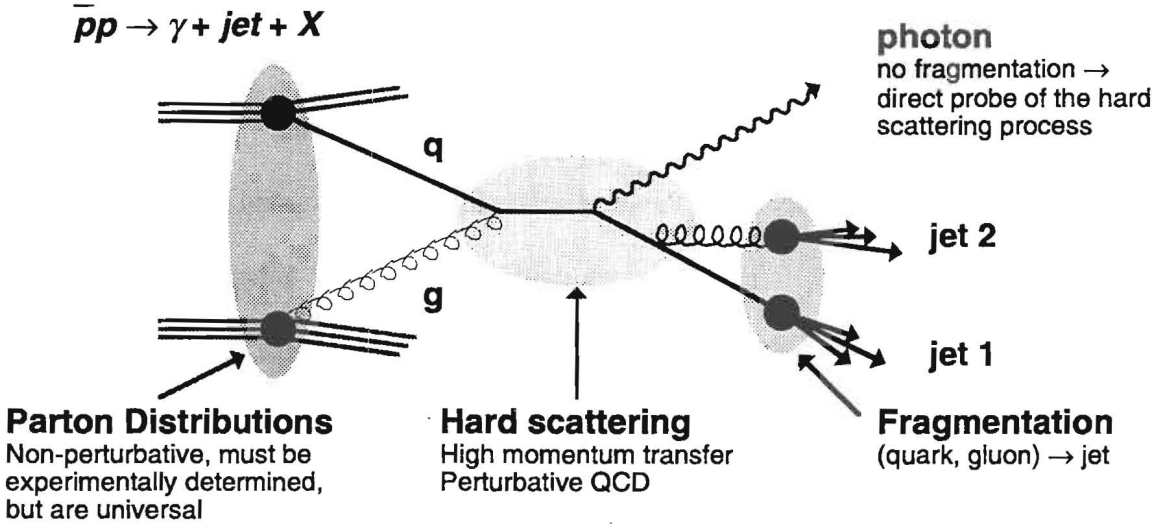

Figure 2.1: Diagram picturing different aspects of a QCD interaction.

orders - as a result, infinities in the momentum integration no longer cancel, leading to unphysical results. To resolve this problem, a mathematical method known as *renormalization* is used, which neatly removes the infinities, but at the price of introducing an arbitrary momentum scale μ_R (the renormalization scale). It is important to note that μ_R is an artificial, non-physical parameter which appears in the result of the calculation only because we cannot complete the calculation to all orders. We choose this scale to be roughly the order of the produced photon momentum, representative of the scale of the interaction; however, we expect that the dependence of our result on μ_R will be minimized if we have carried the calculation to high enough order.

Given this method of calculating the hard scattering, we can expand our consideration to the left side of Figure 2.1 - namely, if we collide a proton and antiproton, what is the likelihood that two partons of a given momentum will be available to interact? These directly affect the perturbative calculation, since we need to know how often each parton combination that we enumerated above might occur. Also, we need to know what fraction x of the proton's momentum each of these partons is likely to have, so that we can integrate over momentum properly. Unfortunately, these are exactly the quantities which we cannot calculate in perturbative QCD, as they deal with the relatively low energy structure of the proton.

In order to continue the calculation, then, we must make one further assumption. We assume that the part of the calculation which specifies the parton densities and momenta can be separated from the hard scattering part - this is known as *factorization*. Given this assumption, we can replace the non-perturbative portion of the theory with experimentally

determined functions which describe the quark and gluon content of the proton - the parton distribution functions (PDFs). These PDFs can then be considered universal - they can be applied to any process which requires knowledge of the content of the proton. However, to implement this separation in the calculation, we must use a mathematical method similar to that used in renormalization - hence we introduce another (unphysical) factorization scale μ_F, on which the PDFs are dependent. As in the case of μ_R, we choose μ_F approximately equal to the photon momentum to set the scale of the interaction; however, it is important to note that the two scales need not be exactly the same, as they have independent origins.

With an understanding of the PDFs and the perturbative hard scattering, we can finally consider the right side of Figure 2.1. In enumerating the outcomes of a hard scattering, we must consider what happens to the outgoing partons, as we know they cannot remain free because they are not colorless. Here again the nature of the Strong force comes into play: because the Strong force grows stronger with distance, as the outgoing parton gets farther away from the interaction the color force between it and the parent hadron increases. Ultimately, enough energy builds up to create one or more quark-antiquark pairs from the vacuum - these quarks then combine to form colorless hadrons. This process is called *hadronization* or *fragmentation*, and it results in a collimated "jet" of particles being observed as the final signature of an outgoing parton. Because of this fragmentation process, there is a finite probability of obtaining any given particle from a parton fragmentation which can be expressed in terms of *fragmentation functions*; these functions are also not calculable in perturbative QCD and therefore must be modeled using experimental data. However, like the PDFs, they can be considered universal, and

independent of the nature of the hard scattering process.

Combining these aspects of the calculation, then, we can express the QCD cross section for the process $A + B \rightarrow C + X$ (where X indicates that we do not explicitly keep track of what, other than C, is produced) with the following expression:

$$\sigma(A+B \rightarrow C+X) = \sum_{abcX} \int dx_a dx_b dz_c F_{a/A}(x_a, \mu_F) F_{b/B}(x_b, \mu_F) D_{c/C}(z_c) \times \hat{\sigma}_{ab \rightarrow cX}(x_a, x_b, \mu_R, \mu_F) \qquad (2.1)$$

where a and b are the partons which interact from hadrons A and B; c is the parton which gives rise to C; the F are the parton distribution functions which describe the likelihood of getting a and b (with momentum fractions x_a and x_b) from A and B; D is the fragmentation function which describes the probability of getting C from c with some fraction z_c of c's momentum; and $\hat{\sigma}$ is the partonic hard scattering cross section, implicitly summed to some order in α_s.

Note that in the specific case of photon production (as illustrated in Figure 2.1), the final state photon is free of the complication of fragmentation ($D_{c/\gamma} = 1$). The photon is seen in the final state exactly as it was produced, directly from the parton level interaction. This is an important advantage of the study of direct photon production. In contrast, the study of jet production suffers from ambiguities in reconstructing a parton from the spray of hadrons; also, because of the fluctuations in hadronization, the measured energy of jets can be uncertain because the exact particle composition of any given jet is not known.

2.3 Direct Photon Theory

The study of direct photons thus provides experimentalists with a unique and useful tool with which to test QCD. The mechanisms by which they are produced, as described by QCD theory, imply a direct sensitivity to the gluon distribution of the proton. Also, the characteristics of the final state particles that emerge in a direct photon event, including the ease and precision with which one can identify and measure a photon experimentally, provide a practical advantage.

2.3.1 Direct Photon Diagrams

Consider the examples of leading order direct photon production shown in Figure 2.2. We

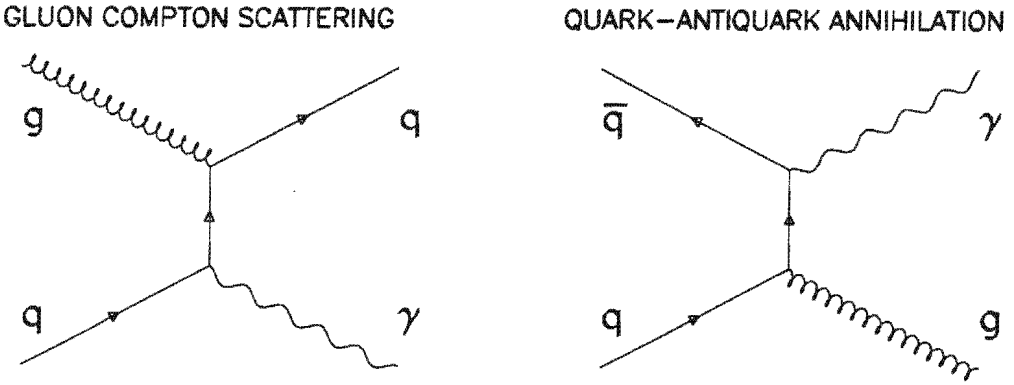

Figure 2.2: Leading order diagrams for direct photon production.

see that photons can be produced in quark-antiquark annihilation, in which the direct photon is produced along with an outgoing gluon. Another process is the QCD analogue to Compton scattering, in which a quark scatters from a gluon, producing a photon in the final state along with the scattered quark. Because of the relative abundance of low x gluons in the proton, this process is the dominant form of direct photon production for E^{γ}_{T} below ~ 100 GeV; above this, the (typically) larger momentum fractions of quarks are necessary to produce such an energetic photon, and the annihilation diagram becomes more prominent. Because of the Compton dominance, we expect a measurement of direct photon production to have sensitivity to the gluon content of the proton.

Some examples of higher order photon production diagrams are shown in Figure 2.3. These typically involve additional gluon radiations, and result in characteristic signatures of a photon plus two or more jets. Current direct photon QCD calculations include only up to the two jet level (order α_s^2), known as next-to-leading order (NLO), whereas the experimental measurement includes all orders unless an explicit cut is made, and is therefore termed *inclusive*. However, if terms beyond NLO are small, the NLO prediction should be a good approximation to the inclusive cross section.

2.3.2 Bremsstrahlung Component and Isolation

As shown in Figure 2.4, there is another source of single photons: bremsstrahlung from an outgoing quark in a dijet event. In this case, the photon is not produced directly from the interaction vertex, and is therefore not really a "direct" photon - however, the existence of this production method affects the way direct photons are measured and modeled

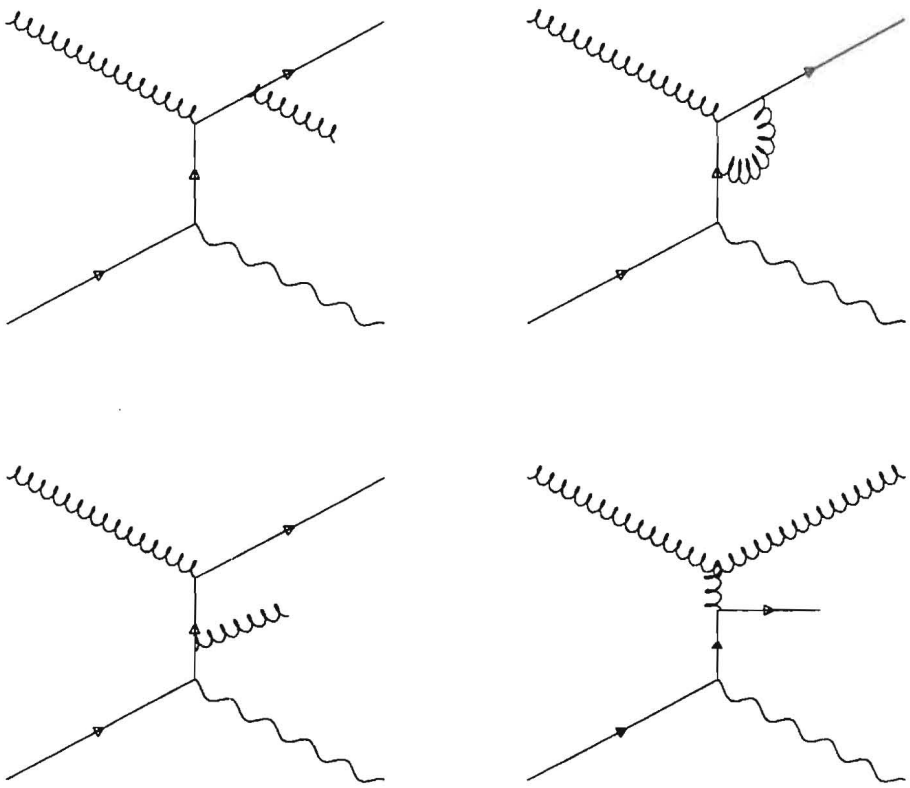

Figure 2.3: Examples of higher order direct photon diagrams.

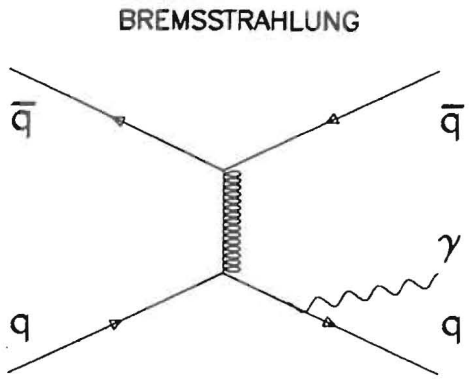

Figure 2.4: Photon production through Bremsstrahlung

theoretically, as described in the next section. This method of production can be described using the probability that a quark fragments primarily to a photon - $D_{q/\gamma}$.

In order to reduce the occurrence of the bremsstrahlung case, an isolation criterion is imposed on the photon: typically, a cone around the photon is examined and required to have less than a certain amount of energy. Since a photon produced through bremsstrahlung tends to be very collinear with the quark it radiates from (and thus the jet resulting from the quark's subsequent fragmentation), the requirement that the photon be isolated removes all but the very largest angle radiations. In the theoretical model, a bremsstrahlung/fragmentation component is added into the calculation and then (partially) removed by the imposition of an isolation requirement matching that of experiment. This component contributes a large (up to 50%) fraction of the total (un-isolated) rate, and remains significant in the E_T region below ~ 25 GeV even after the isolation criterion is applied [13][14].

Another important reason to include an isolation criterion is the possibility that a jet might be misidentified as a photon. In the process by which a parton fragments into observable particles, if most of the parton energy remains with a single particle (for example, a π^0 meson) and that particle produces photons as its decay products (e.g., $\pi^0 \rightarrow \gamma\gamma$), the multiple photons can be indistinguishable from a single photon. While only one in 10^3-10^4 jets fragments in this way, the dijet production cross section is 10^3-10^4 times larger than the photon cross section; therefore this background to the direct photon signal is of the same magnitude as the signal itself. The experimental challenges and solutions involved in removing this background are a major part of any direct photon analysis, and are described in Chapter 5.

2.4 Variables for Hadron Collider Physics

It is necessary to define a set of quantities which are used in the study of high energy hadron-hadron collisions. While the standard phase space variables of energy (E), momentum ($\vec{p}$), polar angle (θ), and azimuthal angle (ϕ) can be used, the nature of hadron colliders makes the introduction of additional quantities necessary.

An important feature of hadron colliders is that while the hadrons can be given equal and opposite momenta, there is inherent uncertainty in the momenta of the partons which interact. Unlike positron-electron (e^+e^-) colliders, where the two colliding particles and their momenta can be exactly defined, the quark and gluon substructure of the proton implies that we cannot predetermine which partons will interact, and what momentum

they will have (as discussed in Section 2.2). Therefore in the lab (detector) frame, the momenta along the beam axis (defined to be the z direction) will usually not sum to zero, and the system will be Lorentz boosted.

In the transverse (x-y) plane, however, we expect that the final state momenta will cancel, as the initial state transverse momenta are negligible. Therefore, we define the *transverse* momentum and energy:

$$p_T \equiv \sqrt{p_x^{\,2} + p_y^{\,2}} \tag{2.2}$$

$$E_T \equiv \sqrt{E^2 - p_z^{\,2}} \tag{2.3}$$

which become important variables for collider physics. Note that if the particle mass $m \ll E$, or for massless particles such as the photon,

$$E_T = p_T = E\sin\theta \tag{2.4}$$

The Lorentz boost also motivates an alternative to the polar angle θ, which is not Lorentz invariant. Instead, we define the *rapidity* (y):

$$y \equiv \frac{1}{2}\ln\left(\frac{E + p_z}{E - p_z}\right) \tag{2.5}$$

which transforms under a Lorentz boost as $y \to y + [\text{constant}]$, thereby preserving the shape of the rapidity distribution under the boost. Again, if a particle's mass is much less than its energy, we can simplify to form the *pseudorapidity* (η):

$$\eta = -\ln\tan\left(\frac{\theta}{2}\right) \tag{2.6}$$

Thus a pseudorapidity of $\eta = 0$ corresponds to $\theta = 90°$ from the beam (z) direction,

increasing to ∞ ($-\infty$) as the angle grows nearer to the $+z$ ($-z$) direction. Since the condition $m \ll E$ is a good approximation for high energy jets and photons, the pseudorapidity is used almost exclusively, and is often referred to as simply the rapidity.

Finally, since we are interested in measuring a cross section, we consider the rate (R) at which events with a cross section σ (with units of area) occur:

$$R = \sigma L \tag{2.7}$$

where L is the *luminosity* in units of inverse area per second. The luminosity is a measure of beam flux, and is tied to the performance of the accelerator and its ability to focus the colliding beams densely enough to achieve significant event rates for high energy physics processes. Cross sections are typically measured in *barns* (1 barn = 10^{-24} cm^2), with rare events having cross sections of several picobarns (pb) or less; therefore, modern colliders such as the Fermilab Tevatron provide luminosities of up to ~10^{31} cm^{-2}s^{-1}. Integrating over the amount of time the accelerator makes this luminosity available to experiments gives a useful measure of how much data has been taken - the *integrated luminosity*. For the 1994-1995 Tevatron Run 1B, from which the data in this analysis was taken, a total of ~ 100 pb^{-1} of data was accumulated.

Chapter 3

Experimental Apparatus

3.1 Accelerator

The Fermilab Tevatron Collider, located in Batavia, IL, accelerates protons and antiprotons to energies of 900 GeV, making a total of 1.8 TeV of energy available as the particles collide. This makes the Tevatron the most powerful accelerator in the world, and thus, in the particle physics tradition of giving Nature as much energy as possible to see what She will create from it, the premier facility at which to study elementary particles and the forces by which they interact.

While the Fermilab accelerator might be described simply as a huge ring of magnets almost 4 miles in circumference, there are actually several different, increasingly sophisticated stages of acceleration which make the final collision possible (Figure 3.1). Cockroft-Walton generators produce H^- ions which have a small initial kinetic energy; these are then fed into a series of accelerating electric fields known as a linear accelerator,

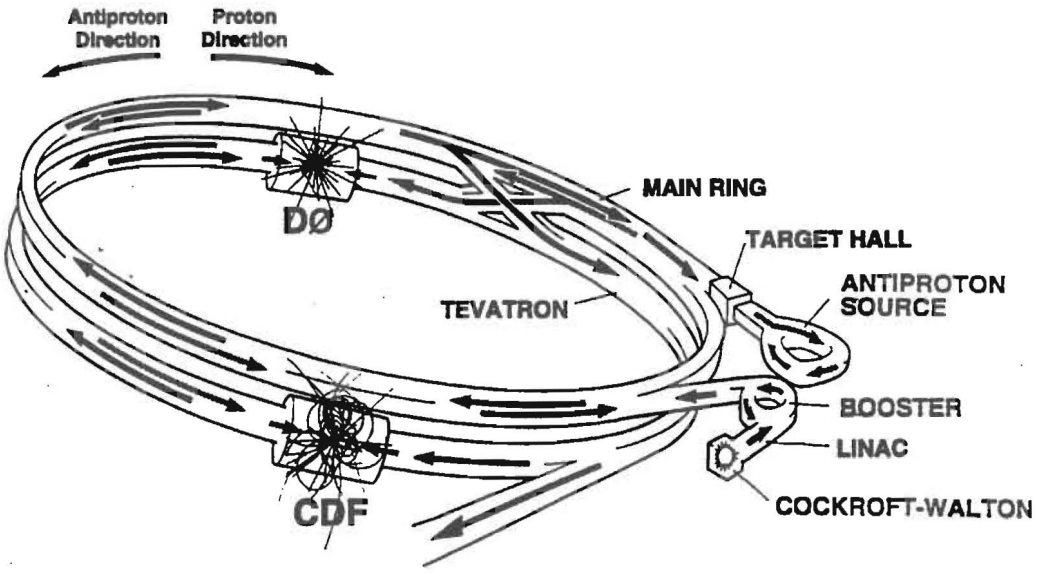

Figure 3.1: The Fermilab Tevatron Collider.

and then stripped of their electrons. The remaining protons are then accelerated further in a small "booster" synchrotron, consisting of a ring of accelerating cavities alternated with magnets to bend the particles, which are also grouped into bunches at this stage. The bunches of protons, by now at an energy of 8 GeV, are then extracted into the Main Ring, so named because it was once itself the final stage of acceleration, giving the protons an energy of 150 GeV. Housed in the same underground tunnel as the Main Ring, however, is its successor the Tevatron, which uses superconducting magnets to produce a magnetic field strong enough to bend even particles of 900 GeV kinetic energy into the necessary circle.

The production of antiprotons takes place by directing some of the protons circulating in the main ring into a target, which produces (among other particles) a small amount of antiprotons. These are carefully selected out, condensed into bunches, stored in a small "accumulator" accelerator, and finally, when a sufficient number have been produced, injected into the Main Ring to circulate in the opposite direction to the protons. This points out a major advantage of colliding protons with antiprotons: the same apparatus can be used to accelerate both sides of the collision, since the two particles are identical but for the opposite charge, which will draw the particles in opposite directions in an electromagnetic field. The two bunches of particles pass through each other without collisions because of the low density of particles within the bunches.

The antiproton bunches are then fed into the Tevatron and ramped up in energy to 900 GeV. The Tevatron operated during Runs 1A (1992-93) and Run 1B (1994-95) with six bunches of each particle circulating within the accelerator, with collisions occurring at two separate interaction points corresponding to the locations of the two detectors (DØ and its sister experiment CDF). At the collision points, focusing magnets are used to squeeze the particle beams down to densities which make collisions sufficiently likely (and thus produce a useful luminosity). The arrangement of particles into bunches means that the collisions take place at definite time intervals as the bunches cross each other - this allows the detector to synchronize with this time cycle so that the readout electronics have sufficient and uniform time intervals to process one bunch crossing and prepare for the next. During Run 1 this time between beam crossings was 3.5 μs; the average number of collisions per bunch crossing varied as a function of the luminosity from ~0.5 to over 3.0 interactions/crossing.

In practice, the accelerator runs in cycles called "stores" - at the beginning of each store, the particles are injected into the Tevatron bunch by bunch, the beam is "scraped" (particles with very off-center orbits are removed), and collisions begin. At this point the luminosity of the collider is at its highest - as the store progresses, luminosity decreases as particles are lost by attrition from collisions and unstable orbits. After about 8-15 hours the available luminosity is too low to be useful, and the store is ended by dumping the particles into a "beam stop," and a new store is readied.

3.2 Detector

The DØ detector is a multi-purpose apparatus, designed with the physics possibilities of the Tevatron in mind. The goal of studying high-P_T phenomena and high-mass states such as the W and Z bosons, as well as the search for the top quark, led to design emphasis on electron and muon identification and measurement; high-P_T jet energy measurement; and accurate accounting of missing transverse energy.

The detector is shown in Figure 3.2. It consists of three main sections: the central tracking detectors, which lie close to the beamline and detect ionization left by particles as they travel from the interaction point outward; the liquid argon sampling calorimeter, which stops most particles and measures their deposited energy; and the muon detection system, which surrounds the calorimeter and provides identification and momentum measurement of muons. A full description of these systems can be found in [15]; a brief description is presented below, with particular emphasis on the tracking detectors and calorimeter, which are the systems used in this analysis.

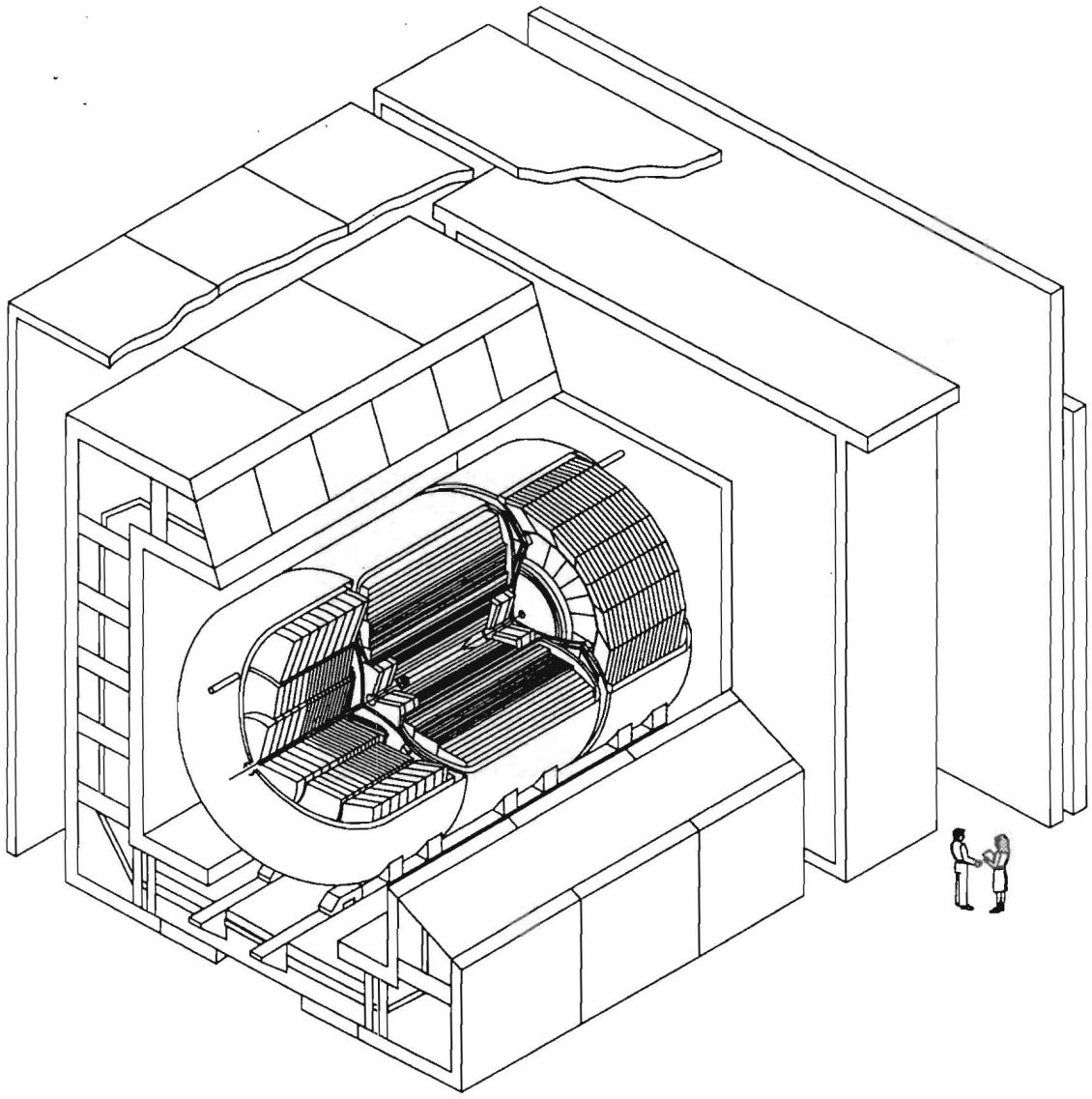

Figure 3.2: The DØ Detector.

3.2.1 Tracking

The DØ Tracking System (Figure 3.3) consists of three subsystems, each providing

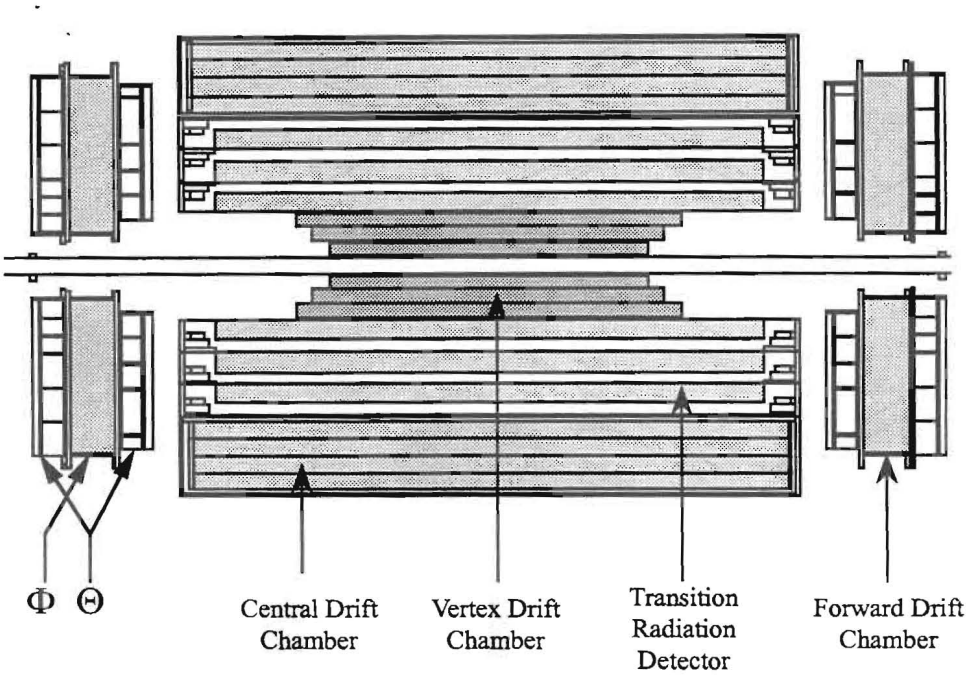

Figure 3.3: The D0 Tracking System.

different information as the distance from the interaction point increases. The Vertex Detector (VTX), which surrounds the beampipe over the range $-2.0 < \eta < 2.0$, provides fine resolution of tracks very close to the interaction point. The Transition Radiation Detector (TRD) surrounds the vertex detector, covering the range $-1.2 < \eta < 1.2$, and

provides discrimination between electrons and charged pions. The Central and Forward Drift Chambers (CDC/FDC) give a measurement of charged tracks further away from the interaction point, where they are more physically separated; the CDC surrounds the TRD, while the FDC extends the tracking coverage down to $\eta = 3.1$.

The Vertex Chamber

The DØ Vertex Detector, like the CDC and FDC, is a drift chamber, designed to detect the ionization left behind as a high-energy charged particle passes through a medium and Coulomb scatters with atomic electrons. As the name implies, this type of detector consists of a "chamber" containing a medium to be ionized (usually a gas, which allows for easy movement of the ionized electrons), and a scheme by which an electromagnetic field is applied to the medium in order to "drift" the ionized electrons to collection points, these points being organized to provide spatial information on the path of the charged particle.

The Vertex detector (Figure 3.4) consists of 3 cylindrical chambers, concentrically layered such that the inner radius of the first layer is just outside of the beampipe at $r = 3.7$ cm, and the outer radius of the last layer is at 16.2 cm. The actual walls between each chamber are constructed of carbon fiber support tubes, and the chambers are filled with a mixture of carbon dioxide (95%) and ethane (5%). Each of the layers is segmented in azimuthal angle φ, with the inner layer segmented into 16 cells and the outer layers segmented into 32. As seen in Figure 3.4, the cells are defined by rows of wires, which run the length of the cylinder (in the z direction) under tension, and which provide the carefully shaped electric field. Traces on the carbon fiber tubes provide a cathode which

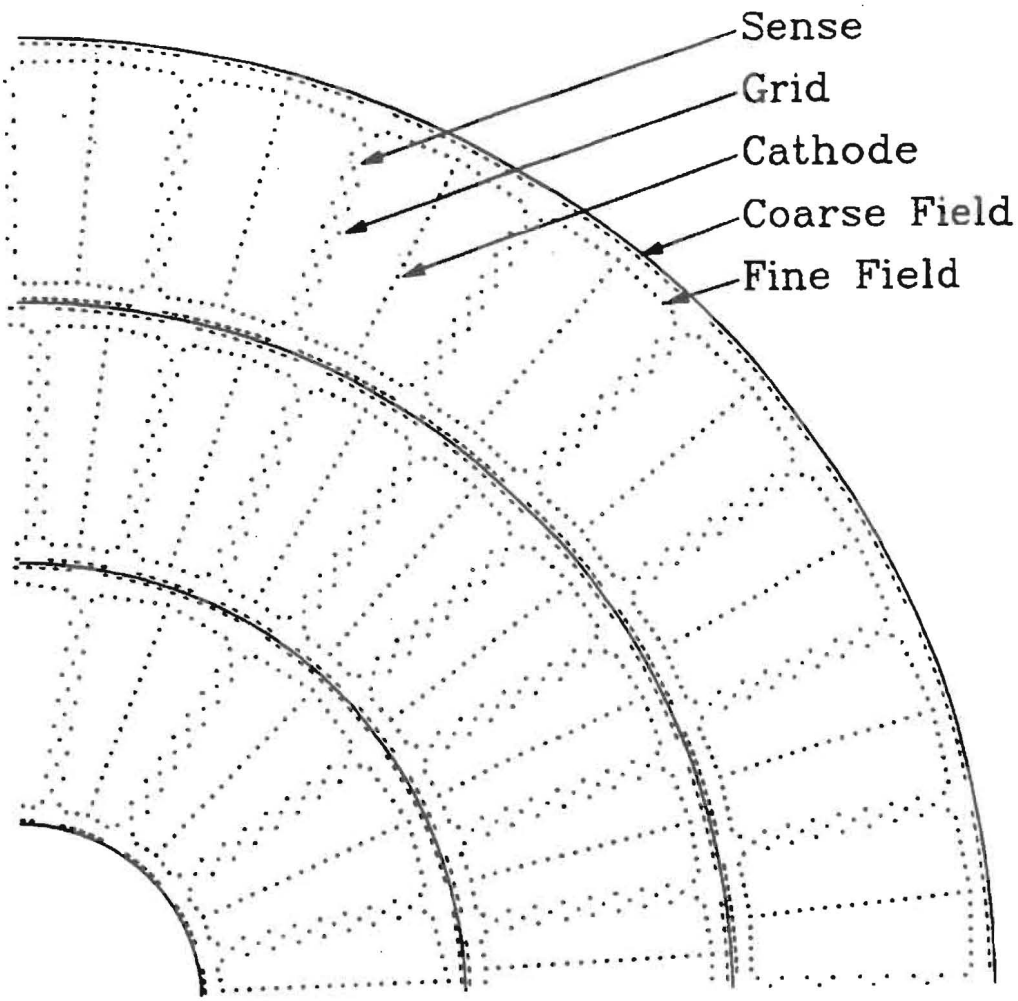

Figure 3.4: Side schematic of the DØ Vertex Detector.

coarsely shapes the field; fine shaping is provided by the cathode wires, and the grounded grid wires serve as anodes to attract ionized electrons to the adjacent sense wires, which read out the accumulated charge. Note that the cell positions in the three layers are staggered in order to improve resolution in the r–ϕ plane, which is typically ~50 μm.

The track position can be determined in the z coordinate by comparing the amount of charge read out at either end of the sense wires, obtaining a z coordinate via charge division. Measuring the z position of tracks is crucial to reconstructing the location of the primary interaction vertex, as well as any secondary vertices due to multiple interactions; knowledge of these vertex positions is used to fix the exact direction of final state particles and therefore measure their production angles and transverse energy components. While the Vertex Detector was designed to achieve a z resolution of ~1 cm, the high track multiplicity environment near the interaction point at Tevatron luminosities has hampered this performance. As a result, the position of the primary vertex is determined with the aid of the Central Drift Chamber.

The Transition Radiation Detector

The Transition Radiation Detector relies on the fact that a charged particle moving at highly relativistic speeds will radiate photons (as X-rays) when it transits between regions with different dielectric constants. The amount of radiation emitted depends on the speed of the particle, which in turn will depend on the energy and mass of the particle. For example, an electron at a certain energy will travel much faster than a π^+ meson with the identical energy, since the π^+ is almost three hundred times more massive than an electron - and as a result the electron will on average emit more transition radiation. It is this

difference which the TRD is designed to exploit.

The TRD, like the VTX chamber, is made up of 3 separate cylindrical units. Each contains foils of polypropylene, 18 μm thick, separated by 150 μm in a volume of nitrogen gas (Figure 3.5). Since the probability of radiation is about 1% per boundary interface [4], there are 393 foils in each unit to insure maximum efficiency. After the foils in each unit there is a drift chamber, which serves to convert the X-rays and read out the ionization signal. Since the drift chamber uses a $Xe(91\%)/CH_4(7\%)/C_2H_6(2\%)$ gas mixture, the drift chamber in each unit is separated from the nitrogen environment of the foil layers by two layers of mylar, between which dry CO_2 gas is circulated to prevent any leakage of gases between the two volumes.

While this analysis does not explicitly use the information read out from the TRD, its presence affects the detection of direct photons. At normal incidence ($\theta = 90°$) the TRD presents 8.1% of a radiation length to a photon; this is most of the material which lies between the interaction point and the calorimeter. As a result, some fraction of photons will convert to an electron-positron pair, and will thereafter leave a pair of ionization tracks. Averaged over the region $-0.9 \leq \eta \leq 0.9$, the probability for such a conversion is roughly 10%, while in the regions corresponding to $1.6 \leq |\eta| \leq 2.5$, where non-normal incidence on the TRD results in greater material depth and the endplates of the VTX and TRD present additional material, the probability rises to about 38% [16]. Therefore, a significant fraction of real photons and jets decaying to photons will convert before the CDC/FDC, and will behave as an e^+e^- pair thereafter.

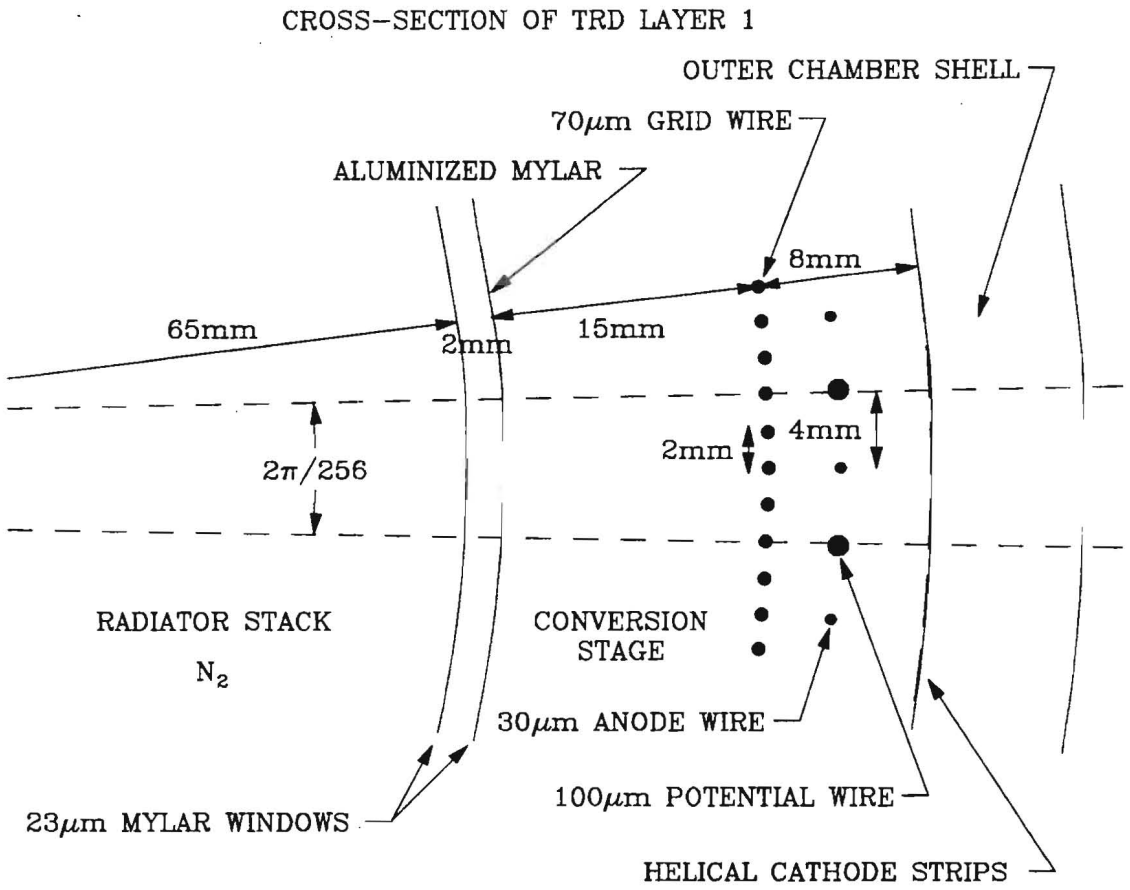

Figure 3.5: Cross section of the first TRD layer.

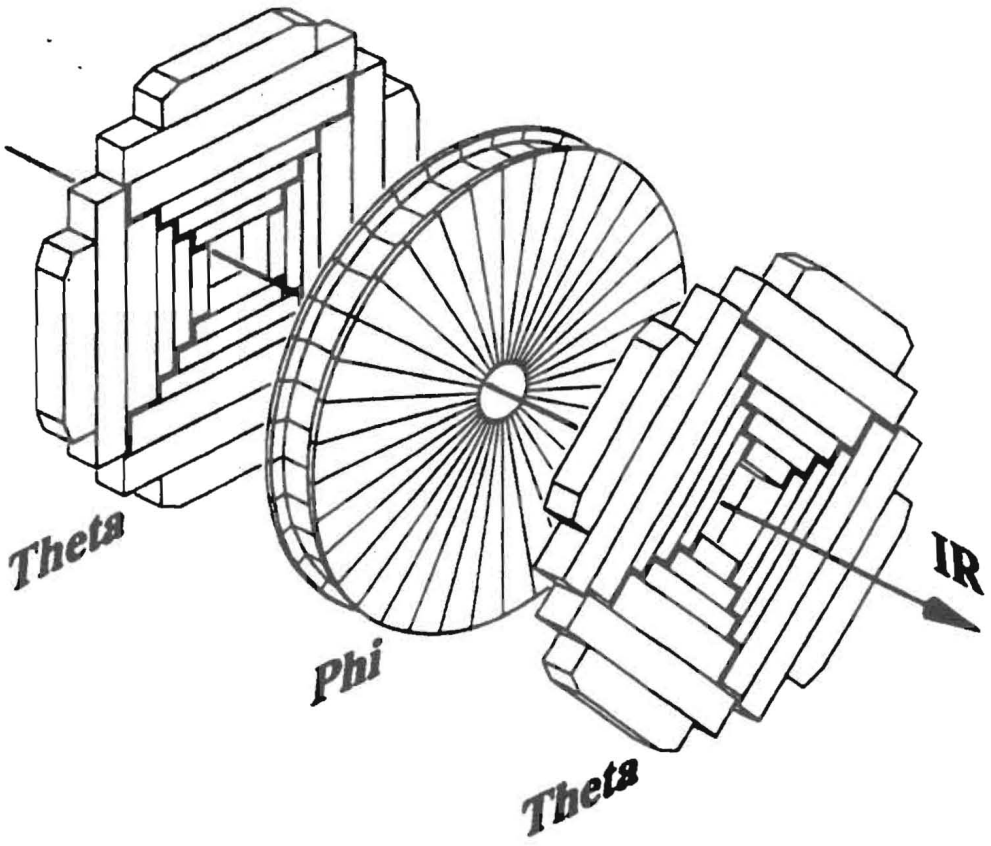

Figure 3.7: An exploded view of the Forward Drift Chamber.

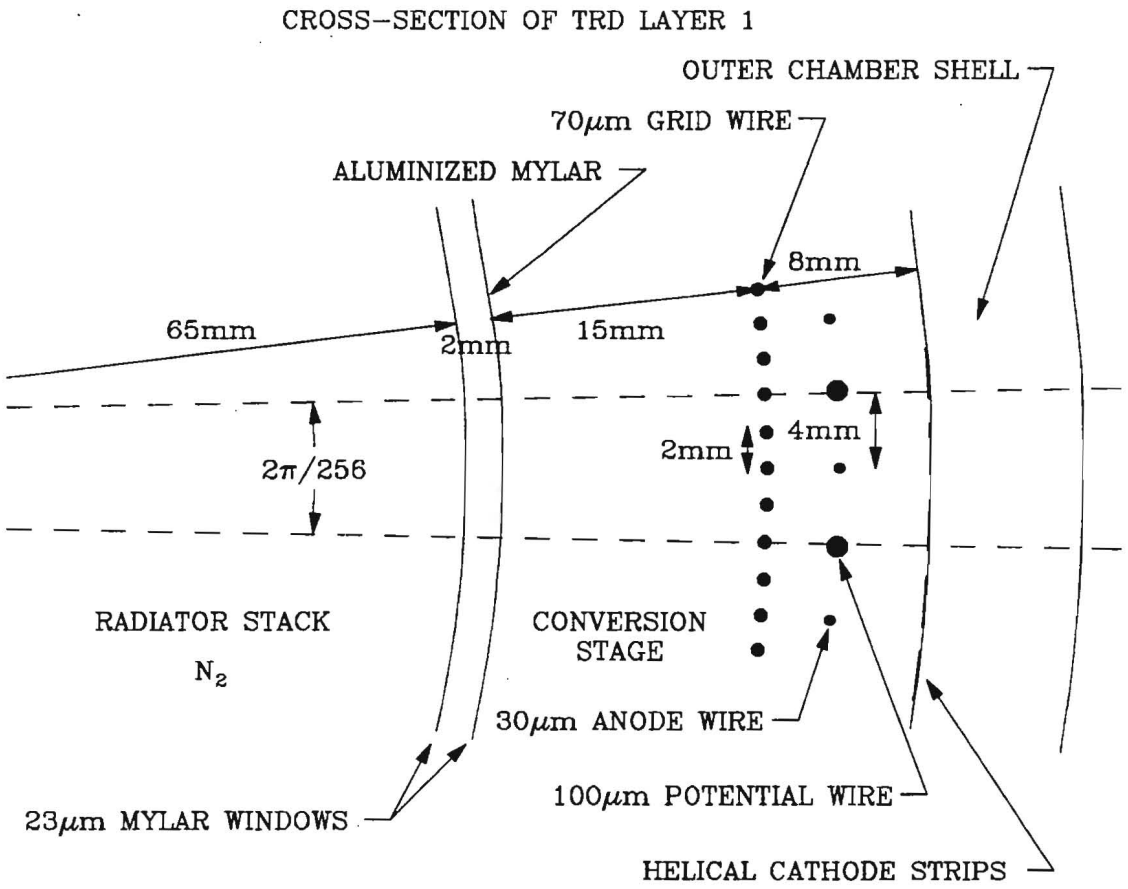

Figure 3.5: Cross section of the first TRD layer.

The Central Drift Chamber

Surrounding the TRD is the Central Drift Chamber, which like the VTX and TRD has a cylindrical shape. As seen in Figure 3.6, the CDC is segmented in azimuthal angle (32

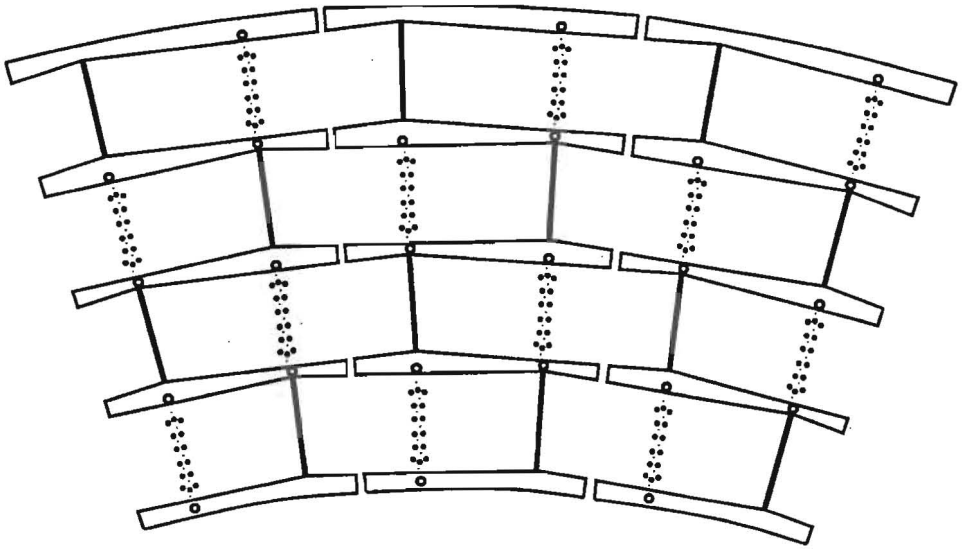

Figure 3.6: End view of a section of the Central Drift Chamber.

cells in all) and is four layers deep, with alternating layers staggered for better coverage. While the physical construction of the cells differs from that of the VTX, with Kapton-covered Rohacell "shelves" defining the physical cell borders, the configuration of sense wires centered in the cell along with surrounding grounded guard wires is similar. In addition to the sense and guard wires, two Teflon coated delay lines run in grooves cut

into the inner and outer shelves of each cell. Signals induced in the delay lines by the nearest sense wires are read out at each end of the CDC, and the comparison of arrival times at the two ends yields a measurement of the z position of the ionization track. The CDC uses an Ar(92.5%)/CH_4(4%)/CO_2(3%) gas mixture.

The Forward Drift Chambers

At smaller angles (closer to the beamline), rather than extending the central detectors, it becomes advantageous to place separate detectors perpendicular to the beamline, so that particles will again impact normally on the detector surface and the z direction extent of the detector can be minimized. The Forward Drift Chambers thus have a different geometry than the CDC: each detector (one on each side of the central region) consists of three disk-like layers (Figure 3.7) oriented perpendicular to the beamline. The first and third layer are constructed of four quadrants of six stacked rectangular cells each, so that each cell covers a different range of angle θ. These two "Θ" layers are rotated by 45° with respect to each other. The middle layer is very different, composed of 36 cells which are like pie wedges, providing discrimination in azimuthal angle ϕ. As in the CDC, though, both "Θ" and "Φ" layers utilize multiple anode and sense wires running along the long dimension of each cell, and several deep in z, to detect the ionization signal. The gas mixture used is also the same as in the CDC. Also, in the "Θ" layers, a single delay line similar to those in the CDC provides a determination of the location of the track along the length of the rectangular cell.

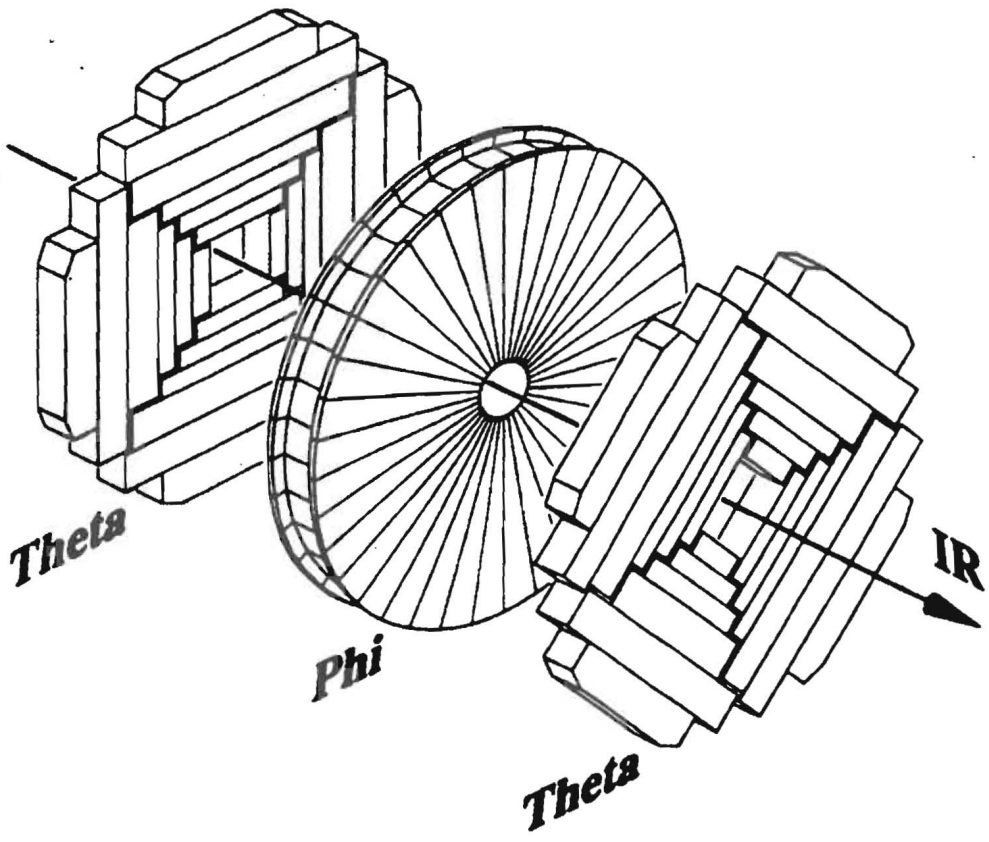

Figure 3.7: An exploded view of the Forward Drift Chamber.

3.2.2 Calorimetry

The DØ Calorimeter System (Figure 3.8) measures the energy of most particles by

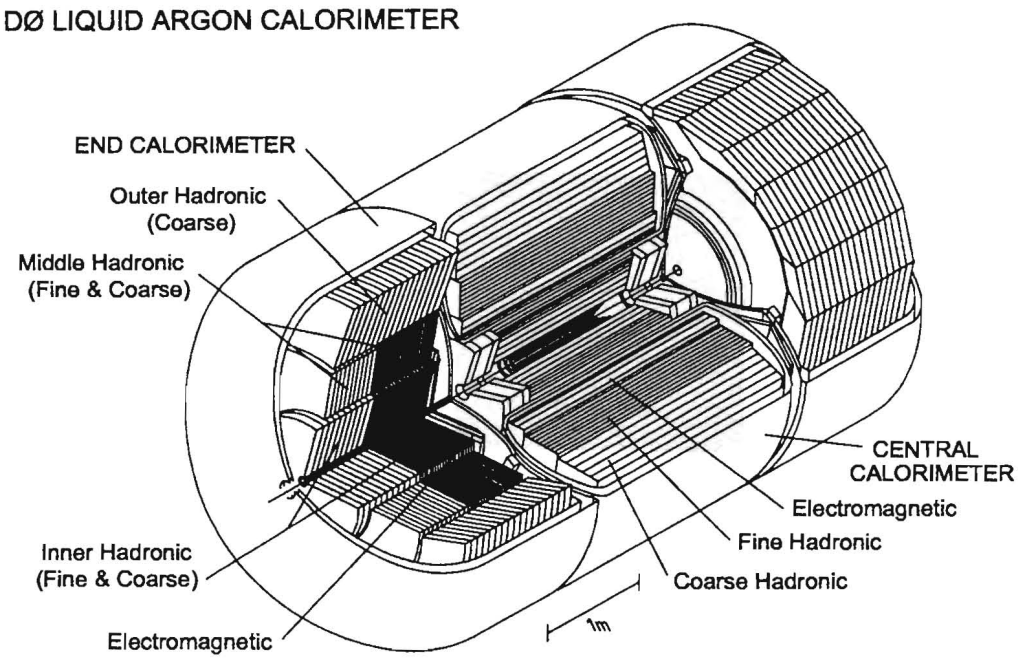

Figure 3.8: The DØ Calorimeter (cutaway view).

stopping them completely within the calorimeter volume, thus transferring the (kinetic) energy of the incident particle to the material in the calorimeter. Accordingly, the calorimeter contains layers of very dense materials (plates of uranium and steel), within which the particles shed their kinetic energy, interspersed with layers of an ionizing

medium from which a signal can be easily measured (liquid Argon). This is therefore a "sampling calorimeter" - since only the ionization left within the Argon layers is read out, only some fraction of the energy (about 10%) is sampled. The total energy deposition is then inferred from this sample by calibrating with particles of known energy in a test beam, and deriving "sampling weights" which multiply the raw energy read out in each layer so that the sum exactly represents the true particle energy. We further expect that readout charge will be proportional to particle energy, so that the calorimeter response will remain linear with increasing energy.

Practically, this layering is achieved by enclosing the dense plates within a cryostatic vessel filled with liquid Argon, so that the Argon-filled gaps between plates become the readout layers. An example of a calorimeter cell implemented this way is shown in Figure 3.9.

As can be seen in Figure 3.8, the calorimeter is separated into one Central and two Endcap sections (North and South), housed in separate cryostats to allow easier access to the interior of the detector. The Central Calorimeter (CC) covers roughly the range $|\eta| \leq 1.0$ and the Endcap Calorimeters (EC) extend the coverage to $|\eta| \approx 4$.

The CC is further segmented radially into 3 sections (Figure 3.10). The Electromagnetic (EM) calorimeter is the section closest to the interaction, and it is read out in 4 separate layers (EM1-EM4) which correspond to 2.0, 2.0, 6.8, and 9.8 radiation lengths, respectively. Most electromagnetic showers from photons and electrons are contained almost completely within these 4 layers, and thus it is the most important part of the calorimeter for this analysis. Beyond the last EM layer, and designed to stop the more penetrating hadronic showers, are the three layers of the Fine Hadronic (FH) section

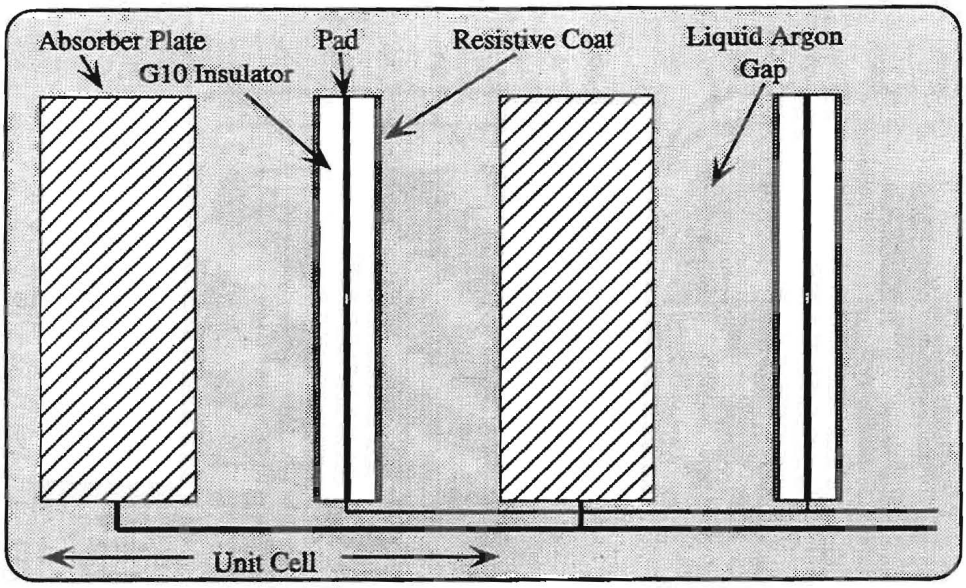

Figure 3.9: Diagram of the layers within a calorimeter cell.

which include 1.3, 1.0, and 0.9 nuclear interaction lengths. Finally, the Coarse Hadronic (CH) section, which uses copper as an absorber rather than uranium, provides one more depth segment of 3.2 nuclear interaction lengths to contain the few hadronic showers which penetrate beyond the EM and FH sections.

The depth segmentation of the EC is similar to that of the CC, with the difference that the hadronic calorimetry is actually broken up into 3 separate sections (concentric about the beampipe) called the Inner (IH), Middle (MH), and Outer (OH) sections, with the IH and MH sections containing both fine (uranium) and coarse (stainless steel) layers of depth similar to the FH and CH in the central region. The OH section contains only coarse layers of stainless steel, as it lies in a region of overlapping coverage with the FH section

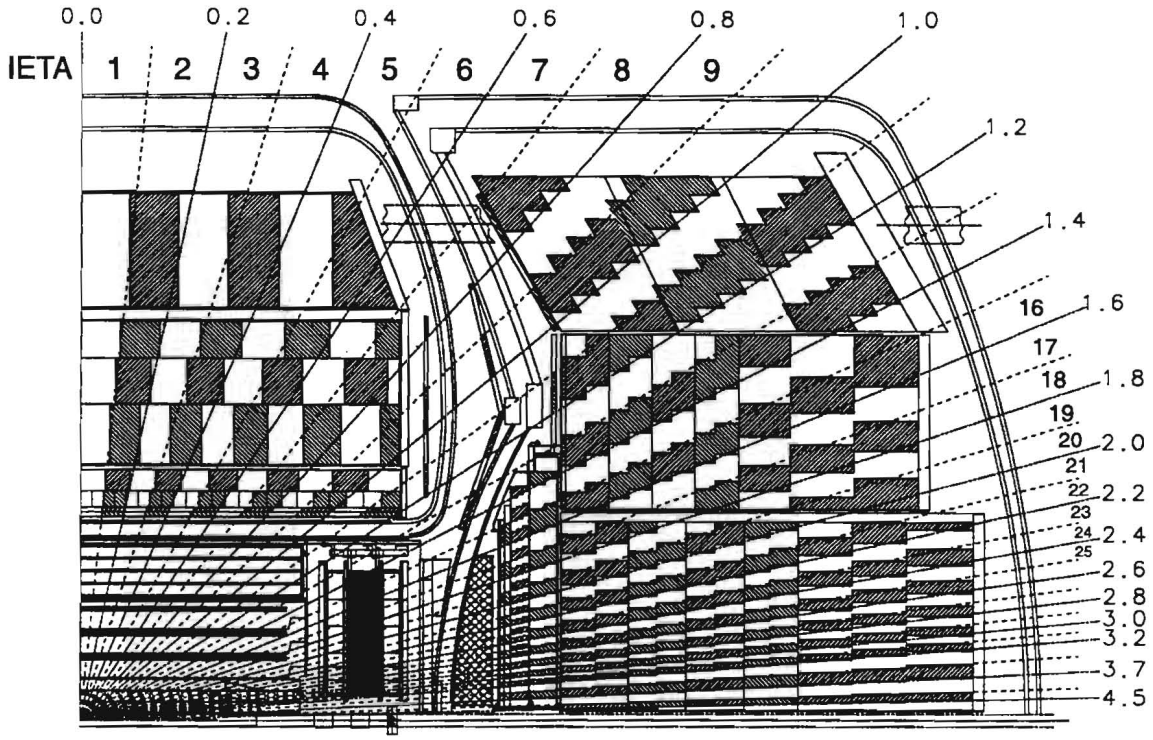

Figure 3.10: Side view of a calorimeter quadrant. Lines of pseudorapidity are shown to demonstrate the projective tower geometry.

of the Central Calorimeter, and thus serves essentially as an extension of the Central Coarse Hadronic layers. Also, the EC EM layers have slightly different thicknesses than in the CC, comprising 2.0, 2.0,7.9, and 9.3 electromagnetic radiation lengths.

Figure 3.10 also shows that the individual cells of the calorimeter are arranged projectively in towers of $\Delta\eta \times \Delta\phi = 0.1 \times 0.1$ so that their centers point back to the midpoint of the detector, which allows good shower shape resolution. In addition, to provide better measurement of electromagnetic shower position, the third layer of the EM

calorimeter (EM3), where EM showers typically leave the majority of their energy, is more finely segmented ($\Delta\eta \times \Delta\phi = 0.05 \times 0.05$).

To calibrate the calorimeter modules, sections of CC and EC calorimeter assemblies were studied in a test beam [17][18]. Electrons and charged pions with well-measured energies ranging from 2 to 150 GeV were scanned across the modules to simulate various angles of incidence. These studies found that the response of the calorimeter was linear above ~ 10 GeV, with a resolution for electrons of $15\%/(\sqrt{E})$, and $50\%/(\sqrt{E})$ for pions. To finely calibrate the EM calorimeter, calorimeter response was measured *in situ* by reconstructing the decays $Z \rightarrow e^+e^-$, $J/\psi \rightarrow e^+e^-$, and $\pi^0 \rightarrow \gamma\gamma$ [19]. Since the masses of these particles are well established (91.187 GeV, 3.096 GeV, and 134.97 MeV, respectively) and their decay products span a large energy range, exact calibration of the response versus energy is possible.

The Intercryostat Region

To accurately measure energy deposited in the gap between central and end cryostats, two additional detector systems are installed. The first, termed massless gaps, consist of single calorimeter readout cells placed in the region between the cryostat wall and the edge of the FH calorimeter section (in the CC) or the MH and OH sections (in the EC). These essentially make the regions between the calorimeter modules and the cryostat walls into an extra readout cell, albeit with very little mass to stop particles. In addition to the massless gaps, scintillating counter arrays called the Intercryostat Detectors (ICD) are mounted in the space between the central and endcap cryostats. Each ICD array consists of

384 tiles of $\Delta\eta \times \Delta\phi = 0.1 \times 0.1$, read out by phototubes, and covering an area on the inside face of the EC cryostats roughly corresponding to the MH and OH sections. While they are of no aid in identifying electromagnetic showers, the ICD and massless gaps provide enough information on hadronic showering between calorimeters to assist in the proper reconstruction of energy deposition between cryostats.

3.2.3 The Muon System

While the calorimeter stops and absorbs most particles within its volume, there are two particles it will not contain: neutrinos and muons. Neutrinos, due to their extremely small cross section for interaction with matter, cannot be detected at all, and the presence of a neutrino in an event must be inferred by summing the energies in the detector and determining the amount and direction of "missing" transverse energy (E_T) needed to make the total transverse energy sum vectorially to zero. Muons, however, will leave a trace of their passage via ionization - thus the outermost component of the D0 detector, the Muon System, is designed to identify muons and measure their momenta and position.

The Muon System consists of three sets of proportional drift tube chambers (PDTs) along with a toroidal iron magnet, implemented in 5 separate pieces, maintaining fields of ~2 T. The first set of PDTs, called the A layer, is mounted before the toroid and consists of four planes of PDTs; the B and C layers are mounted outside of the toroid, and consist of three planes of PDTs each, with the two layers separated by 1m. The A layer, with its extra plane of PDTs, detects muon hits and allows them to be associated with tracks in the Central Tracking Chambers; the B and C layers track the muon trajectory after it has been

bent by the magnetic field in the toroid, and thus allow the momentum of the muon to be determined from the magnitude of the bend.

3.3 Data Acquisition and Processing

3.3.1 The Trigger System

Since the accelerator produces beam crossings every 3.5 μs, the detector must evaluate a possibly interesting collision 285,000 times per second. At the other end of the timescale is the rate at which a complete readout of the detector - close to 150,000 channels - can be written to tape for storage: this is limited to 2-5 Hz. Condensing 285 kHz of potential collisions down to 2-5 Hz of interesting events which comprise the final data sample is done using the DØ Trigger System, which consists of three successive levels.

The Level 0 Trigger

The first level of triggering is the Level 0 Trigger, which signals that an inelastic collision occured in the beam crossing and this event is therefore worth examining by the higher levels of the trigger. The Level 0 system consists of two planes of rectangular scintillation counters, mounted 90° relative to each other to form a checkerboard-like pattern of coverage; one such pair is mounted on the front surface of each of the endcap calorimeters. When both counters register hits after a beam crossing, there is a >99% probability that an inelastic collision occurred; the rate of coincident hits is also an independent measure of the beam luminosity, and can provide feedback to accelerator operations. The timing difference between the two counters can be used to give a rough

measurement of the z of the interaction vertex, and can also indicate the presence of multiple interactions - all of this information can be utilized in the higher trigger levels.

The Level 1 Hardware Trigger

Once it is established that a collision has occurred, the Level 1 triggering system examines the calorimeter and the muon system for evidence of significant energy deposition. In order to do this within the 3.5 μs deadline, the Level 1 system uses fast, hardware-based algorithms to evaluate the event.

In the Muon system, 200 electronic readout boards known as Module Address Cards (MACs) receive from their assigned subset of muon chambers a list of cells from all planes which registered hits. These hits are processed by the MACs into a single "coarse centroid," representing the best quick estimate of the muon position. Centroids output by the MAC cards are then combined over the A, B, and C layers to give a rough momentum measurement; this information is then used by the Level 1 system to compare with trigger requirements for position and minimum momentum within 3.5 μs of the interaction. If needed, the system can initiate additional processing known as the Level 1.5 muon trigger system: this uses "fine centroids" generated by the MACs and can produce a more accurate measurement of the transverse momentum, but requires another 3.5 μs and thus incurs a deadtime penalty for the entire detector.

In the Calorimeter, a fast readout samples the rising edge of each cell's signal pulse, and sums these signals into $\Delta\eta = \Delta\phi = 0.2$ trigger towers, keeping separate account of EM and hadronic energies. Using lookup memories and the z position from Level 0, these tower energies are processed to provide the Level 1 system with EM, hadronic, and total

E_T values for each tower, as well as the missing E_T resulting from a sum over all towers. These quantities are then compared against the trigger requirements. The average rate of events passing at Level 1 is about 100 Hz.

The Level 2 Software Trigger

The final level of triggering is provided by the Level 2 system, which consists of 50 VAXstation 4000 computers (termed "nodes") connected to the rest of the system by high speed data cables. Events which pass the Level 1 system initiate a complete digitization and readout of the detector, and this information is sent to the first available Level 2 node, which then runs software-based algorithms to evaluate the event in much more detail than at Level 1. This digitization and processing requires about 200ms; however, this is well under the average time between events sent to a node from Level 1. To increase the speed of the readout, calorimeter cells are subjected to zero suppression, in which cells with less than 2σ fluctuations in energy from their normal, quiescent readout level are zeroed and suppressed, therefore saving the need to read out an energy value.

In practice, the three levels of triggering are carefully tuned and matched to each other to produce an optimum output stream of events. The Level 1 trigger system, having received a positive Level 0 result, can evaluate up to 32 separate sets of requirements (termed "triggers") on energy in one or more towers, and the position of those towers. These triggers are carefully selected to correspond to general types of physics events. Should any of these requirements be met, the event is passed on to a Level 2 node, where up to 128 sets of requirements (termed "filters") can be made. Each filter is matched to a specific Level 1 trigger, and serves to identify a more detailed and specific type of final

state. In addition, each trigger and each filter can be "prescaled" to pass only 1 of N events identified as matching its requirement - in this way, the passing rates can be kept within limits, and triggers/filters corresponding to common event types can be controlled to ensure that rarer triggers/filters are not lost to bandwidth limitations.

3.3.2 Event Reconstruction

Once the event has passed the online event selection system, it is then stored on 8mm tapes. However, in its raw form it consists of only the signals read out from each detector cell, information from the triggering process, and information about running conditions at the time it was taken. To put the data in a useful form for physics analysis, the DØ Reconstruction program (DØRECO) was developed to serve three main functions:

- Apply calibration information to the raw data to correct all detector hits
- Apply algorithms to the detector hits to identify and describe objects within the detector: photons, jets, muons, etc.
- Reduce the event to a manageable size for later storage and analysis

Reconstruction of the raw data was done using a farm of SGI and IBM Unix machines, though the program can be run on multiple platforms and can be rerun on processed data in order to apply new techniques or calculate new quantities. The DØRECO program itself is a large assembly of code packages which perform all the necessary functions of calibrating and interpreting the output of each detector; the relevant sections for this analysis are described below. The output of the program is a file using the ZEBRA data

structure, in which information is organized in "banks" which are referenced by pointer, and the ultimate size of the output file can be controlled by which banks are written to the file. DØ maintains several levels of datafiles, each carrying successively less information but allowing successively more ease in processing and disk storage.

The ZTRAKS package

This package is reponsible for the reconstruction of tracks within the tracking chambers; however, it also includes the determination of the event vertex using tracks reconstructed in the CDC.

Tracks are found in the CDC by reconstructing hits in the r–ϕ plane and aligning them first within each layer, forming what are called "segments." Starting with the outer layer, these segments are then compared, and if 3 of the 4 layer segments are sufficiently aligned a track is confirmed, after which the entire track is refit, a z position calculated, and a final cut made on the quality of the track.

Tracks in the FDC are determined in a similar way; however, because the forward region tends to have many more tracks from the breakup of the colliding particles, full reconstruction of the entire FDC is very time-consuming and is usually not done. Instead, only the region between the vertices and physics objects such as electrons or photons is reconstructed - the tracking "road," which is usually $\Delta\theta \times \Delta\phi = 0.2 \times 0.2$.

To determine the vertex, reconstructed tracks within the CDC are pointed back to their z-intercept point, and the points from all such intercepts are put into a histogram. A cluster finding algorithm is run to identify clusters of points, and those with at least three points are resolved into separate vertices, with the primary vertex assigned as the one with the

most points. The mean and error of the points in each cluster are then taken as the mean and error on the vertex position. If there is only one cluster, even with only one point, it is taken as the vertex; if there are no CDC tracks (perhaps 5% of the time), the FDC is used instead, in which case the entire FDC is reconstructed. The error on the vertex position can range from 6mm for an event with many tracks, to 2 cm for an event with only one CDC track, to 10cm if the FDC tracks must be used. For each found vertex a fit is then done using only those tracks pointing to that vertex and constraining them to originate from a single point, resulting in the final mean and error of the vertex z position. Note that determination of the x-y coordinate of the vertex is done using VTX readings during data-taking - the x-y dimensions of the beamspot are small and usually vary only a few microns from run to run, so that an average value can be used over a certain run period.

The CAHITS package

The CAHITS package is responsible for the bookkeeping of all the energies of each calorimeter cell, the application of calibration corrections, and the mapping of cells to physics coordinates. Its output, basically a corrected bank of all cells in the calorimeter, is then used by object finding packages such as those relevant to this analysis, CAPHEL and CAJETS.

The CAPHEL package

As implied by its name, this package searches the calorimeter to find photons and electrons. It employs a clustering algorithm which finds towers (0.1×0.1) in the EM calorimeter above a certain E_T threshold, then associates neighboring towers with this

tower until no neighboring towers above a 50 MeV threshold are found. The package then calculates quantities for this cluster (such as its total energy, position, etc.), making several ZEBRA banks full of information, and also associates with it any tracks coming from the primary vertex within the tracking road between the vertex and the cluster, making links to the corresponding tracking ZEBRA banks.

The CAJETS package

The CAJETS package is similar to the CAPHEL package, in that it must search the calorimeter to find jets. Since the definition of a jet, and which particles in the event should be associated with it, is somewhat ambiguous, several different algorithms are used. The one relevant to this analysis is the fixed cone definition, using a radius of 0.7 in $\Delta\eta \times \Delta\phi$ space.

In the first stage of the algorithm, a "precluster" is found similarly to the electron/photon case: the cell with the highest E_T in the calorimeter is used as a starting point, and cells with E_T greater than 1 GeV and within 0.3 in η or ϕ are grouped together around it; these cells are then removed from consideration and the remaining highest cell has a precluster built around it; and so on until all cells with more than 1 GeV E_T are in a precluster.

Then for each precluster, cone clustering is applied: starting with the highest E_T precluster, the E_T weighted centroid of the cluster is found, and all towers within a radius of 0.7 in $\Delta\eta \times \Delta\phi$ are assigned to the jet. The jet axis is recalculated using these towers, and the process is then iterated until the jet axis becomes stable. If the resulting jet has

$E_T > 8$ GeV it is kept, and it is compared against other jets found for any shared towers. Should any two jets share towers, an algorithm is run which either splits them, assigning contested cells to the nearest jet, or merges them, depending on how much E_T is shared between the two. Split or merged jets then have their axis recalculated a final time.

Chapter 4

Event Selection and Efficiencies

In order to measure the cross section for direct photon production, we must first define what we expect a direct photon to look like in our detector, and place requirements on all photon candidates in order to select these characteristic events and reject non-signal events. As outlined in Chapter 3, this can be done at the trigger level, selecting events which look like direct photon events, and then refined further using offline cuts to impose even stricter requirements. The goal of background rejection may lead to cuts harsh enough to reject even some real direct photon events; therefore, we must also estimate the number of direct photon events lost so that the total number measured can be corrected to equal the total number produced.

4.1 Data Set and Monte Carlo

4.1.1 Direct Photon Triggers

Because the direct photon production rate falls steeply with E_T, multiple triggers/filters must be used to acquire data in each E_T region and prescaled accordingly to achieve comparable statistics over the measurable E_T range. The direct photon candidate sample was obtained using the four single photon triggers and filters summarized in Table 4.1. The two lowest E_T filters, GAM_6_ISO_GAM and GAM_14_ISO_GAM, were taken in special runs, when the luminosity and event rate were lower and the full bandwidth of the trigger system was devoted solely to photon triggers; therefore, usually only the 6 Gev filter was prescaled. The two highest filters, EM1_GIS and EM1_GIS_HIGH, were taken as part of global running, where only a part of the bandwidth was devoted to photons. The EM1_GIS filter was therefore prescaled, with the EM1_GIS_HIGH filter also prescaled at very high luminosity running where high event rates taxed the trigger system's capability. Total integrated luminosities for each filter are also shown in Table 4.1, and carry a 5.4% uncertainty.

Inefficiencies due to triggering do occur; however, to avoid this complication, filters were used in the cross section measurement only where fully efficient. Detailed descriptions of the triggering algorithms, triggering efficiencies and the determination of integrated luminosity for each filter are included in Appendix A.

Table 4.1: Description of triggers and associated integrated luminosities.

Level 1 Trigger	L1 Threshold (GeV)	Level 2 Filter	L2 Threshold (GeV)	Luminosity (nb^{-1})
EM_1_2_GAM	2.5	GAM_6_ISO_GAM	6	13.644
EM_1_7_GAM	7	GAM_14_ISO_GAM	14	225.29
EM_1_HIGH	14	EM1_GIS	25	14577
		EM1_GIS_HIGH	40	94657

4.1.2 Candidate Sample

The standard cuts applied offline to define a good photon candidate are :

- $0 \leq |\eta| \leq 0.9$ $(1.6 \leq |\eta| \leq 2.5)$ in the central (forward) regions. These cuts define the region of phase space which will be measured in the cross sections.

- $0 < |\text{IETA}| \leq 9$ $(16 \leq |\text{IETA}| \leq 25)$ in the central (forward) regions. The quantity IETA is the integer index of each 0.1×0.1 calorimeter tower in pseudorapidity (see Figure 3.10). This cut restricts the candidates to be well within calorimeter boundaries.

- vertex z position $|Z_{vtx}| < 50$ cm to retain the benefits of projective geometry.

- Exclude candidates within 10% of a module edge in ϕ (CC only). Energy reconstruction near these edges is not well understood.

- no track pointing to the candidate from any found vertex.

- $\frac{E_{EM}}{E_{tot}} > 0.96$, where E_{EM} (E_{tot}) is defined as the EM (EM + hadronic) energy in a core cone of 0.2 around the candidate. This rejects hadron showers, which leave significant energy past the electromagnetic layers of the calorimeter.

- $[E_T(R = 0.4) - E_T(R = 0.2)] < 2$ GeV where $R = \sqrt{\Delta\eta^2 + \Delta\phi^2}$ and the E_T within a cone of radius R refers to the sum of EM and hadronic layers. This isolation requirement rejects most neutral mesons, which are typically part of a jet and therefore are accompanied by additional energetic particles.

- H-matrix $\chi^2 < 150$. The H-matrix algorithm is a measure of shower shape in the calorimeter, and uses the total energy, energy deposition in each layer, each energy in a 6x6 array of cells in EM3, and the vertex z position as 41 separate, characteristic observables of a shower. These are combined in a covariance matrix

$$M_{ij} = \frac{1}{N} \sum_{n=1}^{N} (x_i^n - \bar{x}_i)(x_j^n - \bar{x}_j) \tag{4.1}$$

where x_i^n is the value of observable i for candidate n and $\bar{x}_i$ is the mean value of the observable i for a sample of "ideal" electromagnetic showers (test beam and

Monte Carlo electrons were used to tune the matrix). A χ^2 distribution

$$\chi^2 = \sum_{i,j}(x_i^k - \bar{x}_i)H_{ij}(x_j^k - \bar{x}_j) \tag{4.2}$$

($H = M^{-1}$) can then be formed to measure how well each candidate compares to the expected shower shape. An illustration of the H-matrix discriminating power between 25 GeV test beam electrons and pions is shown in Figure 4.1 [20]; the distribution for electrons from a sample of $W \rightarrow e\nu$ decays (~ 25-40 GeV) is included for comparison. Figure 4.1 demonstrates the effectiveness of a cut at $\chi^2 = 150$ in selecting electromagnetic showers.

The first four requirements are classified as acceptance cuts; the last 3 are known as the photon selection cuts, as they provide the bulk of the photon identification and discrimination from backgrounds.

To illustrate the effect of each of these cuts on the data sample, and to show the number of events each filter contributed to the analysis, the number of raw events satisfying the physics η requirement in each region is shown in Table 4.2.

4.1.3 DØGEANT Monte Carlo

In order to calculate cut efficiencies and estimate background from neutral mesons, several different types of simulated (Monte Carlo) events were generated [21] using the PYTHIA event generator [22]. These were generated including PYTHIA modeling of the spectator event, and simulated using a DØ-specific implementation [23] of the GEANT

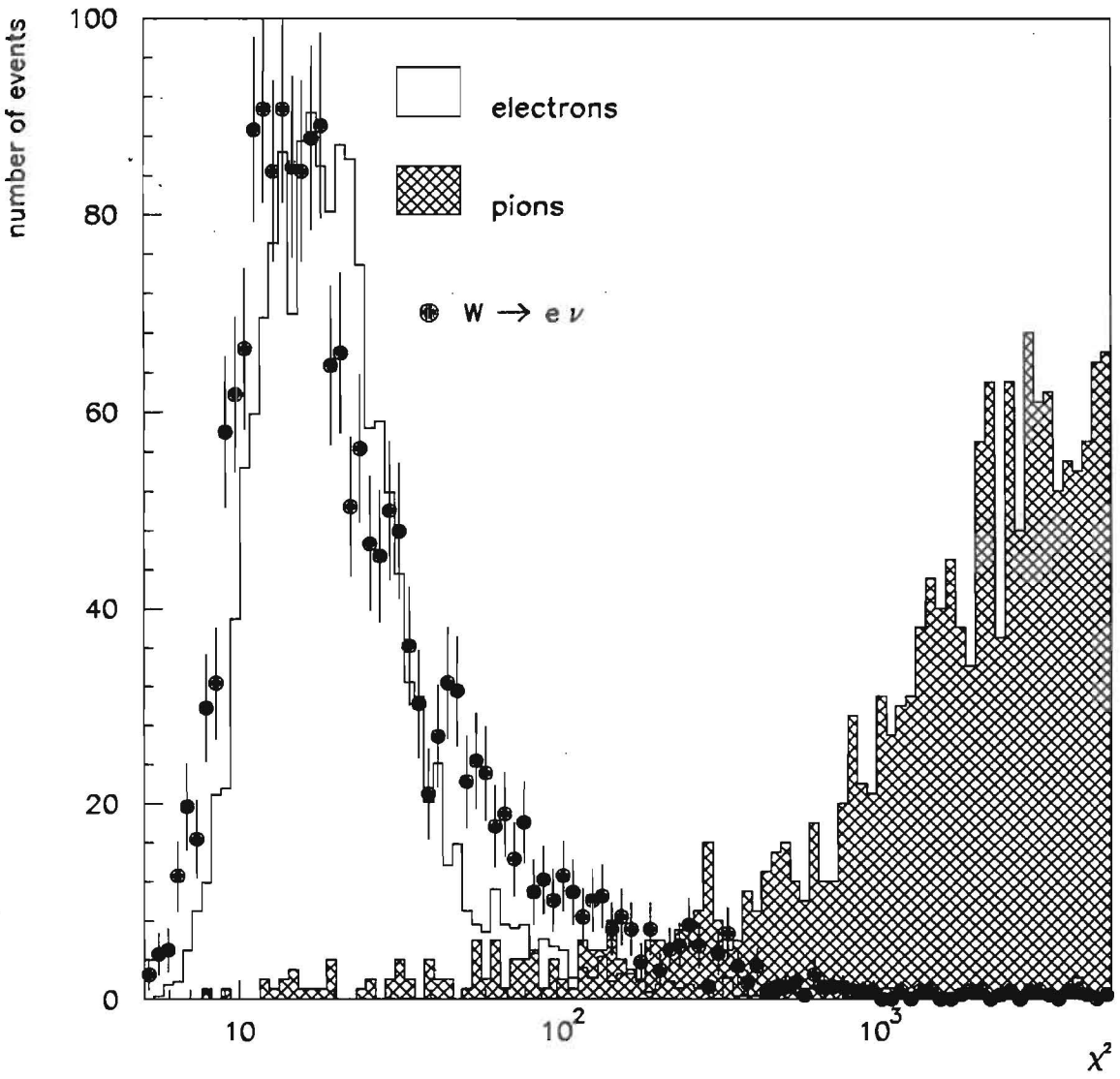

Figure 4.1: H-matrix χ^2 distributions from test beam electrons, test beam pions, and electrons from *W* decays.

Table 4.2: Number of events surviving the application of photon cuts.

Filter		# before cuts (after η cut)	# after acceptance	# after track cut	# after selection cuts
GAM_6	CC	28878	20087	11850	4628
	EC	25370	21264	6214	2777
GAM_14	CC	5820	4170	2327	1346
	EC	6839	5579	1485	890
GIS	CC	79469	56558	27622	13823
	EC	82091	68580	15036	7496
GIS_HIGH	CC	79499	57490	26988	12283
	EC	58602	50571	9323	3861

detector simulation package [24] with fully detailed geometry. In order to model uranium noise effects, multiple interactions, and "pile-up" (which occurs when a cell is read out before the calorimeter electronics are fully recovered from energy deposition in a previous beam crossing) the Monte Carlo was merged with non-zero suppressed zero bias data, taken without any trigger requirement at Level 0 or above. The combined files were then zero suppressed and reconstructed as in the data. The Monte Carlo was put through several iterations of this overlay process to produce 5-10 times the number of final events; this smooths the effects of noise and multiple interactions for a given number of Monte Carlo showers. Since the statistical power of the Monte Carlo sample is limited by the number of actual PYTHIA events generated, however, statistical errors were kept equal to that due to the actual number generated before the overlay process.

Single photon events were generated over the range 10-200 GeV (segmented into four parts for roughly equal statistics in each), resulting in a falling E_T spectrum closely resembling the data. A large sample was generated for background studies (Chapter 5) in which only the region around the photon was simulated in DØGEANT to save processing time; a smaller sample in which the entire event was simulated was used for efficiency and physics studies. A sample of full W and Z events was also generated for comparison to data.

As a check on the ability of the Monte Carlo to model the data, a sample of electrons from Monte Carlo $W \rightarrow e\nu$ events was compared to electron candidates from data $W \rightarrow e\nu$ events taken from the direct photon trigger sample. The results are shown in Figure 4.2 (CC) and Figure 4.3 (EC). Shown are the EM fraction, the H-matrix χ^2, and the isolation E_T; the Monte Carlo (histograms) show good agreement with the data (points), though the isolation E_T distribution has a slightly larger tail in the data than in the Monte Carlo.

4.2 Acceptance

The acceptance A corrects for the effects of the IETA, vertex position, and ϕ module cuts on events with physics η in the central or forward range.

The Run 1B vertex z distribution is shown in Figure 4.4. This distribution was found to be stable during Run 1B and between different photon triggers, and is described by a Gaussian peak of mean -0.3 cm and width 28.5 cm. The vertex position acceptance was determined simply by measuring the number of events lost from the vertex distribution

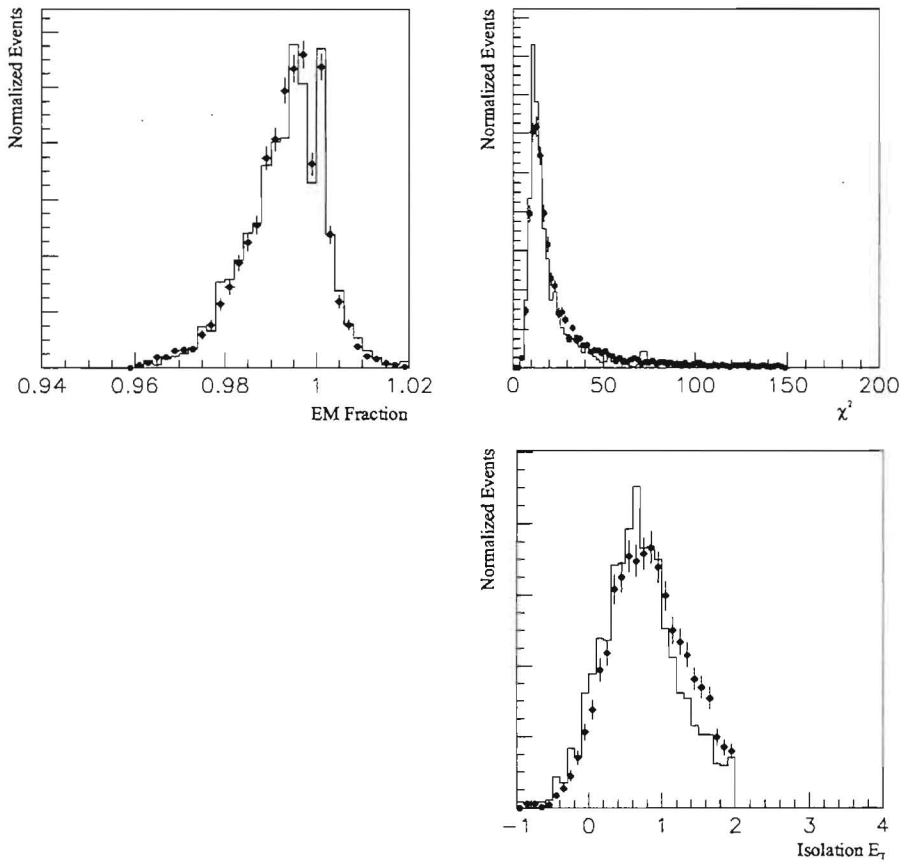

Figure 4.2: Comparison of data (points) and Monte Carlo (histograms) *W* electrons in the central region.

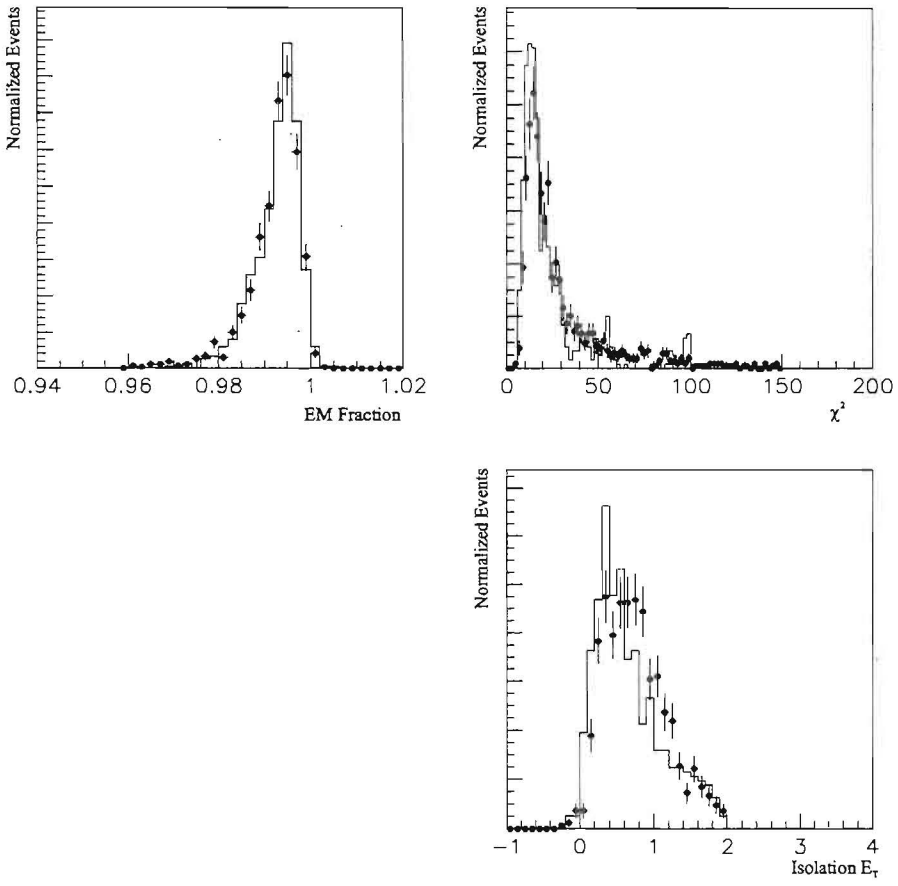

Figure 4.3: Comparison of data (points) and Monte Carlo (histograms) *W* electrons in the forward region.

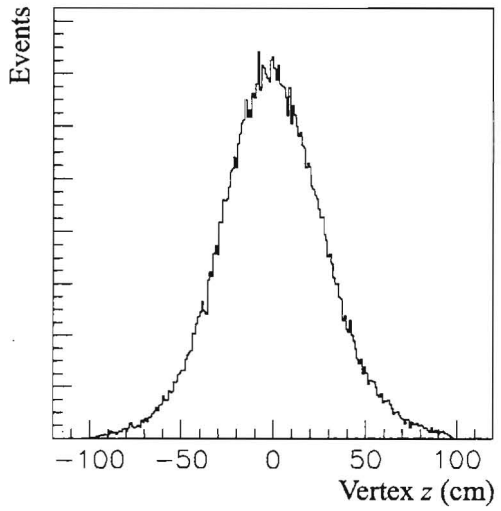

Figure 4.4: The Run 1B vertex z distribution.

after the cut. This was measured separately for all four filters, and was found to be very consistent; the acceptance for this cut using all four filters is 0.913 with a negligible error.

The IETA acceptance was measured using the Owens, et.al. Monte Carlo program [25] to generate photons with the theoretically modelled η distribution in each region. Each event was smeared with a Gaussian vertex distribution to mimic the data distribution, a 50 cm cut was placed on the vertex position, and the calorimeter IETA of the resulting candidates was calculated geometrically. While this should give the appropriate acceptance for real photons, the calculation was also done assuming a flat distribution in physics η, and the difference taken as a systematic error. The resulting IETA acceptance is 0.917 ± 0.007 (0.930 ± 0.007) in the CC (EC).

Combining the vertex and IETA acceptances with the exact ϕ module acceptance of

0.80 in the CC, the total acceptance is then $A = 0.670 \pm 0.007$ (0.849 ± 0.007).

4.3 Cut Efficiencies

4.3.1 Tracking Considerations

By vetoing candidates with a track, real photon candidates are lost in two ways:

- A photon might convert to an e^+e^- pair in the material in front of the CDC/FDC; the fraction of such conversions whose track is accurately reconstructed will be removed from the sample.

- A charged track produced as part of the underlying event might overlap the photon closely enough to lie within the tracking road, in which case the photon will be removed from the sample.

The effect of the charged track cut is considered in detail in Appendix B; the total efficiency due to both sources is found to be $\varepsilon_{track} = 0.828 \pm 0.013$ (0.554 ± 0.030).

4.3.2 Selection Cuts

Selection cut efficiencies were determined using full Monte Carlo photon events which were put through the trigger simulator, and are shown in Figure 4.5. The efficiency dips at very low E_T due to the Hmatrix and EM fraction cuts, as the shower shape changes and the roughly constant contribution of noise from the FH1 layer becomes an increasingly larger

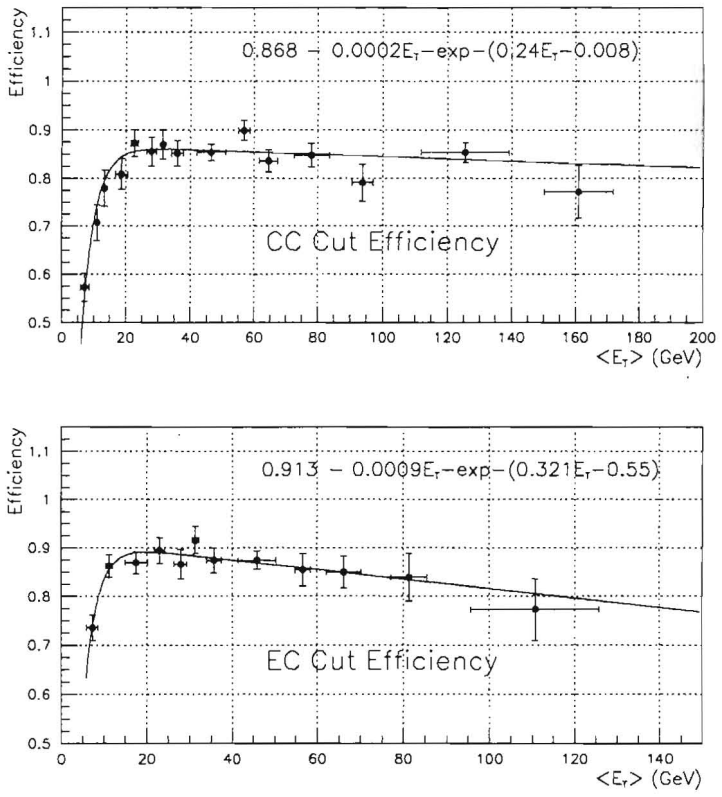

Figure 4.5: Selection cut efficiencies measured using PYTHIA Monte Carlo photons, and corresponding fits.

fraction of the total energy. The isolation cut causes a fairly linear decrease with increasing E_T, as outlying edges of the shower become more energetic relative to the fixed 2 GeV cut. The selection cut efficiencies were thus fit to the form

$$a - e^{-(bE_T + c)} + dE_T \tag{4.3}$$

with the values of the parameters a, b,c, and d as shown in Figure 4.5.

Because the global running data were taken over a range of instantaneous luminosities,

the effect of instantaneous luminosity on the selection cut efficiencies was studied using full event Monte Carlo overlaid with 5E30 and 19E30 zero bias data. Initial studies using Monte Carlo *W* electrons overlaid with 5E30, 14E30, and 19E30 zero bias data indicated that the selection cut efficiency dropped linearly with increasing instantaneous luminosity, resulting in a 10-20% lower efficiency at the highest luminosities. Since the instantaneous luminosity of the data set was peaked at ~ 6E30, however (Figure 4.6), with only a small

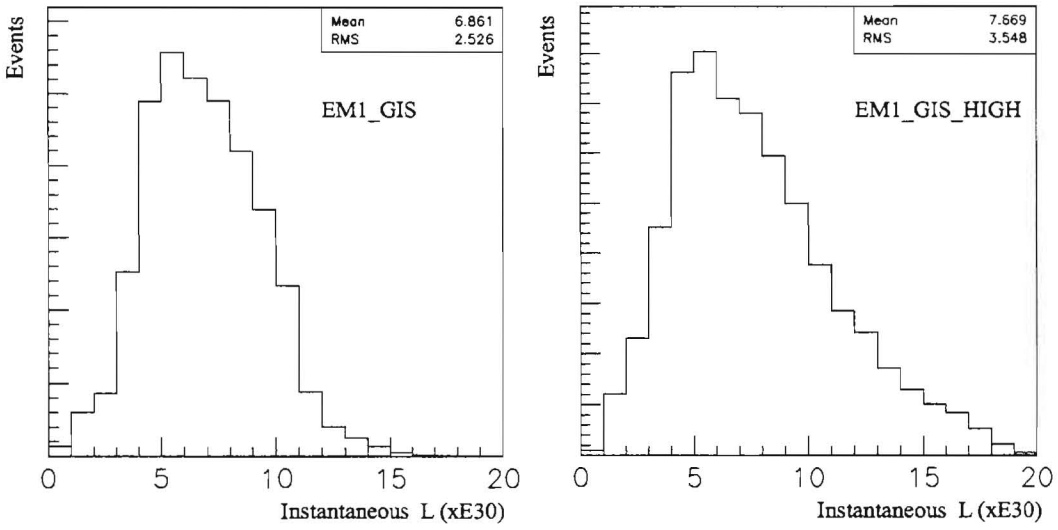

Figure 4.6: Instantaneous Luminosity profiles for the EM1_GIS (left) and EM1_GIS_HIGH (right) filters.

tail extending to the highest luminosities, the average efficiency was expected to be close to that at 5E30, allowing selection cut efficiencies to be determined using Monte Carlo

with only the 5E30 overlay.

This expectation was checked using the photon Monte Carlo: for several E_T bins above 30 GeV, the 5E30 and 19E30 efficiencies were measured and used to define a linear parametrization of the efficiency vs. luminosity. Using the instantaneous luminosity profiles of the EM1_GIS filter (or EM1_GIS_HIGH, depending on the E_T of the bin), a weighted efficiency was then constructed for each E_T bin by summing over the luminosity bins, weighting each with the parametrized value of ε_{sel}. The resulting weighted efficiencies were found to agree with those derived from the 5E30 Monte Carlo to within 2.5% or less; an uncertainty of 2.5% is therefore placed on the fitted selection cut efficiencies derived from the 5E30 Monte Carlo.

To cross-check these efficiencies, a sample of Z events was selected and a background-subtracted selection cut efficiency calculated for Z electrons between 30-50 GeV. The resulting efficiencies were 0.865 ± 0.011 (0.902 ± 0.018) for electrons with mean E_T of 42.7 (36.4) GeV. The fitted efficiencies evaluated at these points, 0.859 ± 0.021 (0.880 ± 0.022), are in good agreement with the Z efficiencies.

Chapter 5

Background Estimation

5.1 Introduction

The main background to the direct photon signal comes from jet fluctuations. While most jets consist of many particles, and are thus easily distinguishable from a single photon, a small fraction (10^{-3} - 10^{-4}) fragment such that a single particle carries most of the momentum of the parent parton. Several neutral mesons decay to produce two or more photons, including the lightest (and therefore most commonly produced) neutral meson, the π^0, which decays to two photons with a branching ratio of 99% [4]. Thus non-direct photons are common in hadronic collisions, and because jet production rates are a factor of 10^3 larger than that of direct photons, the number of jets which fragment to a single meson and then decay to photons - referred to as electromagnetic (EM) jets - are comparable to the level of direct photon signal. Because of this, the level of background in the direct photon data sample must be carefully measured and subtracted.

Table 5.1: Neutral meson decays to photon states.

Particle	mass (GeV/c^2)	decay products	branching ratio
π^0	0.135	$\gamma\gamma$	0.99
η	0.547	$\gamma\gamma$	0.39
η	0.547	$3\pi^0$	0.32
η	0.547	$\pi^0\pi^+\pi^-$	0.23
K_s^0	0.494	$2\pi^0$	0.31
ω	0.781	$\pi^0\gamma$	0.09

Further complicating matters is the fact that, at the energies considered in this analysis (above ~10 GeV), the individual photons from meson decays cannot be separately identified given the spatial resolution of the DØ calorimeter - the decay products coalesce into a single shower which is difficult to distinguish from a single photon. This can be seen by considering that the two photons arising from a π^0 decay have an opening angle distribution peaked at the minimum [26]

$$\theta_{min} \cong \frac{2m_\pi}{E_\pi} \tag{5.1}$$

which for a 10 GeV π^0 results in a minimum separation of 2.5 cm at the first layer of the DØ calorimeter. Since a typical cell size in the calorimeter is ~7 cm, it is clear that most π^0 decays will not be identifiable as two distinct photons.

While Table 5.1 identifies several neutral mesons which decay to photons, the π^0 and η are the main particles considered in this analysis, as they are the two neutral mesons which are most commonly produced. Other backgrounds are expected to be further

suppressed in the data sample due to small branching ratios (e.g., the ω) as well as the photon selection cuts. For example, while a significant fraction (~30%) of K_s^0 mesons decay to $2\pi^0$, at lower values of E_T the four resulting photons are sufficiently spread out that they usually fail the photon selection cuts. At higher E_T the showers coalesce and the passing rate is higher; however, due to the long lifetime of the K_s^0, at higher E_T a significant fraction do not decay before they reach the EM calorimeter, and thus create a hadronic shower which also fails the photon cuts. As a result, the expected ratio of K_s^0 to π^0 in the data sample is less than 5%.

5.2 Background Estimation Techniques

5.2.1 Method

While background subtraction on an event-by-event basis is impossible, there is a statistical method which exploits the difference between single photons and multiple photon clusters as they traverse the detector. At the energies considered in this analysis, photons begin showering in the calorimeter by converting to an electron-positron pair ($\gamma \rightarrow e^+e^-$) near a nucleus. The probability for this to occur is dependent on the amount of material the photon passes through; the deeper into the calorimeter the photon gets, the more likely a conversion becomes.

Consider the probability P_{EM1}^{γ} that a single photon will convert in or before the first

calorimeter layer. For a π^0 meson decaying to two photons, the probability that at least one of the photons will convert is then greater than in the single photon case:

$$P^{\pi}_{EM1} = 2P^{\gamma}_{EM1} - (P^{\gamma}_{EM1})^2 \tag{5.2}$$

In other words, multiple photon showers are more likely to begin earlier in the calorimeter, since there are more independent chances for a photon to convert early. As an example of this, consider Figure 5.1 [2], which shows the clear difference in the fraction

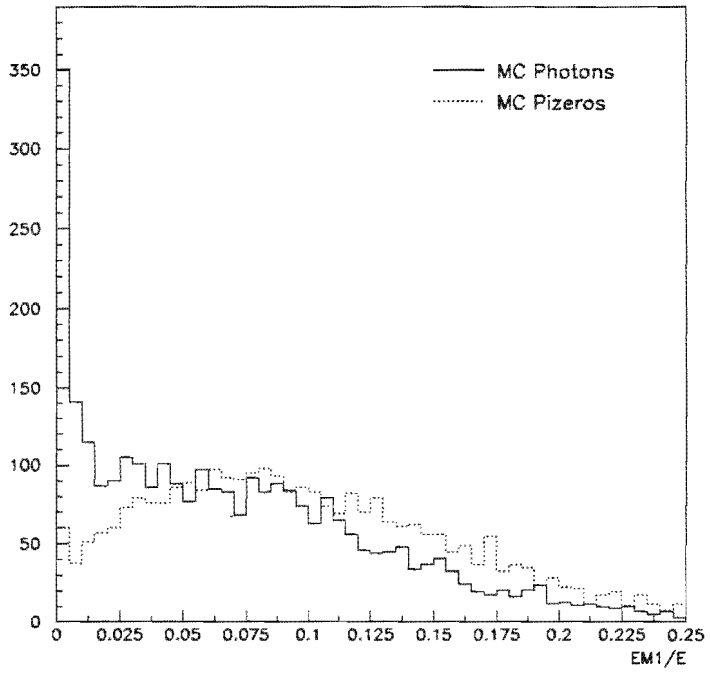

Figure 5.1: Comparison of EM1 energy fraction left by 10 GeV MC photons and π^0's.

of total energy left in the first electromagnetic calorimeter layer (EM1) by single Monte Carlo photons and π^0's. While a significant fraction of photons leave little or no energy in EM1, relatively few π^0's do so.

This difference provides discriminating power with which to estimate the fraction of background present in the direct photon candidate sample. The data distributions can be compared to those of Monte Carlo photons and neutral mesons to determine the relative fraction of each present in the data.

As a discriminant variable, we use the logarithm of the fractional EM1 energy

$$\log(\mathrm{EM1/E}) = \log_{10}\left(\frac{E_{EM1}}{E_{total}}\right) \tag{5.3}$$

with the denominator E_{total} calculated as the sum of the layers:

$$E_{total} = \sum_{n=1}^{5} E_n \tag{5.4}$$

(where $n = 5$ represents the FH1 layer). This quantity emphasizes the region of small fractional EM1 energy where the greatest difference between photons and mesons is seen.

5.2.2 Background Monte Carlo

Previous analyses [16][2] used single π^0 and η mesons, generated at discrete energies, DØGEANTed, and with the appropriate π^0/η production ratio, as a model of the EM jet background. While this model provided the primary constituent of an EM jet, and reproduced the data EM1 distributions fairly well, it was found that the single particles did not recreate some other distributions such as the isolation E_T [16]. In general, the Monte Carlo mesons were found to be more isolated than data showers, which is to be expected

since real jets produce a spectrum of particles, and in EM jets, the meson that carries most of the momentum is usually accompanied by softer particles. Further evidence that a more detailed background model was desirable came from the fact that when considering the π^0 and η backgrounds separately, comparison to data favored the η even though the π^0 is expected to be produced and selected more often. Since the η Monte Carlo included the $3\pi^0$ and $\pi^0\pi^+\pi^-$ decay states as well as the $\gamma\gamma$ state, this indicated a preference for more complex, multi-particle showers.

In order to provide a better background model for this analysis, a large number of PYTHIA QCD dijet events were generated in a falling E_T spectrum over a range similar to the Monte Carlo photons (Section 4.1.3). Just as in the data, these events were then "filtered" to find EM-fluctuated jets: at the particle level, π^0 and η mesons were selected by requiring

- $[E_T(R=0.4) - E_T(R=0.2)] < 2$ GeV where $R = \sqrt{\Delta\eta^2 + \Delta\phi^2}$ around the meson
- No charged particle within a cone of $R = 0.2$
- Energy within a cone of $R = 0.2 > 60\%$ of parent parton energy

Only events passing this filter (~0.1-0.01%) were then run through DØGEANT; in addition, only a cone of $R = 1.0$ around the parent meson was simulated to save processing time.

It is important to note that even with the particle level filter, a major constraint on Monte Carlo production was the availability of processing power. This has also been a factor in the past, and is in fact one reason why previous analyses were limited to single particle Monte Carlo. The Monte Carlo events used in this analysis were generated on a farm of DEC 3000/400 Alpha workstations at the Supercomputer Computations Research Institute in Tallahassee, FL; a fully detailed DØGEANT event required approximately one hour of CPU time to generate. Also, while the particle level filter was intended to avoid unnecessary simulation of events which would fail the offline cuts, it was necessarily loose enough to ensure a reasonably realistic EM jet sample. As a result, the fraction of DØGEANTed EM jets which passed the photon cuts (and could therefore be used in modeling the data sample) was still only about 30%.

As in the case of the photon Monte Carlo, events were overlaid with non-zero suppressed zero bias data to add detector and multiple event effects.

5.2.3 EM1 Calibration

Because this method of background estimation relies on accurate modeling of the data by Monte Carlo, it is important to verify that the Monte Carlo reproduces the data distributions. Such agreement was demonstrated in Section 4.1.3; however, the log(EM1/E) distributions must also be examined.

These distributions are shown in Figure 5.2 for *W* electrons from data and from Monte Carlo. While the central region Monte Carlo (left) shows good agreement in shape and peak with the data, the forward region (right) shows a slight offset - the Monte Carlo showers have a slightly smaller fraction of energy deposited in EM1 than the data. This

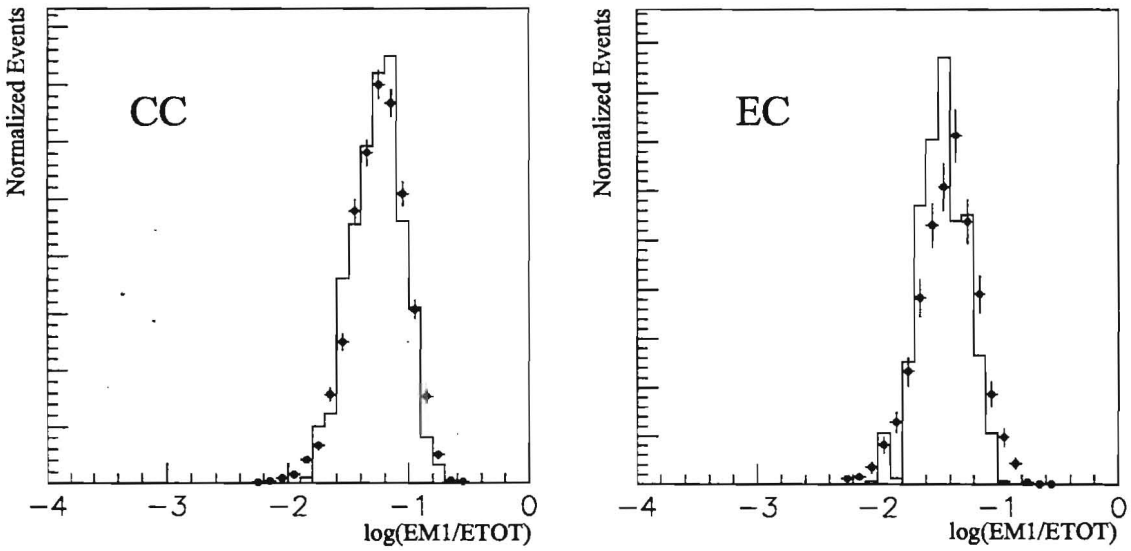

Figure 5.2: Log(EM1/E) distributions for *W* electrons from data (points) and Monte Carlo (histograms).

difference directly affects the background estimation, since a shift in the Monte Carlo distributions represents a shift in the position of the data between the extremes of the Monte Carlo jet and photon behavior. To ensure that the Monte Carlo best models the data, this offset must be corrected.

The reasons for the difference are considered in detail in Appendix C, where it is determined that the offset is consistent with a difference in EM1 sampling weight between the Monte Carlo and the data. Since the sampling weight is simply a multiplicative factor applied to the raw energies read out from EM1, the Monte Carlo can be properly calibrated by applying another multiplicative factor to the EM1 energy, or equivalently an additive offset to the log(EM1/E) distributions. Using the *W* electron data, the offsets were

derived separately for the North and South endcap calorimeters, and were found to be 0.147 ± 0.013 (North), and 0.094 ± 0.013 (South) in the log(EM1/E) variable. For completeness, a very small central region offset (0.014 ± 0.005) was also applied.

5.3 Purity Calculation

An example of the log(EM1/E) distributions for central region data, Monte Carlo photons, and Monte Carlo EM jets between 33 and 39 GeV is shown in Figure 5.3. The Monte Carlo distributions are binned in 50 bins across the range $-4.0 < \log(\text{EM1/E}) < 0.0$, and are normalized to the data so that they may be directly compared. Note that in the log(EM1/E) variable, a value of -1.0 indicates 10% of the shower energy deposited in EM1, a value of -2.0 indicates 1%, etc. The difference in single and multi-photon behavior is seen in the larger tail of the photon Monte Carlo at left (smaller values of EM1/E), and the sharper peak in the jet distribution which occurs at larger values of EM1/E.

Using the CERNLIB MINUIT program, a χ^2 minimization was performed to fit the data log(EM1/E) distribution as a sum of the photon and background distributions:

$$F_{data}(P, x) = PD_{\gamma}(x) + (1 - P)D_{jet}(x) \tag{5.5}$$

where P is the purity of the photon sample (the single parameter of the fit), and x is the range of log(EM1/E). Fits were performed for 13 separate E_T bins in the central region, and for 10 bins in the forward region. The resulting fit for the central region between 33 and 39 GeV is shown in Figure 5.3; a complete set of fits for both regions is included as Appendix E.

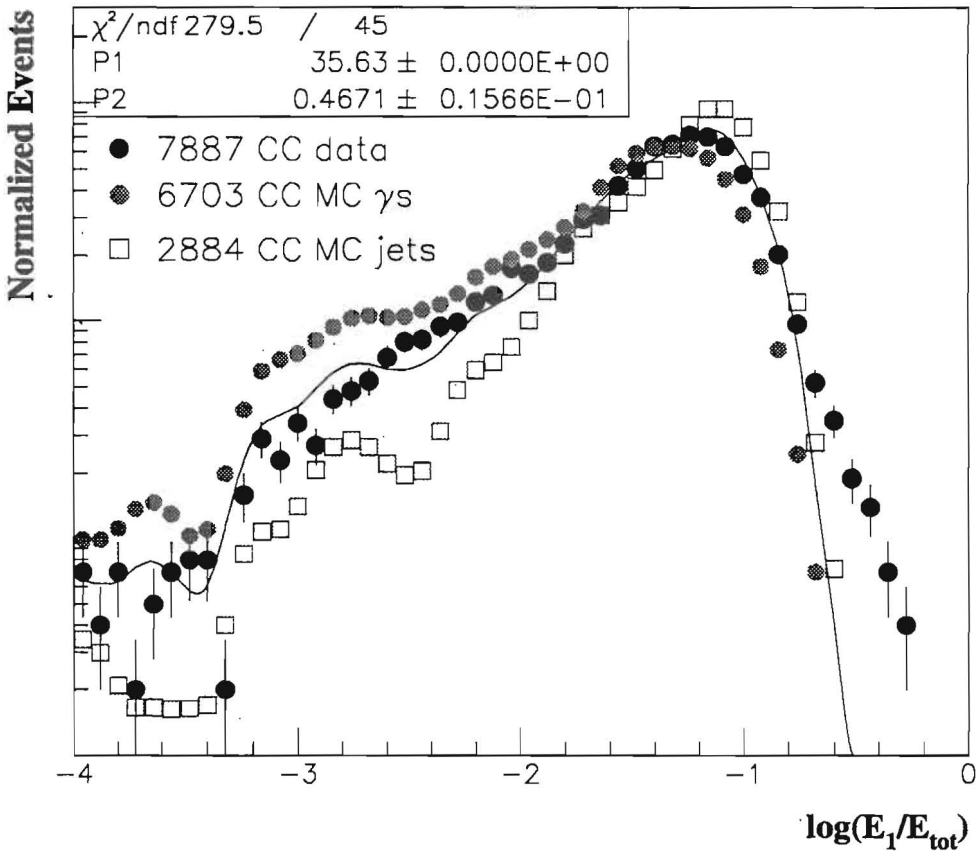

Figure 5.3: Log(EM1/E) for Monte Carlo and data between 33-39 GeV in the central region. The solid line is the MINUIT fit, which results in a measured purity of 0.467 (P2).

Prior to fitting, the Monte Carlo distributions were smoothed to reduce statistical effects. In order to ensure that the data and MC were comparable in E_T across each bin, the Monte Carlo E_T spectra were weighted to match the data E_T spectrum. This had a negligible effect except in bins where the Monte Carlo was not matched well to the E_T bin edges (e.g., near the Monte Carlo generation E_T bin thresholds), and in E_T bins where

statistics were limited, in which cases it resulted in small (less than ~ 6%) corrections to the fit result.

The events in the data with large *EM1/E* (seen at the right edge of the distribution in Figure 5.3), which are not accurately modeled by the Monte Carlo, are due in part to a small fraction of candidates which had a track pointing beyond the allowed vertex reconstruction region, and which impacted on the calorimeter at a far steeper angle than modeled in the MC. The effect of these events was investigated by fitting the distributions over only the range from -4.0 to -0.8; no significant difference was observed.

For each purity point, the statistical error on the fit given by MINUIT was inflated by $\sqrt{\chi^2}$ of the fit in order to estimate the combined statistical and systematic error on the fit to the smoothed MC distributions for each point. The change in purity when calculated with unsmoothed distributions was also added in quadrature to the error on each point, in order to estimate the effect of limited MC statistics (which are not explicitly included in the MINUIT error). The purity points, errors, and variation with smoothing and E_T weighting are summarized in Table 5.2 and Table 5.3.

The purity versus E_T for the central and forward regions is shown in Figure 5.4. It is important to note that the purity should be a continuous distribution in E_T; it is therefore reasonable to fit the measured purity points to a functional form. The function

$$P = \frac{1}{1 + a(E_T)^{-b}} \tag{5.6}$$

was selected, as it satisfies the evident boundary conditions of low purity at low E_T and high purity at high E_T. Further, one would expect the data set to be a sum of two falling

Table 5.2: CC Purity points, variations, and errors.

E_T (GeV)	Purity	Inflated Fit Error	$\Delta_{\text{unsmoothed}}$	$\Delta_{\text{no Et correct}}$	Total Error
10.9	0.112	0.307	-0.021	0.065	0.308
13.2	0.144	0.062	-0.025	0.008	0.067
17.1	0.245	0.148	-0.151	0.001	0.211
22.7	0.395	0.051	-0.048	0.006	0.070
27.2	0.350	0.070	-0.072	0.006	0.101
31.4	0.372	0.043	-0.127	-0.007	0.134
35.6	0.467	0.039	-0.066	0.056	0.077
44.5	0.460	0.044	-0.040	-0.001	0.059
56.8	0.558	0.045	0.001	-0.007	0.045
64.3	0.644	0.052	-0.037	0.016	0.063
77.4	0.726	0.042	-0.003	0.025	0.042
93.4	0.826	0.060	0.046	0.005	0.076
115.7	0.789	0.040	-0.030	-0.002	0.050

Table 5.3: EC Purity points, variations and errors.

E_T (GeV)	Purity	Inflated Fit Error	$\Delta_{\text{unsmoothed}}$	$\Delta_{\text{no Et correct}}$	Total Error
15.3	0.482	0.056	-0.023	0.025	0.061
22.7	0.520	0.060	-0.092	0.016	0.110
27.1	0.603	0.078	0.017	0.006	0.080
31.4	0.614	0.032	-0.012	0.010	0.034
35.6	0.571	0.032	-0.022	0.013	0.039
44.0	0.606	0.032	-0.013	0.023	0.034
56.7	0.695	0.037	-0.031	0.029	0.049
65.6	0.812	0.041	0.030	0.024	0.051
80.5	0.886	0.052	0.005	0.022	0.053
101.8	0.957	0.123	0.092	-0.043	0.153

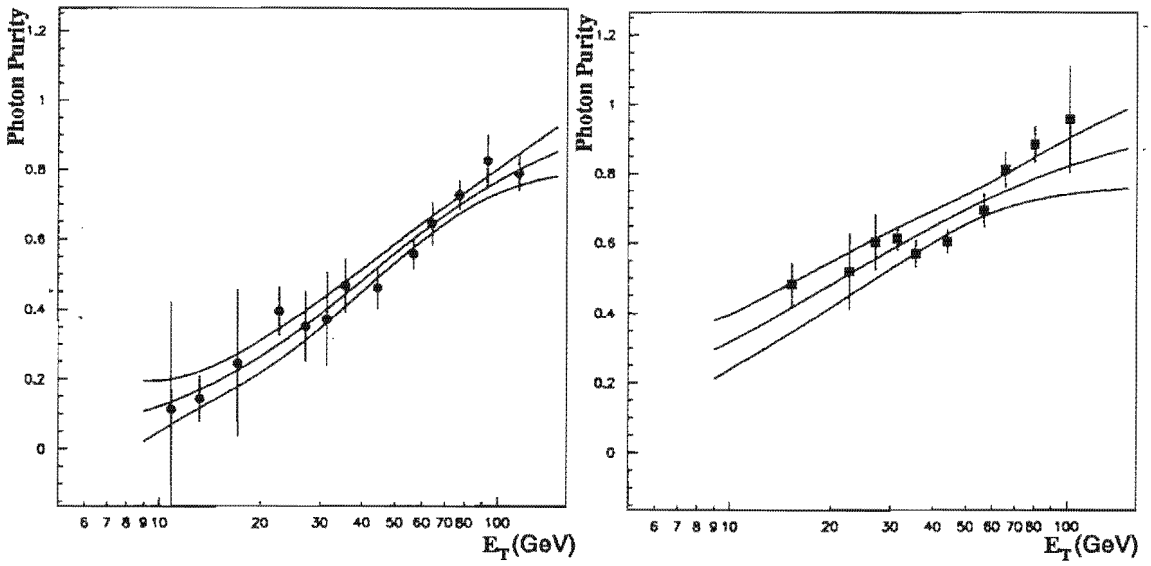

Figure 5.4: Purity vs. E_T for the central (left) and forward (right) regions.

cross sections (photon and EM jet) of rough form $a(E_T)^{-b}$. The purity is then the ratio of the photon cross section to the sum, as described by Equation 5.6. The result of the fit is shown along with the points in Figure 5.4.

While this choice of function is reasonable and physically motivated, and describes the data well, it remains an estimate of the shape of the purity curve. In order to estimate the uncertainty due to the choice of function, the alternate forms

$$P = 1 - e^{-(aE_T + b)} \tag{5.7}$$

(the form used in the Run 1A analysis) and

$$P = a + b\log E_T \tag{5.8}$$

(a straight line fit) were studied. Each gave a very similar χ^2/dof to the nominal form, and resulted in a similar curve through most of the E_T region, but varied significantly at the extremes of E_T (see Figure 5.5). The total uncertainty on the purity fit was calculated

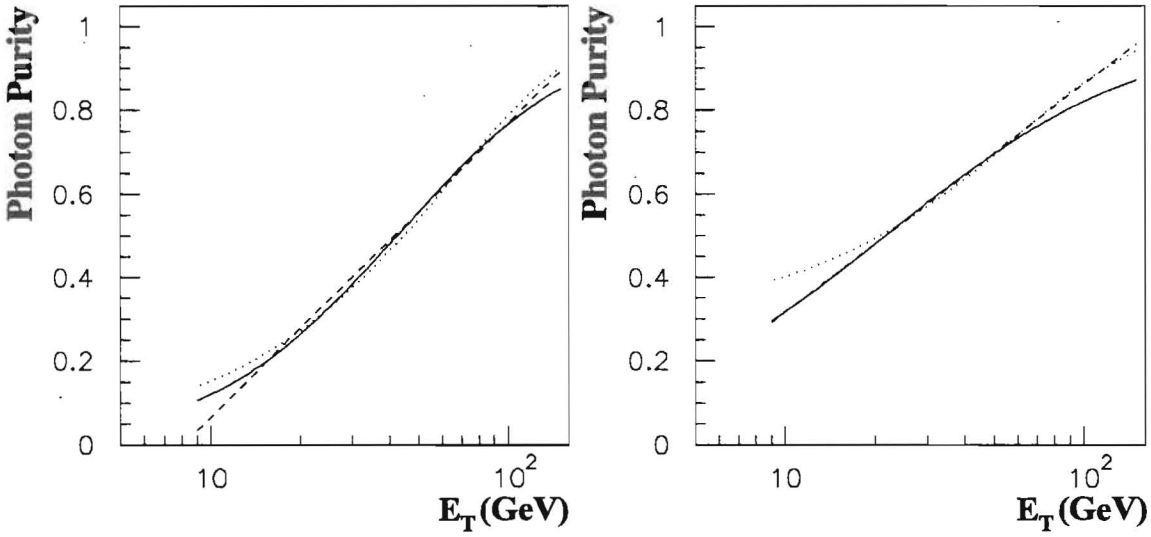

Figure 5.5: Variations in the CC (left) and EC (right) purity fits, using the nominal (solid), exponential (dotted) and straight line (dashed) fit functions.

as the error on the fit to the nominal form, augmented in quadrature by the difference between the nominal and the two alternate forms. However, because this fit dependence affects the lowest E_T points by a large fraction of their value, and because the low E_T region suffers from a lack of well determined purity points, it is difficult to extrapolate

into this region. We therefore restrict the use of the purity to values of E_T above 15 GeV, corresponding to the first measured point in the EC and the first statistically significant point in the CC.

Additionally, for the forward region, the uncertainty due to the EM1 offset was estimated by varying the nominal North & South offsets by $\pm 1\sigma$, and fitting the purity for each case. Since an increase or decrease in the offset directly shifts the purity points up or down, this results in an overall shift of the purity function (Figure 5.6). The uncertainty

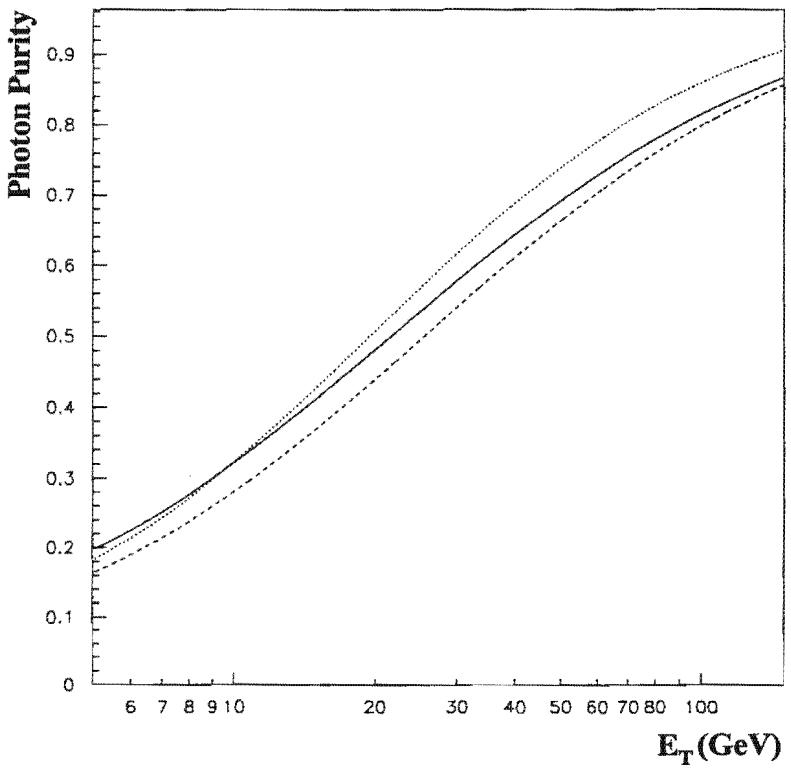

Figure 5.6: Effect of a plus 1σ (dotted) and minus 1σ (dashed) shift in the EC EM1 offset, relative to the nominal (solid) purity curve.

due to the offset was calculated as

$$\sigma_{offset} = \frac{|P_{+1\sigma} - P_{nom}| + |P_{nom} - P_{-1\sigma}|}{2} \tag{5.9}$$

where the P are the purity functions (as in Equation 5.6) for each case. This was then added in quadrature with the other uncertainties to arrive at the final uncertainty in the forward region.

Chapter 6

Cross Sections and Theoretical Comparisons

6.1 Cross Section Calculation

The differential cross section for isolated direct photon production (measured as a function of photon E_T, for specific regions of photon rapidity), is given by

$$\frac{d\sigma}{dE_T d\eta} = \frac{NP}{L\Delta E_T \Delta\eta A \varepsilon_{sel}\varepsilon_{trig}\varepsilon_{track}} \tag{6.1}$$

where

- N is the number of photon candidates in each bin of E_T and η
- P is the photon purity (as determined in Chapter 5)
- L is the integrated luminosity over which the data were taken

- ΔE_T is the transverse energy range spanned by each bin
- $\Delta\eta$ is the rapidity range spanned by each bin (both the central ($0 \leq |\eta| \leq 0.9$) and forward ($1.6 \leq |\eta| \leq 2.5$) region measurements cover a range of $\Delta\eta = 1.8$)
- A is the geometric acceptance for photons (as calculated in Chapter 4)
- ε_{sel} is the efficiency of the photon selection cuts (as calculated in Chapter 4)
- ε_{track} is the efficiency of the charged track veto (as calculated in Chapter 4)

Note that there is an uncertainty associated with the E_T binning due to the electromagnetic energy scale, which has a measured uncertainty in the central region of approximately 0.2% [19]. Since the direct photon falls steeply (of order E_T^{-5}), the resulting error on the central region cross section is taken as 1%. While the forward calorimeter is expected to perform equally well, its calibration has not yet been verified to the same precision, resulting in a 4% energy scale uncertainty on the forward cross section.

Using the components of Equation 6.1 as described previously, we can form the central and forward region cross sections; these are plotted versus photon E_T in Figure 6.1. The data points and errors are summarized for the central region in Table 6.1 and for the forward region in Table 6.2. Statistical errors on each point were calculated as the Poisson error $\sqrt{N}$. Systematic uncertainties from each component were added in quadrature to arrive at a total systematic uncertainty (plotted on each point in Figure 6.1 as horizontal

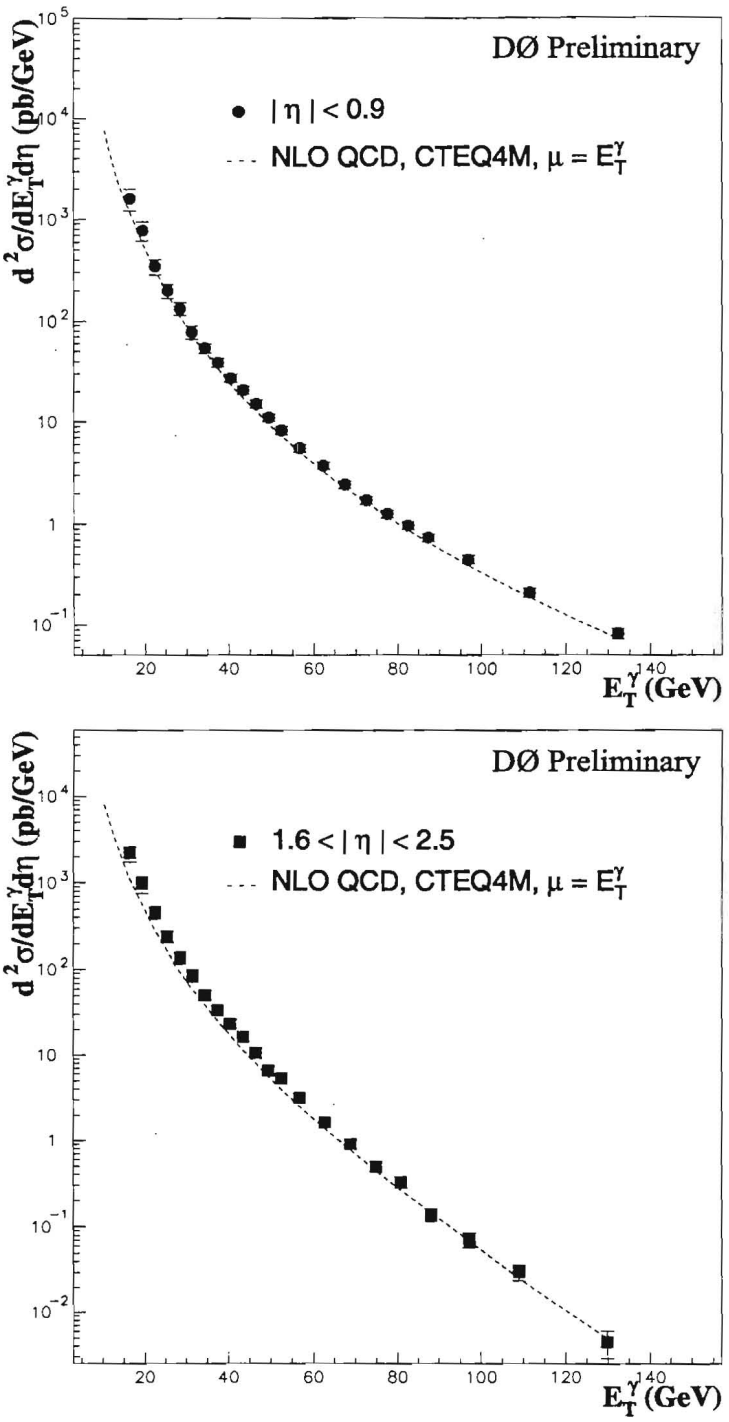

Figure 6.1: Inclusive isolated photon cross sections in the central (top) and forward (bottom) regions.

Table 6.1: Central region cross section points and errors.

E_T bin (GeV)	Mean E_T	Cross Section (pb^{-1})	Statistical Error (%)	Purity Error (%)	Systematic Error (%)
15-18	16.3	0.161E+04	6.2	22.3	23.3
18-21	19.3	0.779E+03	9.7	18.3	19.6
21-24	22.4	0.343E+03	3.8	15.5	16.9
24-27	25.4	0.198E+03	5.4	13.2	14.8
27-30	28.4	0.133E+03	6.9	11.2	13.1
30-33	31.3	0.775E+02	9.4	9.7	11.9
33-36	34.4	0.539E+02	1.5	8.4	10.8
36-39	37.4	0.388E+02	1.8	7.4	10.0
39-42	40.4	0.270E+02	2.2	6.5	9.4
42-45	43.4	0.206E+02	2.6	5.9	9.0
45-48	46.4	0.150E+02	3.1	5.4	8.6
48-51	49.4	0.110E+02	3.7	4.9	8.4
51-54	52.4	0.824E+01	4.3	4.6	8.2
54-60	56.8	0.550E+01	1.5	4.2	8.0
60-65	62.3	0.372E+01	2.0	3.9	7.8
65-70	67.4	0.244E+01	2.6	3.7	7.7
70-75	72.4	0.171E+01	3.1	3.6	7.7
75-80	77.4	0.125E+01	3.7	3.6	7.7
80-85	82.5	0.967E+00	4.3	3.7	7.7
85-90	87.4	0.731E+00	5.0	3.9	7.8
90-105	97.0	0.444E+00	3.8	4.4	8.1
105-120	111.4	0.209E+00	5.6	5.4	8.7
120-150	132.3	0.829E-01	6.5	7.0	9.8

Table 6.2: Forward region cross section points and errors.

E_T bin (GeV)	Mean E_T	Cross Section (pb^{-1})	Statistical Error (%)	Purity Error (%)	Systematic Error (%)
15-18	16.3	0.217E+04	8.0	16.2	18.7
18-21	19.2	0.961E+03	12.6	14.0	16.8
21-24	22.3	0.461E+03	4.6	12.3	15.4
24-27	25.3	0.243E+03	6.6	11.0	14.4
27-30	28.4	0.139E+03	9.0	9.9	13.6
30-33	31.5	0.865E+02	11.6	8.9	12.9
33-36	34.4	0.510E+02	1.9	8.2	12.4
36-39	37.4	0.341E+02	2.4	7.5	12.0
39-42	40.4	0.235E+02	2.9	7.0	11.7
42-45	43.4	0.165E+02	3.5	6.6	11.4
45-48	46.4	0.107E+02	4.4	6.3	11.3
48-51	49.4	0.656E+01	5.7	6.1	11.2
51-54	52.4	0.533E+01	6.4	6.1	11.1
54-60	56.7	0.318E+01	2.3	6.1	11.2
60-66	62.7	0.164E+01	3.3	6.4	11.3
66-72	68.8	0.907E+00	4.5	6.8	11.6
72-78	74.9	0.493E+00	6.2	7.4	11.9
78-84	80.8	0.325E+00	7.7	7.9	12.3
84-93	88.1	0.137E+00	9.9	8.6	12.8
93-102	97.2	0.713E-01	13.9	9.5	13.3
102-120	109.0	0.305E-01	15.2	10.5	14.1
120-150	129.9	0.447E-02	31.6	11.9	15.2

bars); as an example, the systematic errors on the central and forward 39-42 GeV bins are shown in Table 6.3.

Table 6.3: Contributions to the total systematic error on the 39-42 GeV cross section bins.

	A (%)	*E scale (%)*	ε_{sel} *(%)*	ε_{track} *(%)*	*L (%)*	*P (%)*	*Total (%)*
CC	1.0	1.0	3.5	1.6	5.4	6.5	9.4
EC	0.8	4.0	3.4	5.4	5.4	7.0	11.7

It should also be noted that the results of this analysis differ from those found in previous DØ analyses [16][2][3]. The differences, which are mainly due to improvements in the modeling of the detector and the EM jet backgrounds, are discussed in Appendix D.

6.2 Comparison with Theory

Also shown in Figure 6.1 is a next-to-leading order prediction from Baer, Ohnemus, and Owens [25] using the CTEQ4M parton distributions [31]. For this calculation both the renormalization and factorization scales were set to the E_T of the photon. The DØ photon and jet energy resolution functions were applied to the theory; this resulted in a negligible change. Also, an isolation cut was applied at the parton level to match that applied to the data.

In order to show more clearly the comparison between data and theory, the quantity

$$\frac{Data - Theory}{Theory} \tag{6.2}$$

is plotted in Figure 6.2; statistical errors are indicated on the points. The grey band indicates the combined systematic errors, some elements of which (such as the luminosity) are correlated across the E_T range.

In the central region, the data lie slightly above the theoretical prediction, but are consistent given the systematic error. In particular, the overall shape of the distribution agrees well, although a slight increase in cross section is seen in the very lowest points. Since the systematic error (mainly from the purity) becomes large at low E_T, this shape deviation is not necessarily significant.

In the forward region, the data are consistently higher than the theoretical prediction, especially in the lowest E_T bins where the data are almost a factor of two above the prediction. Also, a difference in shape between data and theory is evident in the region below ~ 40 GeV.

In order to check the effect of fitting the purity points to a functional form, the cross sections were also calculated using the same coarse binning as in the purity determination - each cross section point was then adjusted by the corresponding purity value for that bin, rather than the fitted value. The resulting (Data-Theory)/Theory plots are shown in Figure 6.3. The systematic and statistical uncertainties are plotted separately on each point; the systematic uncertainty is the error on the purity in each bin (see Figure 5.4), augmented in the forward region by the EM1 offset uncertainty (Equation 5.9). A comparison of Figure 6.2 and Figure 6.3 indicates no significant difference in shape, and in particular

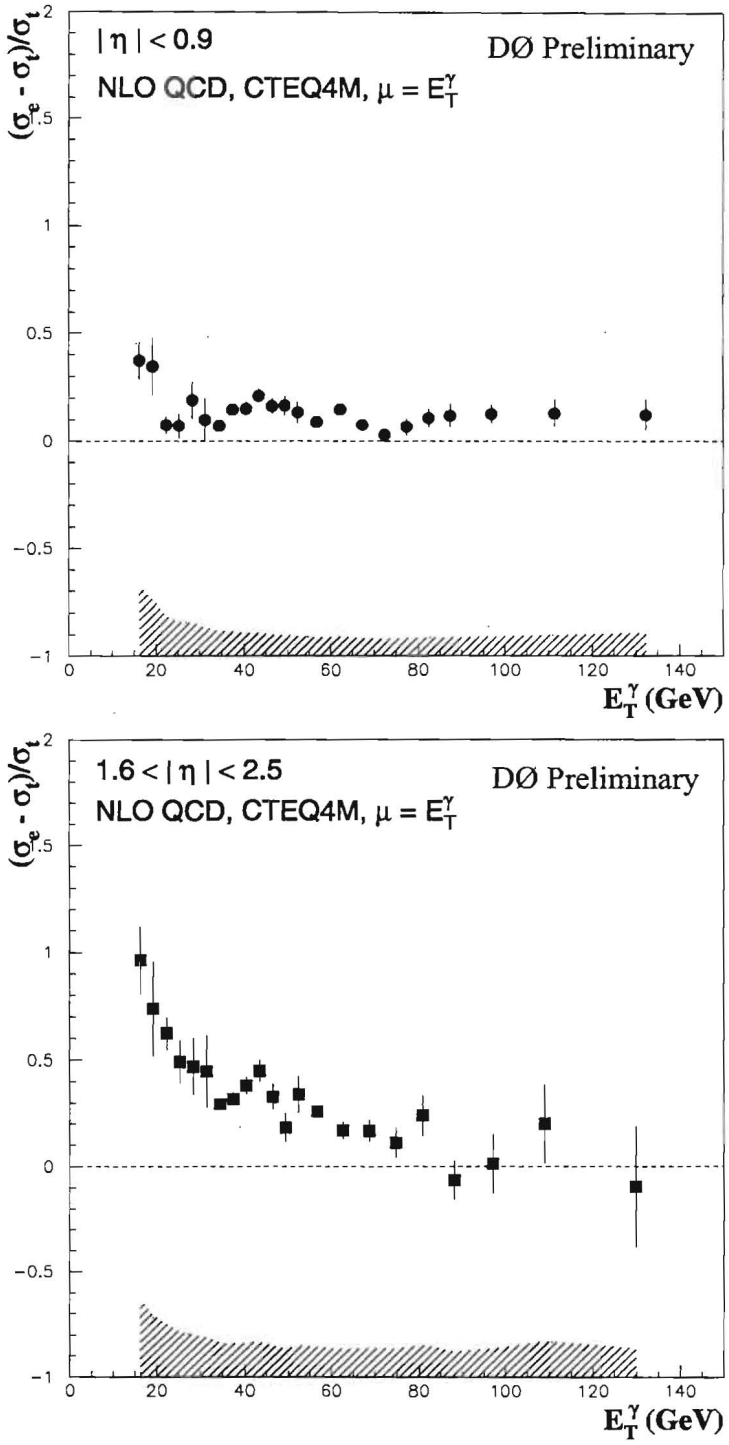

Figure 6.2: (Data-Theory)/Theory for the central (top) and forward (bottom) regions

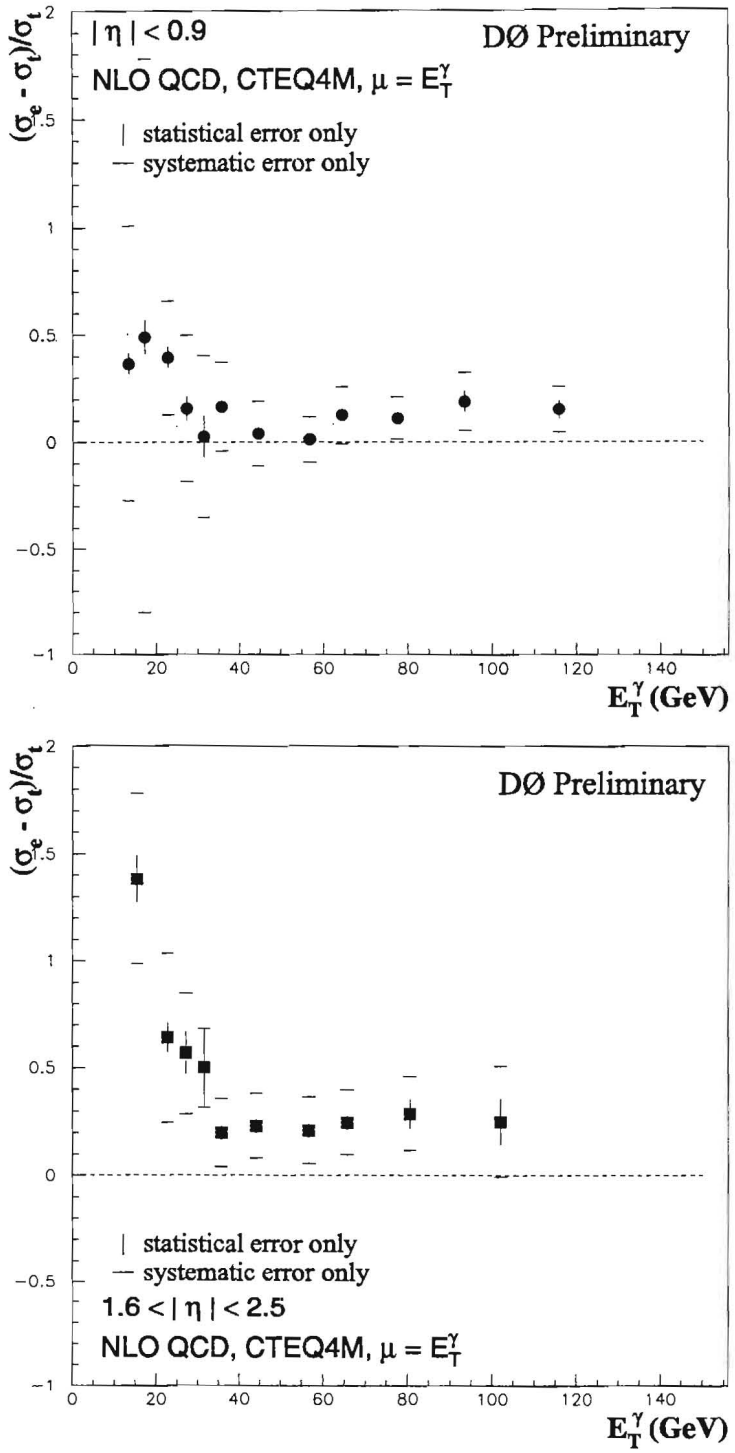

Figure 6.3: (Data-Theory)/Theory using purity determination bins.

demonstrates that the low E_T excess in the forward region is not an artifact of the purity fit.

A low E_T increase in cross section over that predicted by theory has been seen by the CDF collaboration [32] in a measurement limited to the central region only ($0 \leq |\eta| \leq 0.9$). The CTEQ collaboration, in an analysis of direct photon results from that and past experiments [33], concluded that there is a shape difference between experiment and theory which cannot easily be accounted for in the parton distribution functions. Recent theoretical work has included attempts to account for this apparent excess through soft gluon emission [34].

On the other hand, some theorists argue that the current theory is compatible with experiment given the uncertainty due to the choice of theoretical parameters [13], or that theoretical problems in implementing the isolation criteria may play a role [35]. In Figure 6.4 we show the variation of the theoretical cross section with a reasonable change of the renormalization and factorization scales, to that of twice or one half the value of the photon E_T. The resulting shift in the cross section is less than 10%, and is flat over the E_T range; however, it must be pointed out that the two scales were varied in tandem, while some of the effects noted in [13] arise from separate variation of the scales. It should also be noted that the imposition of an isolation requirement must be matched to the particular experiment to which the theory is compared - therefore, theoretical problems in implementing the cut may have different effects when comparing to different experiments.

While it is beyond the scope of this thesis to present a detailed examination of these and other theoretical issues, it is important when comparing data and theory to consider that the theoretical treatment of direct photons is an area of much current debate and

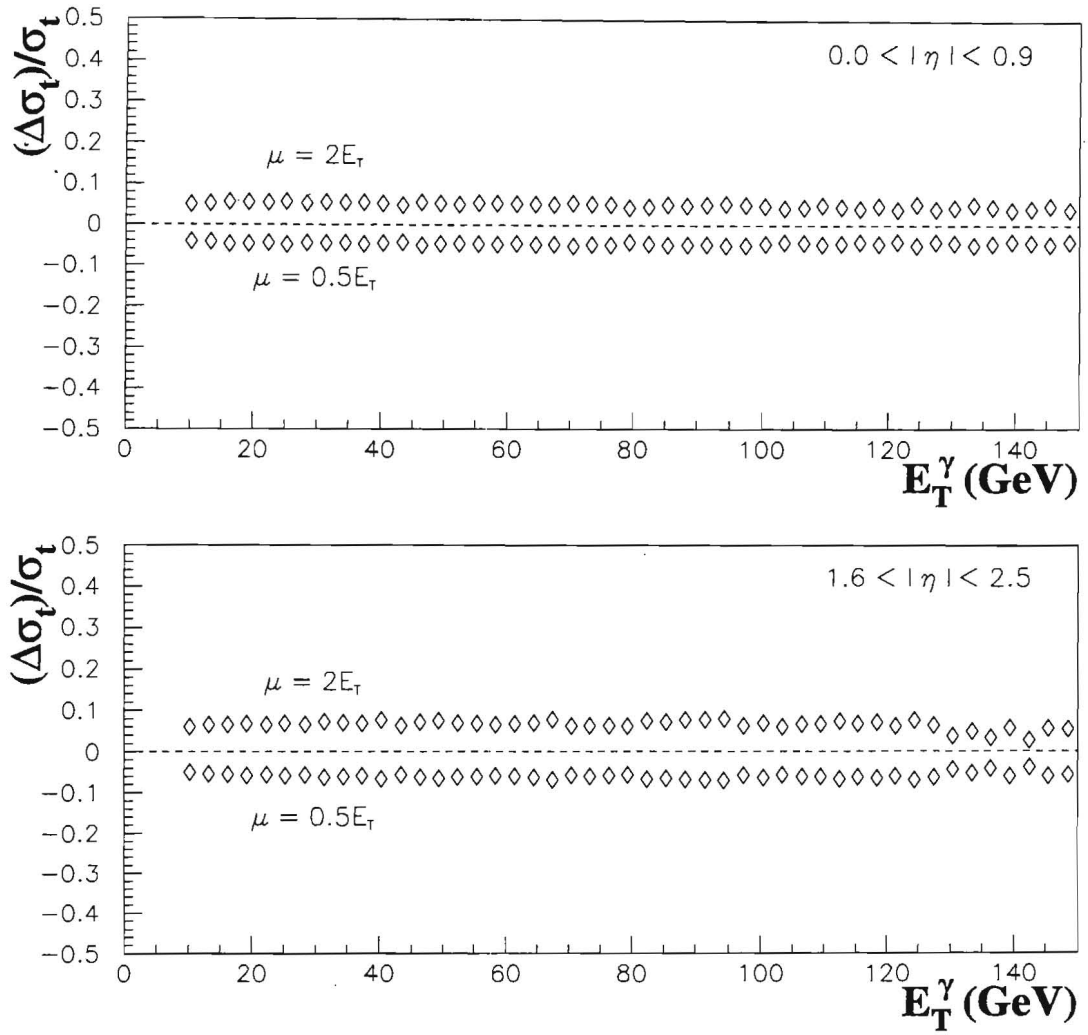

Figure 6.4: Variation of the theoretical prediction with a change in scale for the central (top) and forward (bottom) regions.

effort. To illustrate this, we consider the effect which the more recent CTEQ4M parton distribution functions have on the theoretical prediction, compared to the CTEQ2M distributions which were used in comparing previous DØ results to theory. The difference in cross sections is shown in Figure 6.5, plotted as

$$\frac{Theory(\text{CTEQ4M}) - Theory(\text{CTEQ2M})}{Theory(\text{CTEQ2M})} \tag{6.3}$$

and it is evident that the newer PDFs have some effect on both the shape and normalization of the cross section, increasing it significantly at low E_T. In addition, since the version of the Baer, Ohnemus, and Owens program used in this analysis has different heavy quark contributions and uses a different method of determining α_s than in the version used in previous comparisons [36], we consider in Figure 6.6 the total change in the calculation (PDFs and version) from that used to compare to the DØ Run 1A result, plotted as

$$\frac{Theory(\text{new}) - Theory(\text{old})}{Theory(\text{old})} \tag{6.4}$$

A shift of ~ 15% is observed fairly uniformly across the E_T spectrum. While these changes are clearly the result of refinements of the theoretical calculation, they indicate the level of precision currently achievable in our effort to measure direct photon production and derive thereby a better understanding of strong interactions.

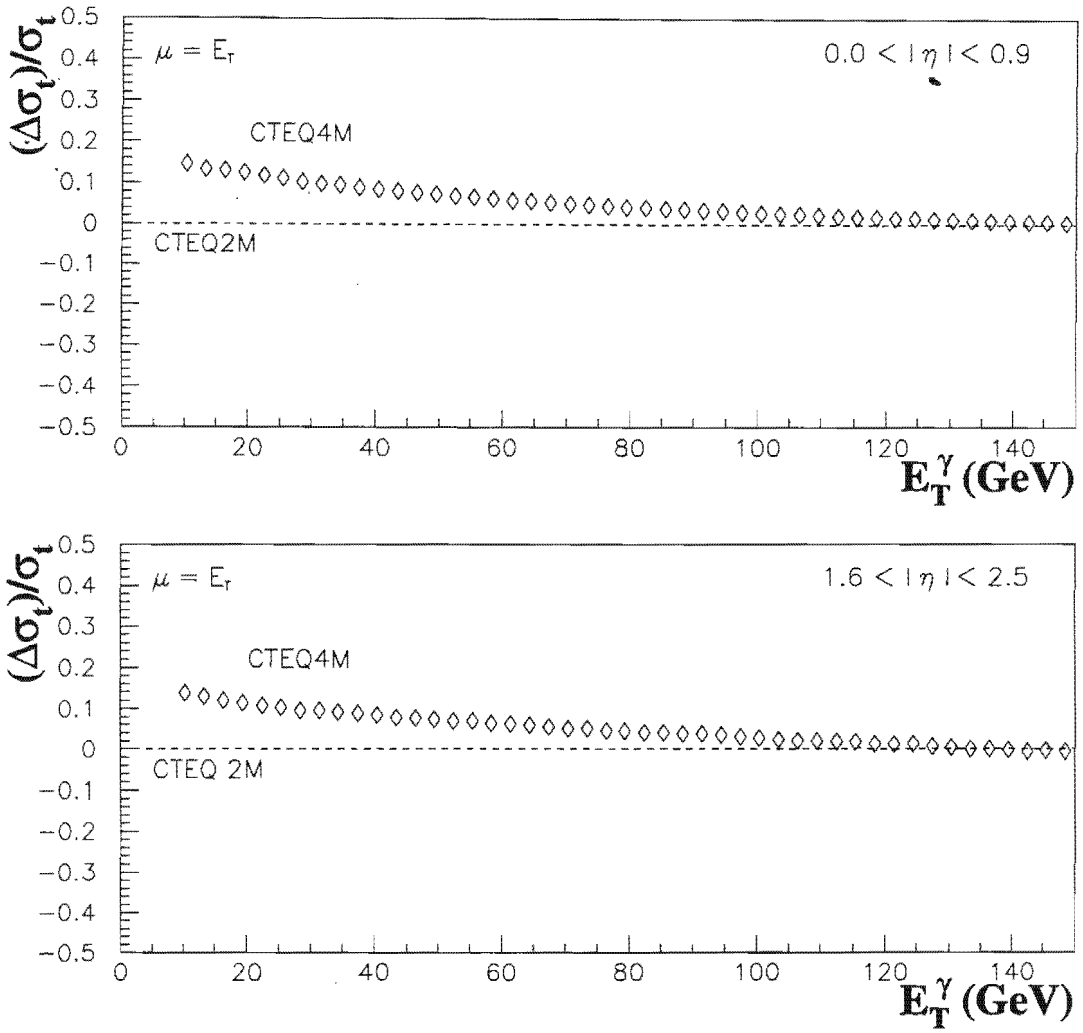

Figure 6.5: Comparison of the theoretical prediction with CTEQ2M and CTEQ4M PDFs.

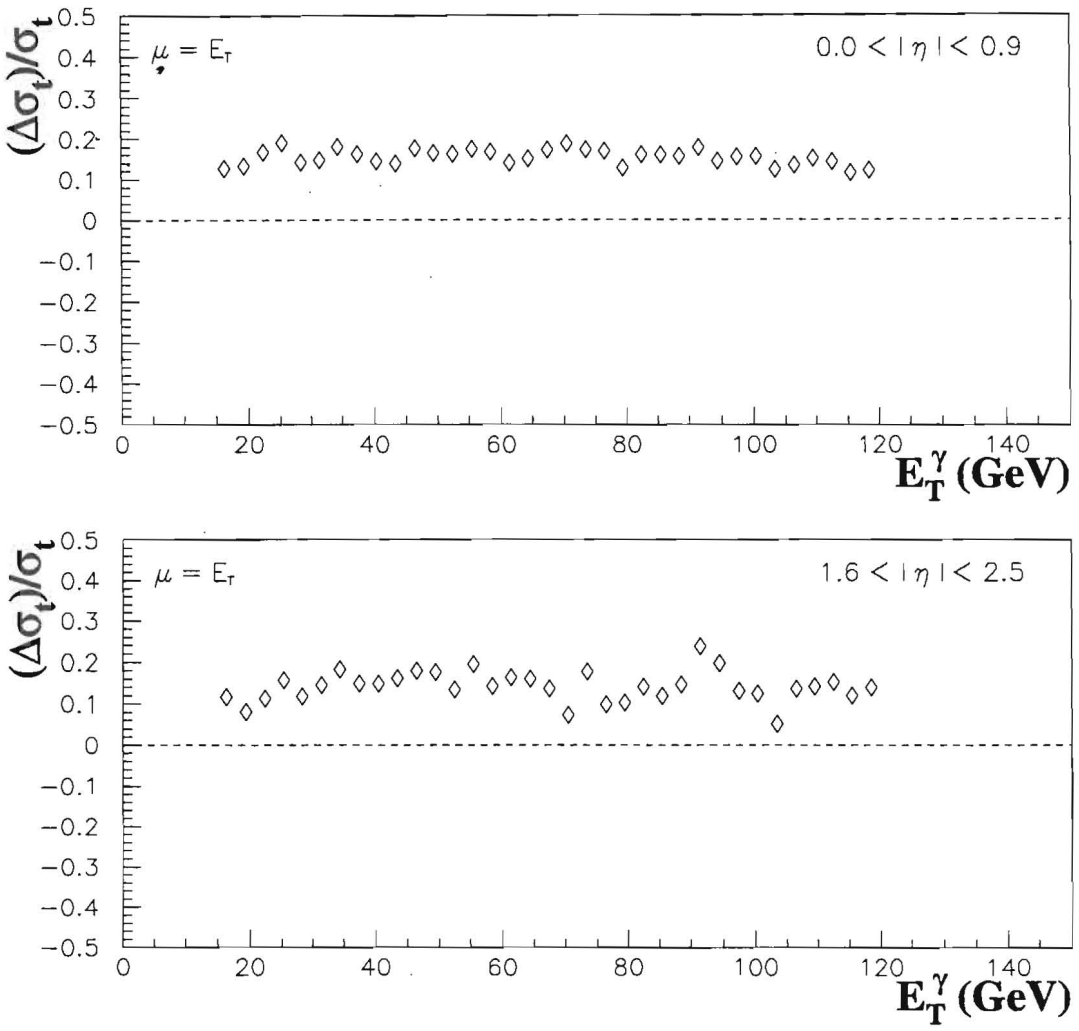

Figure 6.6: Change in the theoretical cross sections from that used in Run 1A.

Chapter 7

Photon + Jet Rapidity Correlations

7.1 Introduction

The preceding chapters have described a detailed analysis of the Run 1B direct photon sample, including the sample's purity. Following this analysis comes the ability to use the sample to investigate more than simply the total rate of direct photon production. Of particular interest is the content of the rest of the event: how many jets are produced? How are they distributed kinematically? The advantages inherent to the inclusive direct photon measurement - an unambiguous final particle, measured extremely well - also provide a good anchor against which to compare the rest of the event. Unlike dijet production, for example, in which jet measurement uncertainties cause ambiguities regarding which was the leading (highest E_T) jet (thereby muddying the associated kinematics), direct photon events have a clearly identified object against which are balanced one or more jets, typically in the opposite hemisphere of the event.

The following analysis investigates the event structure of direct photon events using a subset of the Run 1B data. While limited in scope, it indicates the type of study which can be done more precisely using the techniques and experience from the Run 1B inclusive analysis.

7.2 Rapidity Correlation Measurement

7.2.1 Motivation

As the dominant method of direct photon production at the Tevatron is that of $qg \rightarrow q\gamma$ (QCD Compton Scattering), one expects that the gluon distribution of the proton will affect not only the rate of direct photon production, but the associated kinematics. This effect can be appreciated in the following way: consider the collision of two partons which create the leading order signal of one photon and one jet (Figure 7.1). If the partons are of

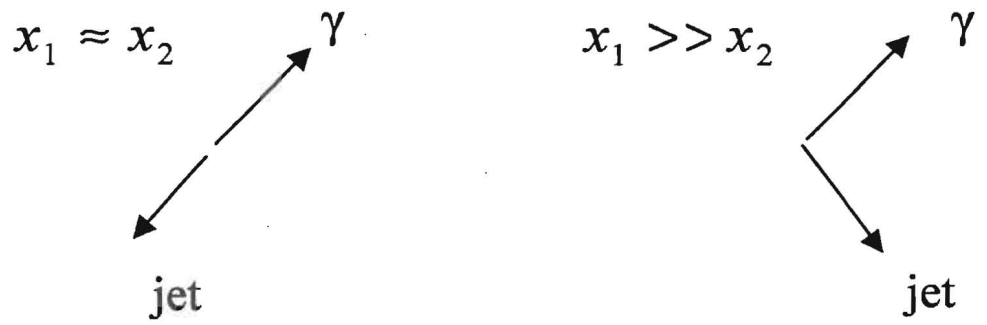

Figure 7.1: Diagram of the final state topology when colliding partons have similar (left) or very dissimilar (right) momentum fractions.

equal momenta, the system retains its center of mass back-to-back nature. If one parton is of much greater momenta than the other, the system is boosted, as the more energetic parton overwhelms the softer one, and the final state objects tend to the same side of the event. When one fixes the angle of the photon, then, one can probe a range of parton momentum fraction combinations by looking at the relative distribution of the leading jet. Since gluons typically carry much less of the momentum of the proton than do quarks, one expects that in direct photon production unequal momentum combinations will dominate, and the final state system will tend to be boosted in the direction of the incoming quark.

Also, one might expect that beyond leading order, the production of additional jets may restrict the phase space available to the leading jet, affecting its angle. Similarly, the production of soft gluons from fragmentation or color coherence effects may affect the phase space of the leading jet. It is therefore interesting to examine the correlation in rapidity between the photon and the leading jet, in order to confirm the expected event structure and to test the precision with which NLO can model it.

7.2.2 Data Selection

A sample of photon candidates was selected using the EM1_GIS_HIGH filter, and the standard photon cuts were applied, along with an additional cut on missing E_T:

- $|Z_{vtx}| < 50$ cm
- Exclude candidates with $10 \leq |\text{IETA}| \leq 15$
- Exclude candidates within 10% of a module edge in ϕ (CC only).

- Missing $E_T < 20$ GeV
- no track from any found vertex
- $\frac{E_{EM}}{E_{tot}} > 0.96$
- isolation cut: $[E_T(R = 0.4) - E_T(R = 0.2)] < 2$ GeV
- H-matrix $\chi^2 < 150$

The photons were required to have E_T above 45 GeV in order to select a region where the photon purity is enhanced. The sample was further subjected to the "golden" photon cut, which requires less than 1% of energy deposited in the EM1 layer, and which is expected to increase the purity of the photon sample since multi-photon backgrounds are, on average, expected to shower earlier than direct photons. In addition to the above cuts on the photon, standard jet quality cuts were applied to the leading jet:

- $E_T^{jet} > 20$GeV
- At least 5% but not more than 95% of jet energy in the EM layers
- No more than 40% of jet energy in the coarse hadronic layers (to prevent lost energy due to punch-through)
- Ratio of highest to next highest energy calorimeter cell < 10 (to eliminate the

effects of spurious signals)

7.2.3 Technique and Candidate Sample Behavior

The sample was binned in 5 regions of the photon pseudorapidity $|\eta^{\gamma}|$ (0.0-0.3, 0.3-0.6, 0.6-0.9, 1.5-2.0, 2.0-2.5). The "signed η^{jet}" of the leading jet in the event was then formed:

$$Signed\ \eta^{jet} = Sign(\eta^{\gamma}) \cdot \eta^{jet} \tag{7.1}$$

This quantity indicates the degree to which the leading jet is on the same side of the final state (in rapidity) as the photon. The signed η^{jet} distribution for the candidate sample is plotted in Figure 7.2. The data show a tendency for the leading jet to follow the photon candidate forward (though not fully), confirming the expected behavior. Also shown in Figure 7.2 are the mean values of the signed η^{jet} distribution for each bin.

7.2.4 Background Behavior

Since the candidate sample is not background subtracted, it is important to gauge the effect of the jet component of the distribution. To investigate this, candidates in the raw photon sample were anti-selected - i.e., selected especially to fail the photon cuts. This was done by requiring:

- $\frac{E_{EM1}}{E_{tot}} > 0.01$ (anti-golden)

- $[E_T(R = 0.4) - E_T(R = 0.2)] > 2$ GeV (anti-isolated)

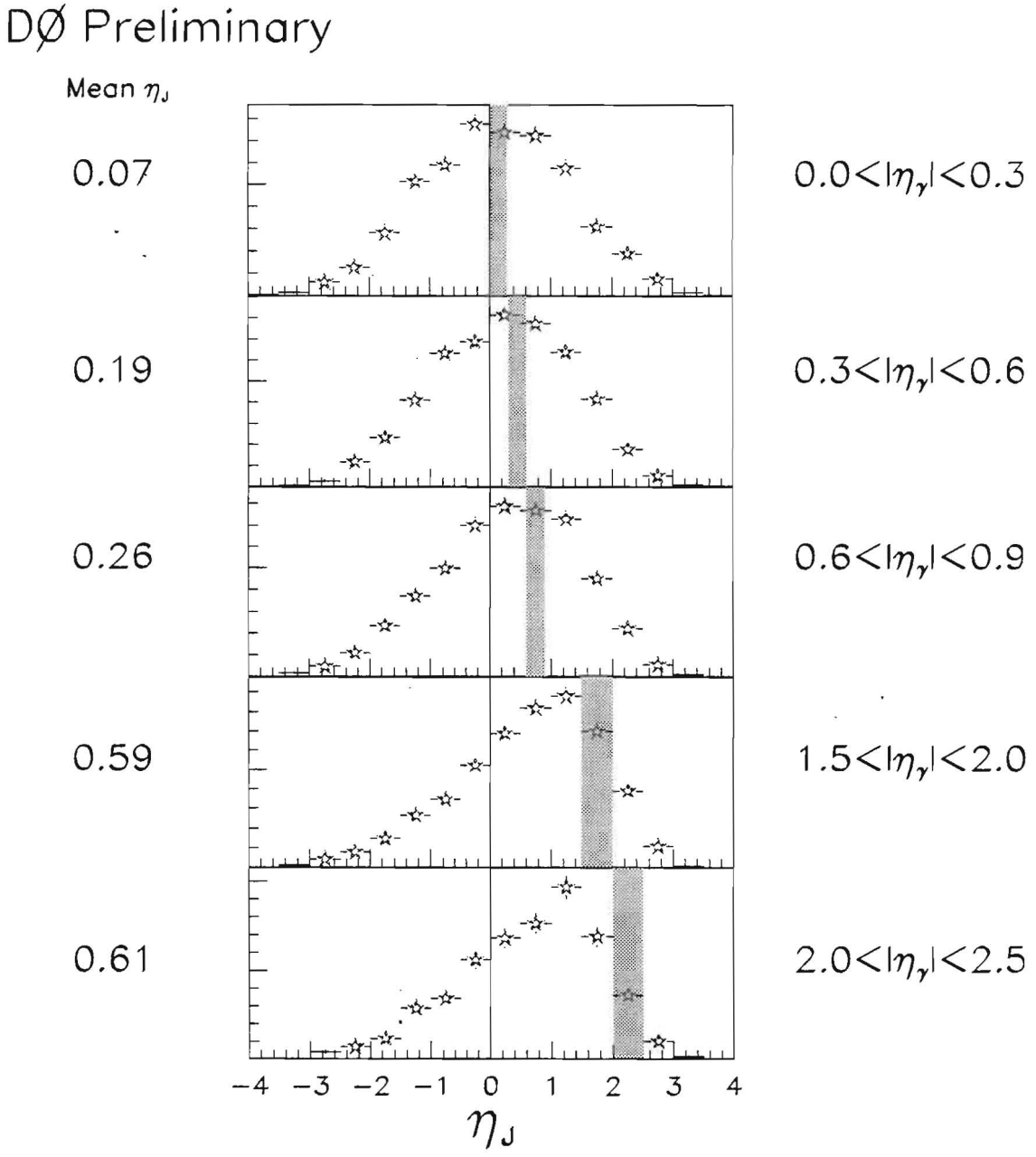

Figure 7.2: Signed η^{jet} distribution of the leading jet for golden photon candidates. The shaded band indicates the rapidity bin of the photon; shown at left are the mean values of signed η^{jet} in each bin.

as well as one or more of the following characteristics which are indicative of electromagnetic jets:

- Two or more tracks pointing to the candidate
- $\frac{E_{EM}}{E_{tot}} < 0.96$ (higher hadronic activity)
- H-matrix $\chi^2 > 150$ (poor shower shape)

with the acceptance and missing E_T cuts retained as in the golden photon case. While there is a limit to how "bad" a candidate can get, due to the trigger and reconstruction quality cuts already placed on raw photon candidates, this "bad" photon sample is expected to be mostly composed of jets which have fluctuated to electromagnetic energy. The signed η^{jet} distributions for this sample are shown in Figure 7.3, and indicate a much smaller tendency for the leading jet to follow the "bad" photon forward. This is expected, since dijet production reflects processes such as $gg \rightarrow gg$, in which the interacting partons tend to have similar average momenta.

7.2.5 Theoretical Prediction and Comparisons

Using the Monte Carlo program of Baer, Ohnemus, and Owens, a NLL QCD prediction for the leading jet behavior in direct photon events was obtained (Figure 7.4). Energy resolution smearing and a photon isolation cut matching that used on the data were applied to the prediction, which used the CTEQ2M parton distributions. Note that the

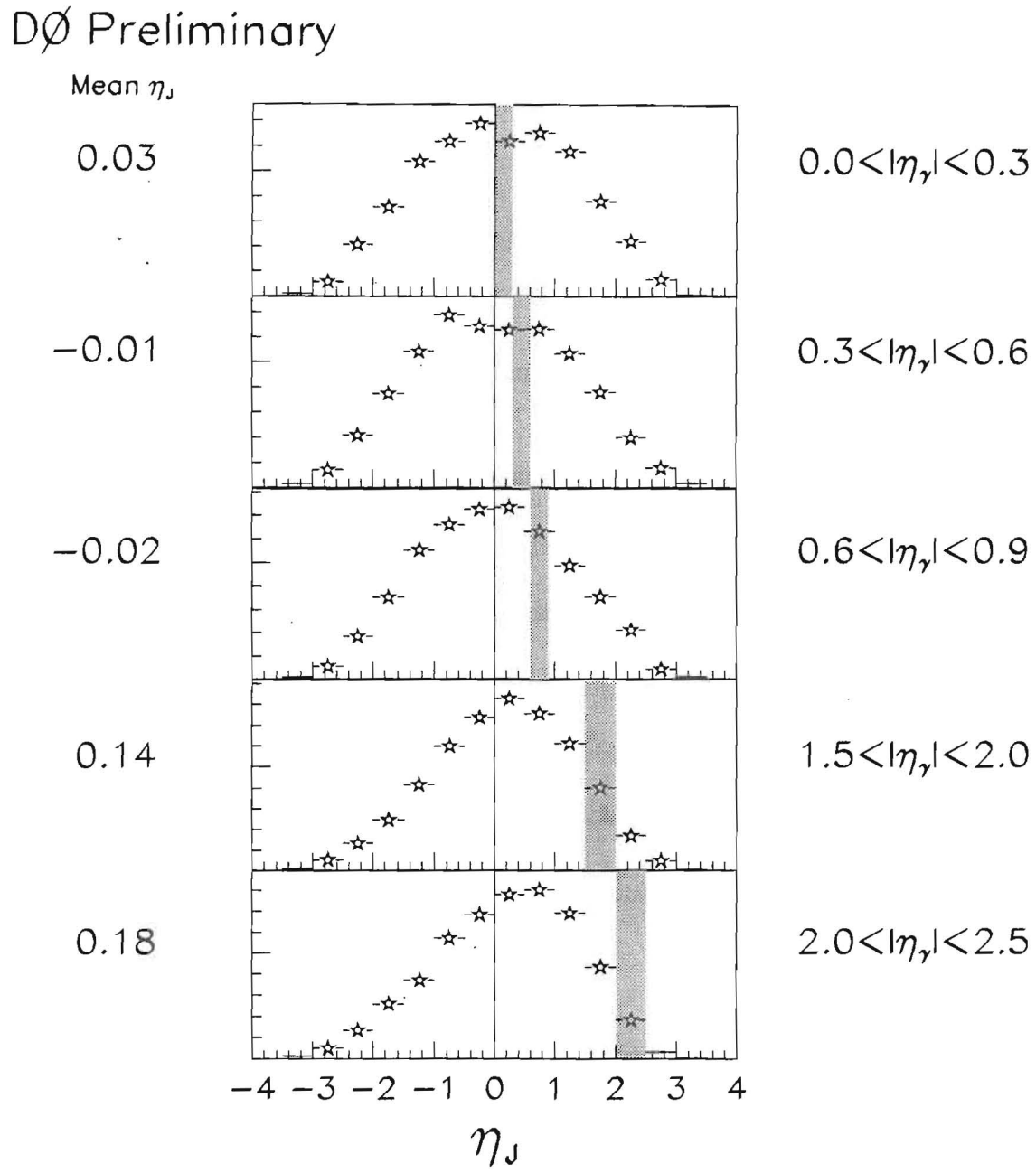

Figure 7.3: Signed η^{jet} distribution of the leading jet for background (electromagnetic jet) candidates.

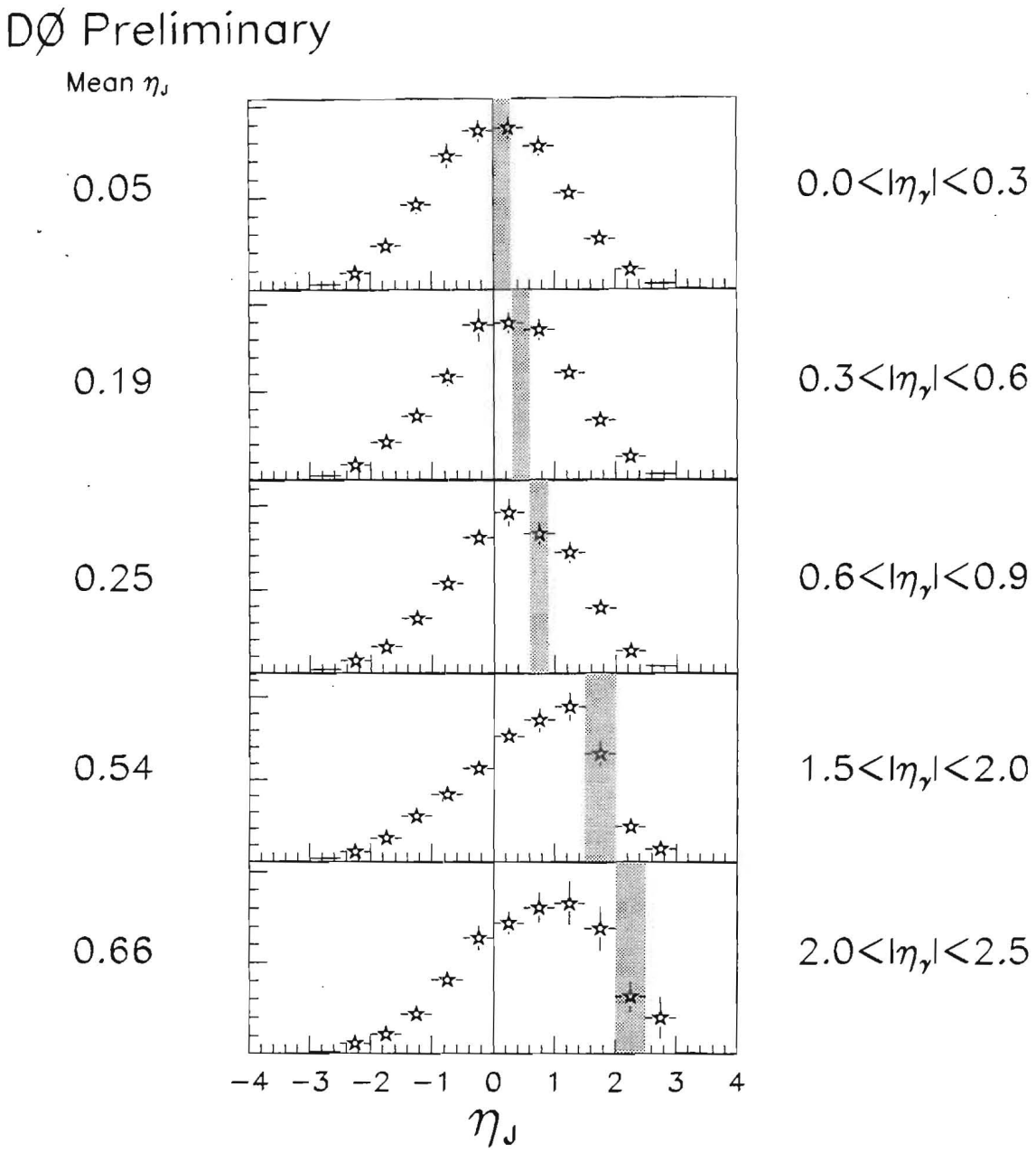

Figure 7.4: Signed η^{jet} distribution of the leading jet in a NLL QCD prediction from Owens, et al.

trend and appearance of the QCD prediction are similar to that of the golden photon candidate sample.

The means of the signed η^{jet} distributions for the candidate, background, and theory samples are plotted versus mean photon rapidity in Figure 7.5; errors are statistical only, calculated as the R.M.S. of the distribution divided by $\sqrt{N}$. While the means do not fully describe the distributions, they provide a measure of the trend in signed η^{jet}, and illustrate the evident difference between the signal and background behavior. Also, the signal-enhanced sample is seen to be qualitatively consistent with the theoretical prediction, though a fully background-subtracted comparison of distributions would be necessary to draw stronger conclusions.

To ensure that the electromagnetic jet sample has a negligible amount of direct photon signal, the behavior of this sample was cross-checked against an unbiased dijet sample. Events in the golden and background photon sample with $45\ \text{GeV} < E_T < 55\ \text{GeV}$ were compared to a sample in the same range measured as part of the inclusive dijet triple differential cross section [37]. The two samples were found to give consistent results with respect to the behavior of the leading jet (Figure 7.6), which indicates that the electromagnetic jet event sample behaves similarly to that of normal jets.

7.3 Conclusions

The analysis presented above demonstrates the utility of direct photon events in studying event structure. Future work, building on the work contained within this thesis, might be

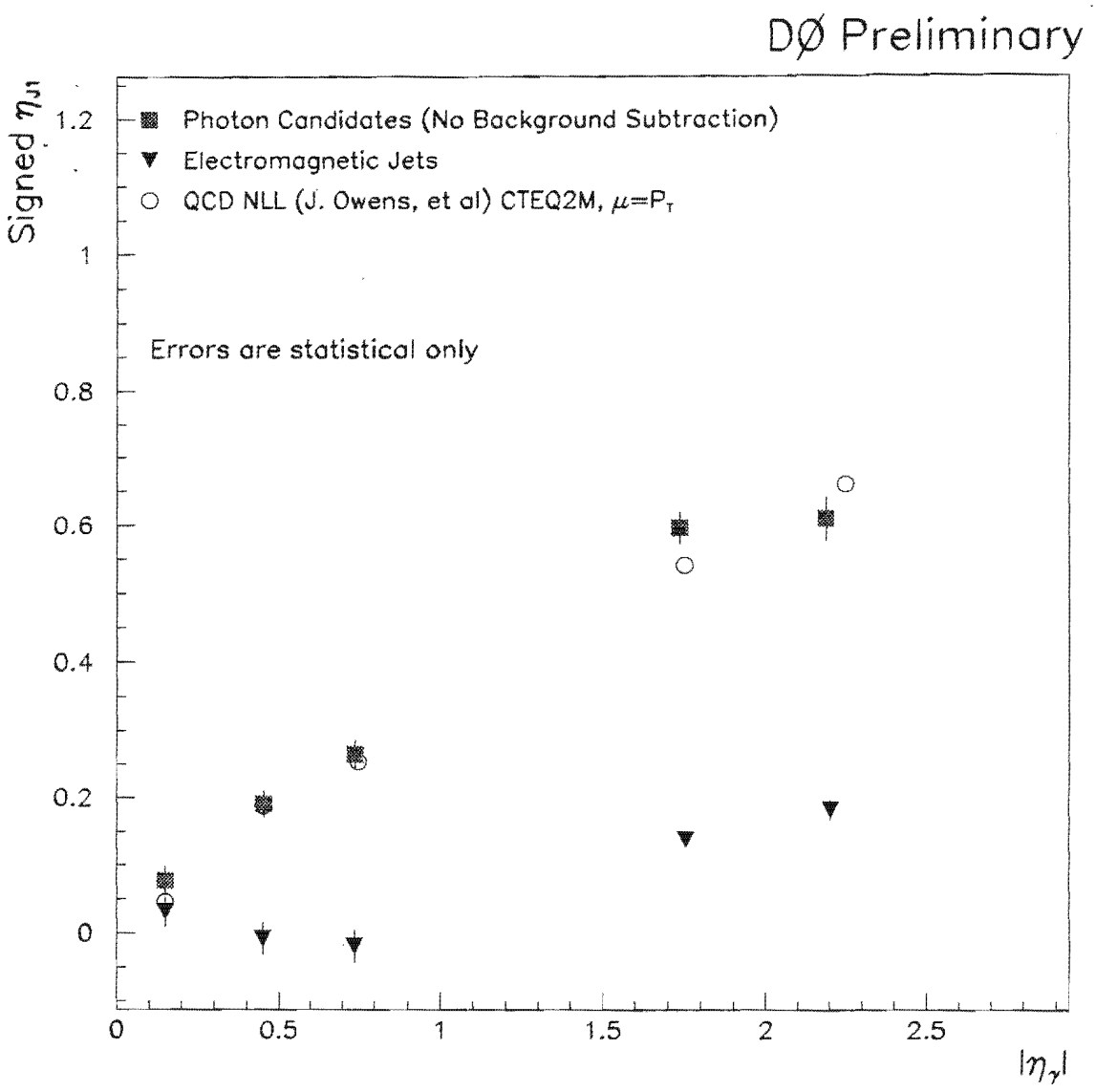

Figure 7.5: Mean signed η^{jet} versus mean $|\eta^{\gamma}|$ for candidate, background, and theory samples.

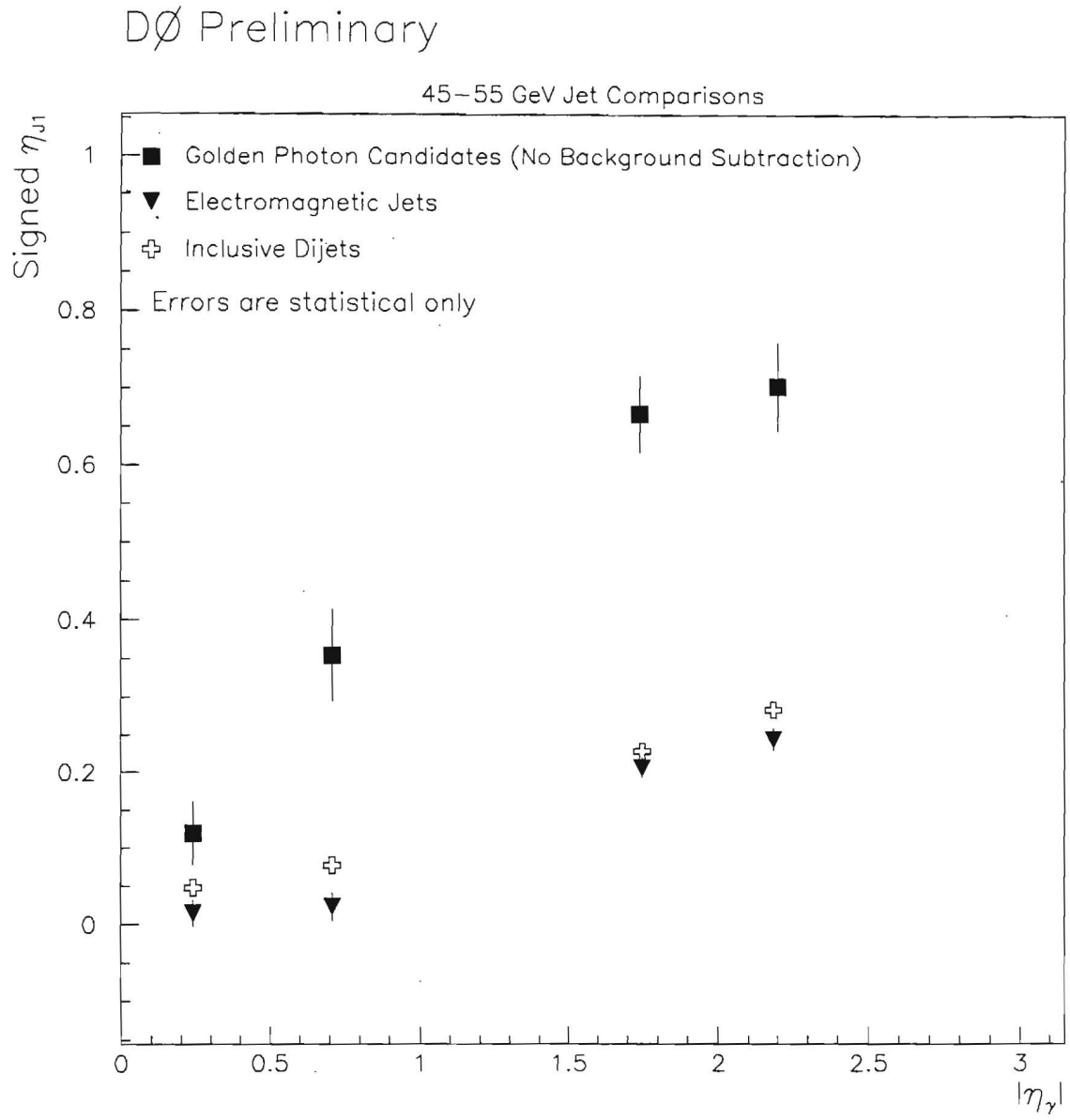

Figure 7.6: Mean signed η^{jet} versus mean $|\eta^{\gamma}|$ for candidate, background, and dijet samples with E_T between 45 and 55 GeV.

expected to extract the pure direct photon signed η^{jet} behavior using the knowledge of the background behavior, along with a purity calculation in each region of $|\eta^{\gamma}|$ as performed in Chapter 5. Studies of the ratio of events with the leading jet on the same/opposite side as the photon (essentially the ratio of events on the positive/negative sides of Figure 7.2) are currently in progress within the collaboration.

Ultimately, it can be recognized that this analysis is essentially an uncorrected, unnormalized triple differential photon cross-section, $(d\sigma^3)/(d\eta^{\gamma}d\eta^{jet}dE_T)$, integrated over the E_T region above 45 GeV. The formation of the full cross section will allow not only the comparison of event shape between data and theory, but also of absolute production rate as a function of that shape. Further, it will be informative to form the cross section in bins of E_T, extending down to lower E_T where increased effects of gluons (as colliding partons and as initial/final state radiation) might be seen; however, it is apparent from the inclusive cross section measurement that the useful range of photon E_T will be dictated by the uncertainty in the photon purity.

Chapter 8

Conclusions

This thesis has presented a detailed analysis of direct photon production at the DØ Detector, using the large statistics available during the Fermilab Tevatron Run 1B.

The analysis has relied on the excellent capabilities of the DØ Detector in measuring electromagnetic objects over a large range in rapidity, as well as its ability to trigger effectively on direct photons over a wide range of photon energies.

The ability of the DØ Calorimeter to reject the copious backgrounds from jet production enabled a signal to noise ratio of up to ~ 10. Measurement of the purity of the remaining sample was made possible by a detailed Monte Carlo simulation; improvements in the calibration of the Monte Carlo, as well as a more realistic background modeling, enabled a better understanding of the photon purity compared to previous DØ analyses.

The cross section for direct photon production has been measured, and is in mixed agreement with the QCD prediction. While the central region ($0 \leq |\eta| \leq 0.9$) cross section

shows consistent agreement with the prediction within errors, the forward region ($1.6 \leq |\eta| \leq 2.5$) cross section is consistently higher than the prediction, and further exhibits a shape difference in the lower E_T region which may indicate a need for a more complete theoretical treatment.

In addition, the structure of direct photon events was investigated by comparing the rapidity distribution of the leading jet in the event to that of the photon. Here the data and theory qualitatively agree; however, we anticipate that future analyses such as the triply differential direct photon cross section will provide a more detailed and quantitative measure of the level of agreement. We expect that this thesis will provide a useful reference for such future analyses, and hope that continued improvement in our ability to measure direct photon production will accompany the progress of the theoretical community in predicting it.

Appendix A

Triggers and Luminosity

In order to make proper account of the number of direct photon events produced and recorded during data acquisition, and hence of the cross section for production of such events, the triggering process must be understood. The purpose of this appendix is to: outline in more detail the requirements which were made at Level 1 and Level 2 to select EM showers within the calorimeter; present efficiency measurements which determine at which E_T each trigger and filter becomes completely efficient at finding photons; and discuss the calculation of luminosities for each of the filters, including cross checks which determine how well the separately triggered regions of E_T match once corrected for luminosity.

A.1 Triggering

A.1.1 Level 1 and Level 2 Requirements

The Run 1B direct photon data set was collected using four separate Level 2 filters fed from three separate Level 1 triggers - these are listed in Table A.1. At Level 1, the triggers

Table A.1: Description of triggers and associated filters.

Level 1 Trigger	L1 Threshold (GeV)	Level 2 Filter	L2 Threshold (GeV)	Requirements
EM_1_2_GAM	2.5	GAM_6_ISO_GAM	6	shape, iso(30%)
EM_1_7_GAM	7	GAM_14_ISO_GAM	14	shape, iso(15%)
EM_1_HIGH	14	EM1_GIS	25	shape, iso(15%)
		EM1_GIS_HIGH	40	shape, iso(15%)

merely required one trigger tower ($\Delta\eta \times \Delta\phi = 0.2 \times 0.2$) to have more than 2.5, 7, and 14 GeV, respectively.

While each Level 2 filter also had a different E_T threshold, they shared the same algorithm used to identify photon-like showers [38]. This algorithm first finds the most energetic EM3 cell (or "seed") in the trigger tower fired at Level 1, then forms a simple cluster by summing the cells within a $\Delta\eta \times \Delta\phi = 0.3 \times 0.3$ window around the seed in

the EM and FH1 layers. Several requirements are then imposed on this cluster:

- Energy in the FH1 layer must be less than 10% of total shower energy.
- Energy in the EM3 layer must be between 10% and 90% of total shower energy.
- The positions of all EM3 cells in a 5×5 array centered on the shower are energy-weighted and summed, forming a measure of the "spread" of the energy from the center. The same sum is made for a 3×3 array, and subtracted from the 5×5 sum, producing a quantity which should be small for electromagnetic showers; too large a value would indicate significant energy deposited further away from shower center. The actual cuts used were determined from test beam electron studies, and vary as a function of η.
- The cluster is required to have little energy in the region around it, defined by

$$\frac{E^{R=0.4} - E^{cluster}}{E^{cluster}} < f \qquad \text{(A.1)}$$

where $E^{R=0.4}$ is the energy (including the cluster energy) within a cone of $R = \sqrt{\Delta\eta^2 + \Delta\phi^2}$ centered around the cluster. The isolation fraction f was 15% for all triggers except GAM_6_ISO_GAM, for which it was loosened to 30% in order to ensure that it was less restrictive than the 2 GeV offline isolation cut.

A.1.2 Trigger Turn-On and Efficiency

Because the DØ Level 1 Calorimeter Trigger looks for energy in fixed towers, it should be expected that its ability to find all EM showers with a minimum amount of E_T will be impaired when the shower occurs near a tower boundary - some fraction of the energy will be split between two (or more) towers and neither tower may pass the trigger. This inefficiency should diminish for increasing candidate E_T, until, for candidates with twice the E_T of the trigger requirement, even sharing between towers leaves at least one tower above threshold.

While the Level 2 system is able to perform rudimentary clustering and thus avoids this problem, its E_T resolution does suffer somewhat from the limited vertex position information available at Level 2. There should also be an inefficiency at Level 2, then, which diminishes faster than at Level 1.

When using a specific filter to measure a cross section, it is desirable to determine the E_T above which that filter and its parent trigger are fully efficient - in this way, trigger efficiencies can be neglected in the cross section. It is important to note that for the direct photon analyses, trigger efficiencies are defined as the efficiency for *real direct photons* to pass the trigger, since we only care how many real photons might be left out of our measurement due to a trigger inefficiency. Thus the efficiency is studied only for events which pass all offline candidate selection cuts, and we expect the efficiency to be unity above some E_T threshold since the offline shape and quality cuts are stricter than those imposed at Level 2.

Efficiencies were measured using the D0Library L2BIT_TRIED and L2BIT_PASSED

routines - the efficiency is defined as

$$\varepsilon_{trig} = \frac{N_{tried\ and\ passed}}{N_{tried}} \tag{A.2}$$

The 7 GeV Level 1 trigger efficiency was evaluated by using special run events which passed the 2.5 GeV Level 1 trigger; the trigger efficiency is shown in Figure A.1. This

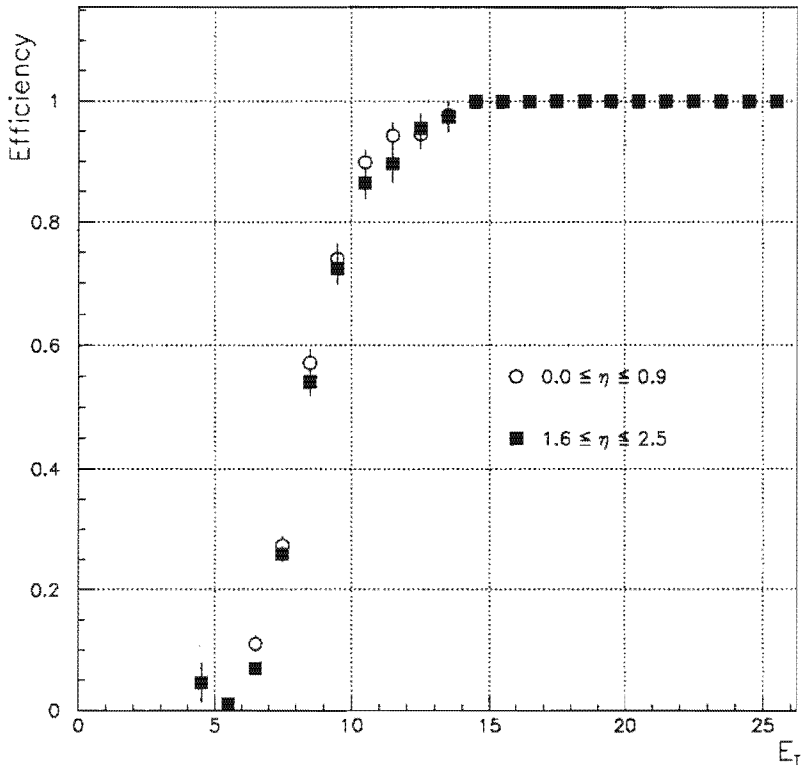

Figure A.1: 7 GeV Level 1 Trigger efficiency for the central and forward regions.

trigger is seen to be fully efficient by 15 GeV. The 2.5 GeV and 12 GeV trigger efficiencies were not explicitly evaluated; however, it is expected that they will likewise become fully efficient at about twice the threshold energy, well before the E_T at which their daughter filters become efficient.

Efficiencies for the four Level 2 filters are shown in Figures A.2 - A.5. The 6 GeV

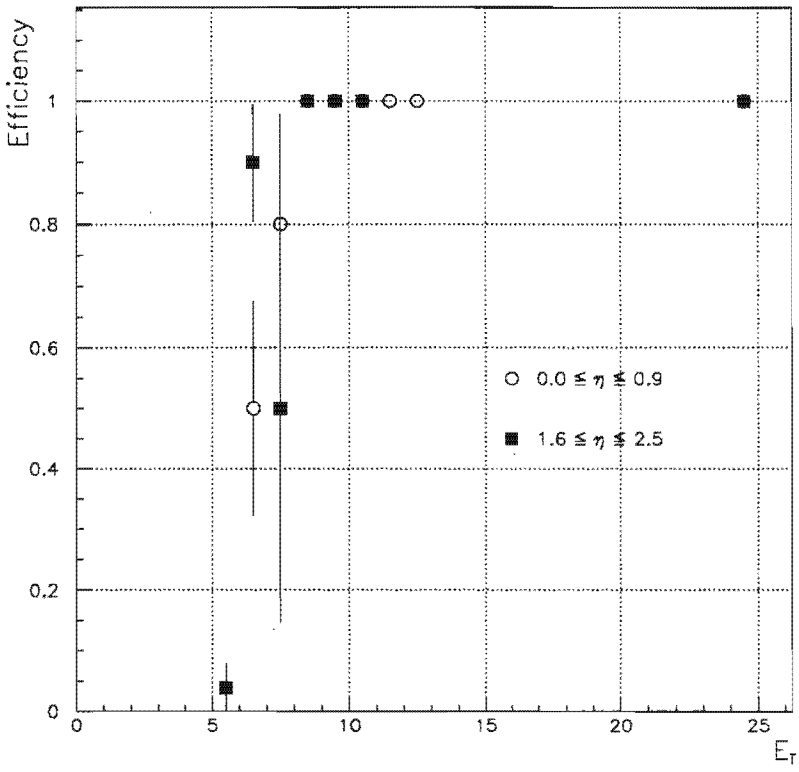

Figure A.2: 6 GeV Level 2 Filter efficiency for the central and forward regions.

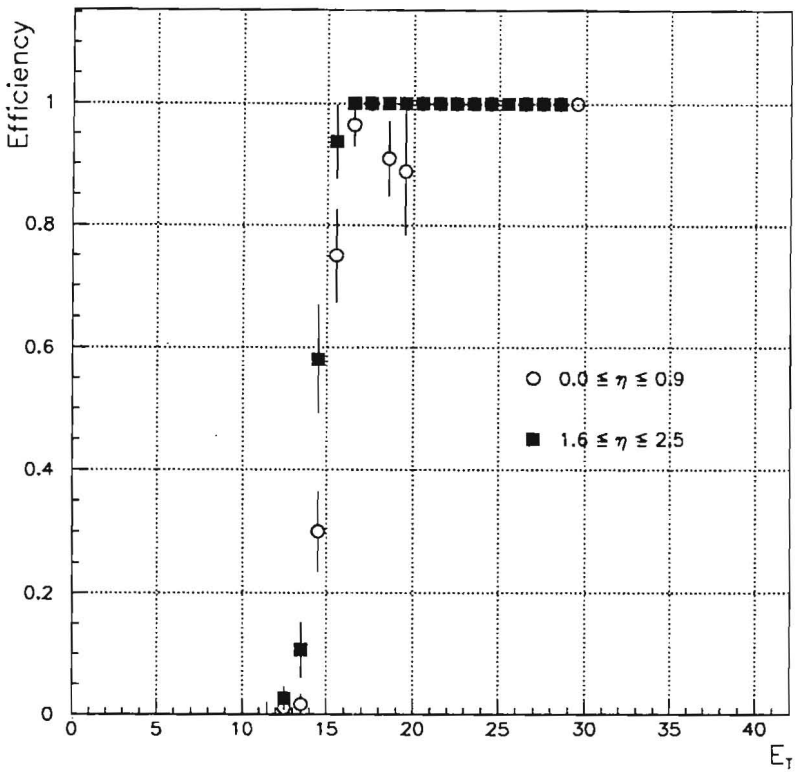

Figure A.3: 14 GeV Level 2 Filter efficiency for the central and forward regions.

trigger efficiency was evaluated using a special "mark-and-pass" run in which the photon special run filters were set to pass all events regardless of the filter evaluation. In this way an unbiased source of candidates was obtained; however, in such a sample the number which pass offline selection cuts is very small, and the trigger efficiency determination suffers from low statistics.

Efficiencies for the 14 GeV filter were determined using events which passed the 6 GeV filter, since it is fully efficient by 14 GeV and provides a sample of events which should pass the 14 GeV filter. The 25 GeV filter efficiencies were determined from the 14

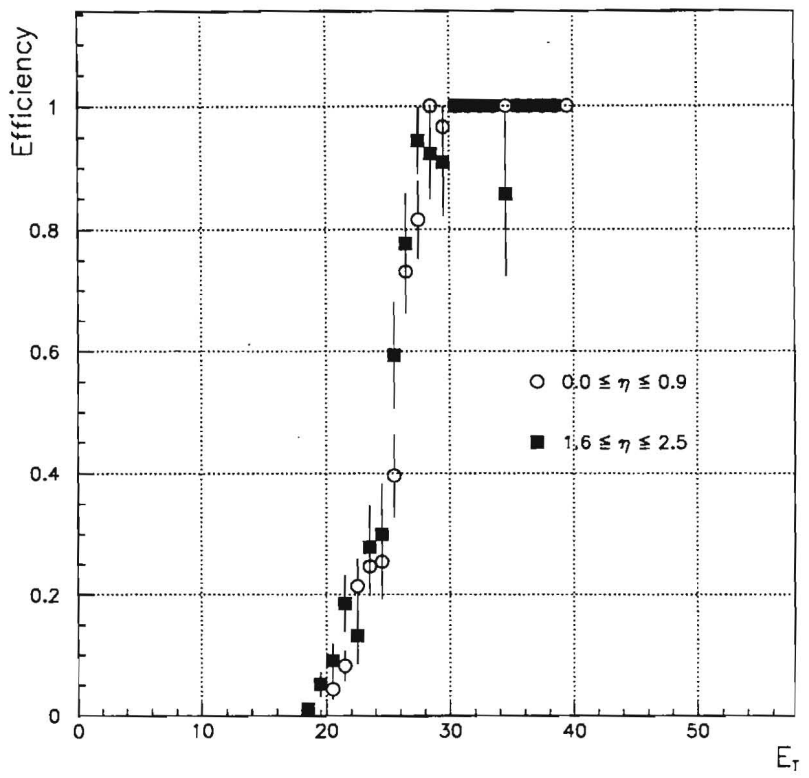

Figure A.4: 25 GeV Level 2 Filter efficiency for the central and forward regions.

GeV filter in the same way, making use of a special run filter which is identical to the 25 GeV EM1_GIS filter used in global running. The 40 GeV filter efficiency was determined using global data, checking the outcome of the 40 GeV filter on events which passed the 25 GeV filter.

Inspecting these efficiency curves, the E_T above which each trigger is completely efficient was determined to be 10 GeV for GAM_6_ISO_GAM, 21 GeV for GAM_14_ISO_GAM, 33 GeV for EM1_GIS, and 54 GeV for EM1_GIS_HIGH.

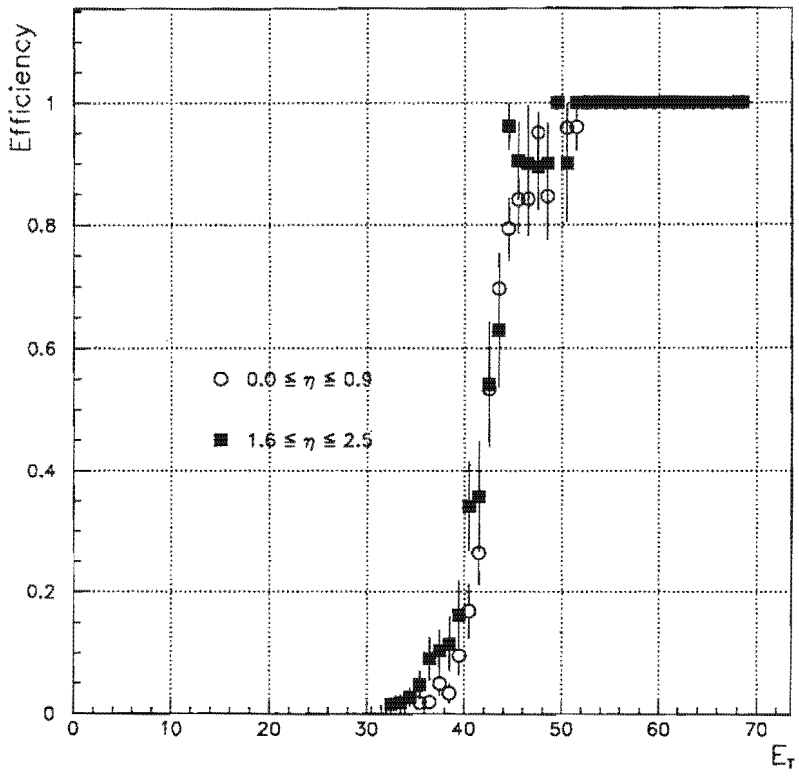

Figure A.5: 40 GeV Level 2 Filter efficiency for the central and forward regions.

A.2 Integrated Luminosity Determination

The integrated luminosity for each filter was determined using the D0 Production Database, which stores information on beam and trigger conditions for each run. The instantaneous luminosity L is determined as

$$L_{measured} = \frac{R_{L0}}{\sigma_{L0}} \tag{A.3}$$

where R_{L0} is the rate at which the Level 0 Trigger indicates inelastic collisions, and σ_{L0} is the cross section subtended by the Level 0 counters. Further adjustments are made to account for multiple interactions and other effects; the final luminosity calculation has an overall uncertainty of 5.4% [39]. Production Database utilities integrate the instantaneous luminosity readings during each run and adjust appropriately for any trigger prescales in effect for that run in order to arrive at the proper total luminosity for which the filter was active. This luminosity calculation is only valid for events which had a Level 0 vertex found within 100 cm. of the center of the detector; therefore a cut was imposed on the direct photon events to enforce this requirement (less than 2% of the events were removed due to this cut).

Luminosities for each filter were calculated for each run used in this analysis; for the two lowest filters this represents approximately 30 dedicated special runs, while for the two higher filters this spans the thousands of runs collected during 1994-1995. The resulting total integrated luminosities are shown in Table A.2.

The spectrum of good (passing all photon cuts) photon candidates passing each of the filters, corrected only by the relevant integrated luminosities and without any background

Table A.2: Integrated Luminosities for the four single photon filters.

filter	Luminosity (nb^{-1})
GAM_6_ISO_GAM	13.644
GAM_14_ISO_GAM	225.29
EM1_GIS	14577
EM1_GIS_HIGH	94657

subtraction, is shown in Figure 8.1 (CC only shown). It is expected that each of the filters should line up with the next, since correcting for the calculated luminosity and prescales should reconstruct the equivalent of a single filter allowed to populate the entire E_T region. The agreement appears good; however, a more quantitative check of this can be obtained by comparing the number of events observed by one filter to that of the next higher in an E_T region where both filters are fully efficient. We would then expect that

$$L_{lower} = \frac{N_{lower} \times L_{higher}}{N_{higher}} \tag{A.4}$$

The results of such a comparison are shown in Table A.3 and confirm that the trigger regions agree given the statistical uncertainties.

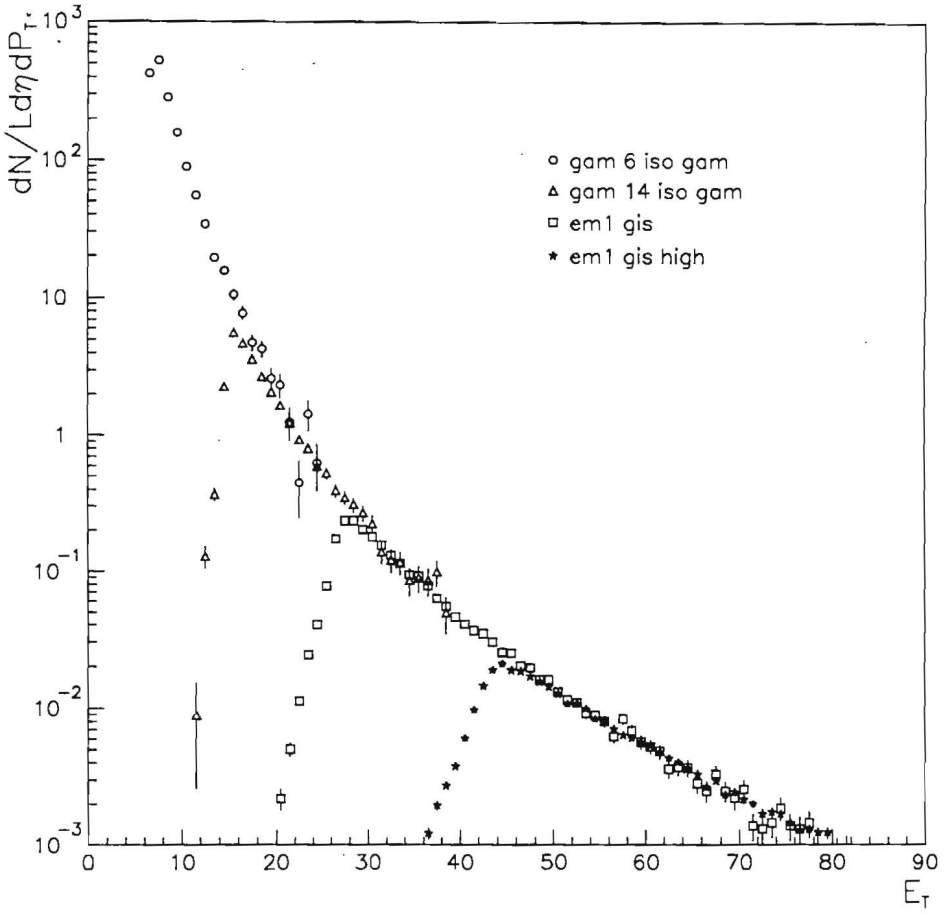

Figure 8.1: Matching of luminosity-corrected filters (CC only).

Table A.3: Comparison of luminosities calculated using Equation A.4 with those taken from the Production database.

Filter (CC)	**L_{PDB} (nb^{-1})**	**L_{calc} (nb^{-1})**	**Stat. Err**
GAM_6_ISO_GAM	13.644	12.43	1.2
GAM_14_ISO_GAM	225.29	222.8	14.3
EM1_GIS	14577	14724	367
Filter (EC)	**L_{PDB} (nb^{-1})**	**L_{calc} (nb^{-1})**	**Stat. Err**
GAM_6_ISO_GAM	13.644	14.27	1.8
GAM_14_ISO_GAM	225.29	252.3	23
EM1_GIS	14577	15970	730

Appendix B

Tracking Considerations

Since the selection of direct photon candidates requires the absence of a matching track in the CDC/FDC, it is important to determine not only the efficiency of these detectors, but also the ways in which real direct photons might be misidentified due to tracking considerations. Specifically,

- A photon might convert to an e^+e^- pair in the material in front of the CDC/FDC; only the fraction of such conversions whose track is accurately reconstructed will be removed from the sample.

- A charged track produced as part of the underlying event might overlap the photon closely enough to lie within the tracking road, in which case the photon will be removed from the sample.

The fraction ε_{track} of real direct photons remaining in the sample after the tracking cut is

then

$$\varepsilon_{track} = (1 - pt)(1 - \psi) \tag{B.1}$$

where p is the probability that a photon will convert before the tracking chambers, measured at 0.095 ± 0.00985 (0.386 ± 0.041) in the CC (EC) [16]. The tracking efficiency t is the probability that a track present in the detector will be reconstructed. The track overlap probability ψ is the probability that a reconstructed track from the underlying event will be found in the tracking road of a good photon. It should be noted that in the data set used in this analysis, EM clusters are matched to tracks from any primary vertex, although this was found to add only 4% (2%) to the number of raw candidates with tracks.

B.1 The Tracking Efficiency

The method used to measure the tracking efficiency t is similar to that employed in previous tracking efficiency studies at DØ [40][41]. A sample of $Z \rightarrow e^+e^-$ events is selected as follows:

- Select the EM2_GIS_GAM filter, which requires two EM clusters with E_T above 20 GeV at Level 2; one cluster is required to pass shape and isolation cuts, the other only shape cuts.

- Require 0 jets in the event to avoid electrons which have overlapped a jet; this

ensures a similar topology to photon events where the jet is generally in the opposite hemisphere from the photon.

- Require that the reconstructed E_T of both EM clusters be above 25 GeV.
- Require that both EM clusters satisfy the direct photon η, η^{det} cuts to eliminate the ICD region.
- Exclude EM clusters in the central region which are within 10% of a module edge in ϕ.

This selects a fairly clean sample of electrons from Z bosons. Both electrons are then checked against the following strict requirements:

- $\eta < 0.9$
- at least one track in road
- Track match significance $\sigma_t < 5\ (10)$ in the CC (EC)
- EM fraction $> 95\%$
- Isolation fraction $< 10\%$
- Hmatrix $\chi^2 < 100$
- Passed Level 2 shape, isolation, and E_T cuts

Those electrons passing these requirements are considered "tagged" as good Z electrons; the other electron is then considered unbiased and can be used in measuring the tracking efficiency. If both electrons in the event are tagged, then both are used as unbiased.

Standard photon selection cuts (minus the track cut) are then applied to each unbiased candidate. For each passing candidate, an entry is made into a histogram of the invariant mass of the two electrons (separately for CC and EC candidates). A further requirement is then made that candidates in the CC (EC) have a track with $\sigma_t < 5$ (10), and two more histograms are filled for these candidates - we then have histograms of the mass spectra for events before and after the tracking cut, for both the central and forward regions (Figure B.1).

The tracking efficiency can then be determined by calculating how many electrons from real $Z \rightarrow e^+e^-$ events were found to have passed the track requirement. To establish the level of background in the sample, we define a region S as the signal region, between 86 and 96 GeV/c^2 - this region should contain mostly real Z events with some background events. We define two equal regions on either side of the mass peak as B_1 (61 - 71 GeV/c^2) and B_2 (111 - 121 GeV/c2), which should contain only background events. Using the technique established in [40][41], we assume a linear background distribution, approximating the level of background in the signal region S as

$$N_B = \frac{N_{B_1} + N_{B_2}}{2} \tag{B.2}$$

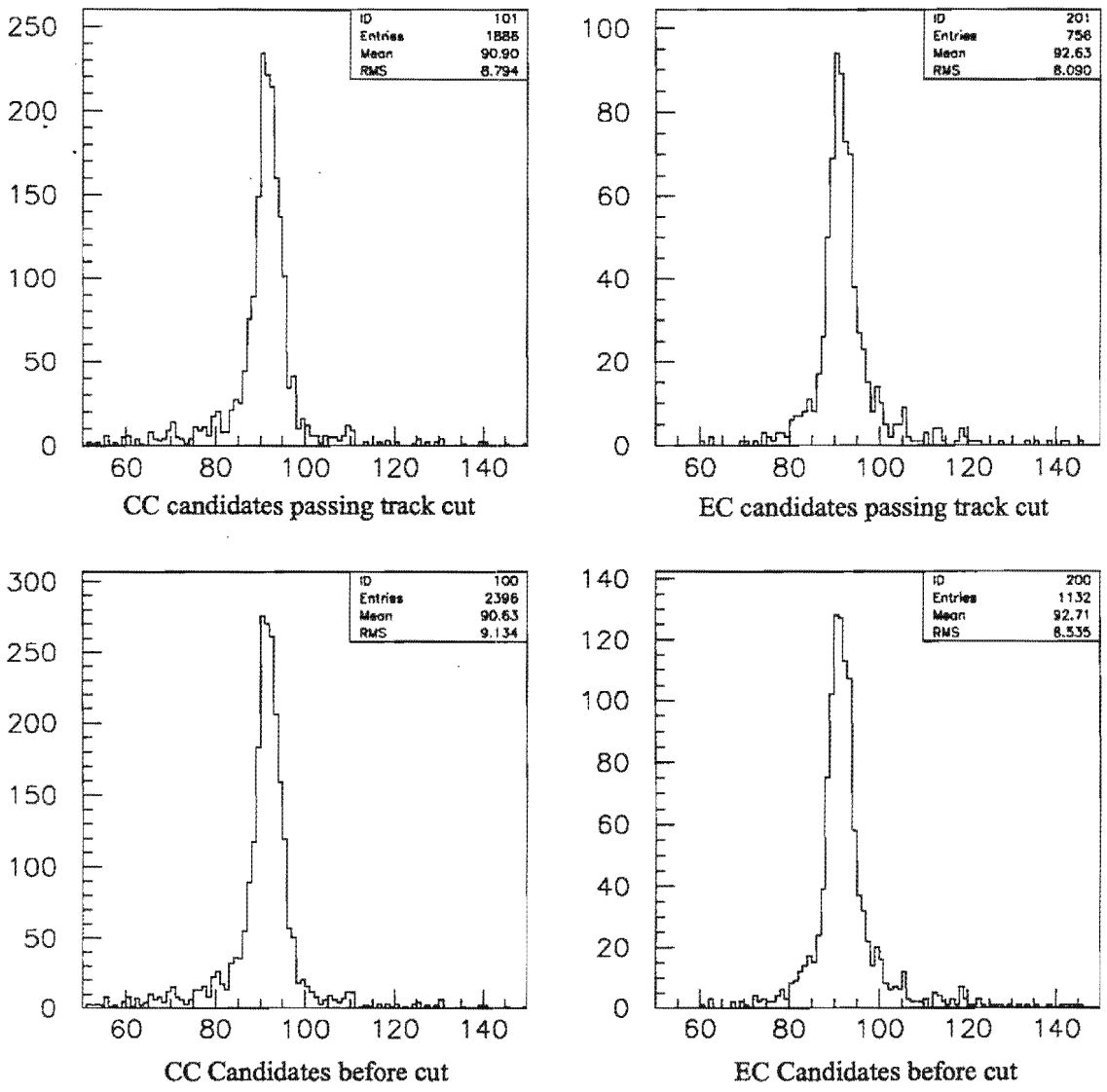

Figure B.1: Z mass distributions before and after track requirement.

in which case the tracking efficiency becomes

$$t = \frac{N_{TS} - N_{TB}}{N_S - N_B} \tag{B.3}$$

where the subscript T indicates the number in each region which have been tracked.

The resulting tracking efficiencies are shown in Table B.1, along with estimates of the background in each sample. Systematic error due to the background estimation is

Table B.1: Tracking efficiencies and errors in the central and forward regions.

	Efficiency	**Stat. err**	**Sys. Error**	**Background (%)**
CC	0.830	0.0096	0.0029	2.66 ± 0.4
EC	0.767	0.016	0.0037	2.54 ± 0.6

estimated by taking the difference in efficiency with and without background subtraction. Note that because the definition of "tracked" applied here includes a cut on the track match significance, the resulting efficiencies are lower than in [40][41]. This is necessary because, since we are considering the possibility of overlaps separately, we wish to extract the probability that an existing track which is directly pointing to the cluster (i.e., from conversions) will be seen by the tracker. Loosening the definition of "tracked" to mean simply finding a track in the tracking road would doubly count the effect of overlapping tracks.

The mean luminosity of the runs used is $6.6\times10^{30}cm^{-2}s^{-1}$ (6.6E30); runs ranged from 0E30 to 20E30. The change in tracking efficiency with increasing instantaneous luminosity is shown in Table B.2; in the central region, the efficiency decreases as the

Table B.2: Tracking efficiencies at different instantaneous luminosities.

Luminosity Range		Efficiency	Stat. Error	Sys. Error	Background (%)
0 - 3E30	**CC**	0.898	0.028	0.0066	1.7 ± 1.2
	EC	0.780	0.059	0.0043	2.0 ± 2.0
0 - 5E30	**CC**	0.860	0.016	0.0022	3.0 ± 0.8
	EC	0.814	0.026	0.0077	2.8 ± 1.1
5 - 10E30	**CC**	0.822	0.013	0.0064	2.8 ± 0.5
	EC	0.742	0.021	0.0009	2.7 ± 0.7
10 - 15E30	**CC**	0.792	0.034	0.0040	1.4 ± 0.6
	EC	0.786	0.054	0.0067	0.8 ± 1.0

luminosity goes up, which is consistent with previous studies and reflects the fact that vertex finding becomes poorer as the average number of vertices increases, causing the tracking road to be drawn inaccurately. This effect is less noticeable in the EC, due to the higher average number of tracks and the larger z region which the tracking road intercepts at smaller angles. The lowest bin, between 0E30 and 3E30, has a mean luminosity of 2.1E30, which is close to the average luminosity of the photon special runs from which

data below 33 GeV are taken.

B.2 Track Overlap Probabilities

B.2.1 Golden Overlap Method

In order to estimate the probability ψ of a random track from the underlying event to overlap a photon, a "golden" photon sample was selected from candidates which satisfied the standard photon cuts (without applying the no track cut), and which further had less than 1% of the photon energy in the first layer. This golden requirement is $> 98\%$ efficient at rejecting electrons from $Z \rightarrow e^+e^-$ events (Figure B.2), since charged particles begin depositing energy as soon as they enter the calorimeter, whereas photons must convert to an e^+e^- pair first. Any tracks in the tracking road pointing to a golden photon candidate are therefore presumed to be overlaps, rather than a real track associated with the calorimeter cluster, and the overlap probability is obtained by observing how many golden candidates have tracks. This is similar to a technique used for the Run 1A analysis.

The results of this method are shown in Table B.3. The overlap probabilities obtained are quite consistent when evaluated for samples obtained from the special runs (6 and 14 GeV Level 2 thresholds), the global EM1_GIS filter (25 GeV threshold), and the global EM1_GIS_HIGH filter (40 GeV threshold).

While this method has the advantage of using a subset of the direct photon sample, and thus matching the luminosity & trigger profiles and E_T range of the overall sample, one possible source of uncertainty in this method comes from the fact that the sample is not

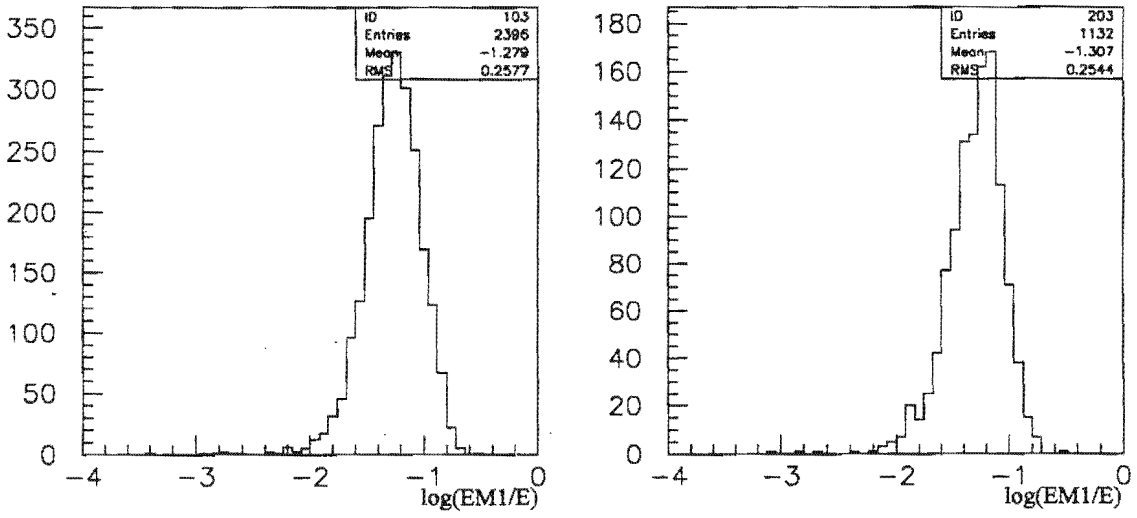

CC Z candidates

EC Z candidates

Figure B.2: Log(EM1/E) distributions for Z electrons. Note that 1% EM1 corresponds to -2.0 on this scale.

Table B.3: Overlap probabilities from golden candidate sample.

Trigger		N_T^{golden}	N^{golden}	ψ	Stat. error
Special Runs	CC	169	1558	0.108	0.008
	EC	435	2129	0.204	0.009
EM1_GIS	CC	564	5810	0.0971	0.004
	EC	1481	7105	0.208	0.005
EM1_GIS_HIGH	CC	707	7184	0.0984	0.004
	EC	1408	6485	0.217	0.005

pure photons. While the golden photon cut does boost the purity of the sample by preferentially selecting single photons over multiple photon backgrounds (which tend to convert earlier), the remaining background may unfairly add overlaps which are not from the underlying event but from jet fragmentation, which will not affect real photons. One might hope that by making the isolation or golden cuts more restrictive, a better purity might be obtained, and the overlap probabilities would approach a stable value. This was found not to be the case, as shown in Table B.4 - requiring progressively less isolation E_T

Table B.4: Variation of the overlap probability with isolation and golden cuts, varied independently using the EM1_GIS_HIGH trigger.

	Isolation E_T cut (GeV)	ψ	**Stat. Error**	**EM1 cut (%)**	ψ	**Stat. Error**
CC	2.0	0.098	0.004	1.0	0.098	0.004
	1.5	0.093	0.004	0.8	0.093	0.004
	1.0	0.083	0.004	0.5	0.081	0.004
	0.5	0.070	0.007	0.3	0.069	0.005
EC	2.0	0.217	0.005	1.0	0.217	0.005
	1.5	0.193	0.005	0.8	0.205	0.006
	1.0	0.151	0.006	0.5	0.183	0.006
	0.5	0.099	0.010	0.3	0.157	0.007

or less energy in EM1 progressively lowered the overlap probability (and removing the isolation cut greatly increased the probability). This is understood when it is considered

that the isolation E_T is in fact itself a direct measurement of underlying event activity, especially when a 2 GeV cut has been imposed to reduce the isolation E_T to approximately the level of underlying event. Similarly, the energy in EM1 is correlated with the amount of underlying event overlapping the candidate. The level of overlap is therefore dependent on the choice of cuts for these two variables. Since the isolation cut used here is the standard cut used in this analysis, it is clear that it should give the appropriate level of overlap. The cut on EM1 is less obvious; however, the level of electron rejection observed with a 1% cut appears to be a reasonable balance between allowing real associated charged tracks and overly minimizing the underlying event effect. As an estimate of the systematic error arising from these choices, the variation in ψ from varying the isolation cut from 2.0 - 1.5 GeV and from varying the EM1 cut from 1% to 0.8% were added in quadrature.

The resulting overlap probability, obtained by averaging the numbers of the two global triggers and combining systematic and statistical errors in quadrature, is then 0.0978 ± 0.010 (0.213 ± 0.026) for the CC (EC).

B.2.2 Z Overlap Method

As a cross check, an alternative estimate was obtained using the $Z \rightarrow e^+e^-$ sample. Using the same method used to determine the tracking efficiency t, an efficiency was determined for a Z electron to have an additional track in its tracking road. This probability was found to be 0.108 ± 0.008 (0.261 ± 0.018) (errors statistical only). The analysis was also performed on a sample of Herwig $Z \rightarrow e^+e^-$ events, using plate-level

GEANT, in order to estimate the probability that a Z electron would produce an extra track through bremsstrahlung and conversion, etc. After correcting for this effect, the final overlap probability using the Z sample is then 0.107 ± 0.008 (0.244 ± 0.018) with statistical error only. This agrees well with the result obtained by the primary method using golden candidates.

B.3 Overall Efficiency

Using Equation B.1, we can then construct the overall efficiency for photons to be lost due to tracking considerations:

$$\varepsilon_{track} = 0.828 \pm 0.013 \quad (0.554 \pm 0.030) \tag{B.4}$$

While this efficiency has been calculated using global run data, with a mean instantaneous luminosity of 6.6E30, substitution of the tracking efficiency t calculated in the 0E30-3E30 bin does not change the result within errors. This is due to the stability of the overlap probability between the global and special runs, and also to the constancy of the conversion probability p and its dominant error. Therefore the values calculated in Equation B.4 can be used over the entire range of the photon E_T spectrum.

Appendix C

EM1 Calibration

The observed offset in log(*EM1*/*E*) between EC Monte Carlo and EC data (Figure 5.2) directly affects the purity measurement, since a shift in the distribution of the Monte Carlo represents a shift in the position of the data between the extremes of the Monte Carlo jet and photon distributions. In order to ensure that the Monte Carlo best models the data, this offset must therefore be understood and corrected.

C.1 Offset Estimation and Origins

The most direct way to correct the Monte Carlo is to determine the offset between the Monte Carlo and data *W* electron peaks, and then apply this additive offset to the Monte Carlo photon and jet distributions used to estimate the photon purity.

The offset estimated in this way is 0.120 ± 0.011. This additive offset in log(*EM1*/*E*) is equivalent to a multiplicative correction of ~30% to the EM1 energy; or more

accurately, to the sampling weight applied to the uncalibrated energy read out from EM1. The sampling weights for the EC EM layers were determined using electrons in a test beam study of EC calorimeter modules [18]; a plate level test beam Monte Carlo, the precursor to the Monte Carlo used in this analysis, was also used in the study. It is apparent from this study [28] that

- When different methods were used to determine the sampling weights (in order to find the scheme which optimized the energy resolution), the EM1 sampling weight varied much more than other layer weights. This effect was dismissed as negligible to the goal of the study, however, since the energy in EM1 is a small (~4%) fraction of the total energy of the shower.

- The EM1 sampling weight varied depending on the amount of material upstream of the calorimeter. An attempt was made to approximate the amount of material which would be present in the real detector; however this was modeled only with a steel plate of uniform thickness.

- The EM1 sampling weight varied up to a factor of 3 between the testbeam data and testbeam Monte Carlo.

It is also important to note, as pointed out in [29], that the sampling weights determined so as to optimize energy resolution may in fact not reproduce the exact energy in any given layer. Because the energies in each layer are correlated, the ideal weight for EM1 may depend on the behavior of EM3, for example. The authors of [29] estimate that this might cause up to a 100% difference in the EM1 energy when comparing Monte Carlo and data.

However, one expects that since the sampling weights are simply multiplicative factors applied to each layer for all energies, the calibration of the Monte Carlo EM1 weights relative to the data will provide, if not the actual energy in EM1, a well-determined quantity which allows direct comparison of Monte Carlo and data to extract a background fraction.

C.2 Cross Checks of the Offset Estimate

As a qualitative check, the photon purity fitting routine (described in Section 5.3) was modified to allow the signal and background distributions to shift by an offset; the routine then minimized the χ^2 to find not only the best purity estimate, but also the best offset estimate in each E_T bin. The result is shown in Figure C.1. This method is not exact, as it relies on the fitter to determine dual quantities and their errors, but it does indicate that the purity fits prefer the Monte Carlo photon and jet distributions offset by roughly the amount determined from W electrons, with no obvious E_T dependence.

To check more rigorously the possibility that the offset might be E_T dependent, the Monte Carlo and data W samples were binned in E_T and compared (Figure C.2a); within the limited statistics, there appears to be no E_T dependence. To provide better statistics, an alternate sample of plate level Monte Carlo W electrons was obtained. These were generated using ISAJET as single particles distributed with W electron kinematics [30], and therefore cannot be compared with full data events to derive an absolute offset; however, the dependence of the offset with E_T can be studied. The analysis was repeated with this sample (Figure C.2b), and again no obvious dependence on E_T was observed.

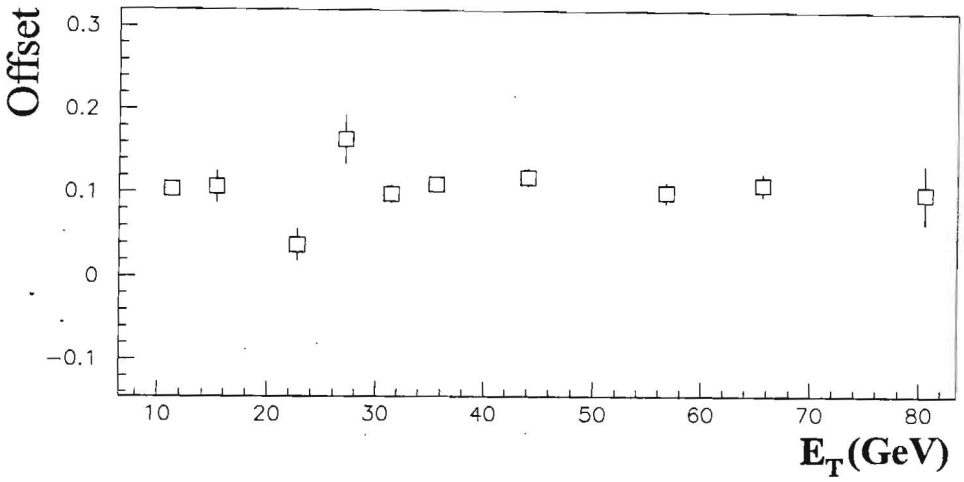

Figure C.1: Values of EC EM1 offset produced by the purity fitting routine for several E_T bins.

C.3 Effects of Pre-EM1 Material in the Monte Carlo

While the offset appears consistent with a mismatch in sampling weight between data and Monte Carlo, there is also the possibility that the DØGEANT simulation of the detector has mismodeled the amount of material in front of the calorimeter. If the amount of material were greater in the real detector than in the Monte Carlo, electromagnetic showers would tend to start earlier, develop further by the time they reach EM1, and thus leave more energy in EM1. The application of the offset in this case would still help correct the Monte Carlo, but there would be an additional, uncorrected effect on the probability that a photon converts to e^+e^- before the EM1 layer, which is precisely the discriminant we hope to exploit.

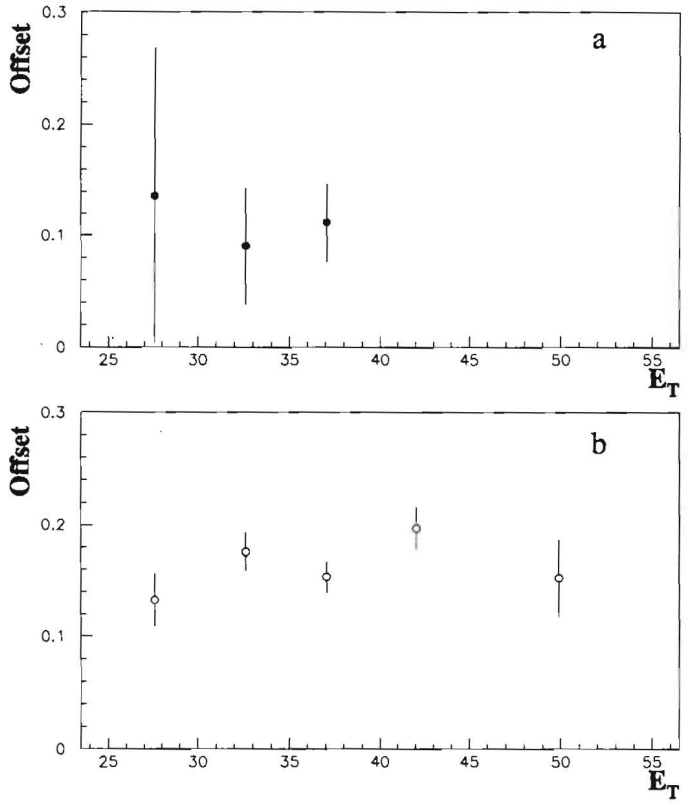

Figure C.2: Offset measured from W electrons versus E_T, using a) full W Monte Carlo; b) single particle Monte Carlo

To examine this possibility, it is necessary to understand how extra material would affect the longitudinal energy deposition of an electron shower. A model of this energy deposition was created using the formula [4]

$$\frac{dE}{dt} = E_0 b \frac{(bt)^{a-1} e^{-bt}}{\Gamma(a)} \tag{8.1}$$

where t is distance in radiation lengths (X_0), and a and b are constants determined, in this case, for 35 GeV electrons passing through uranium. Given the known ECEM layer

thicknesses of 2, 2.6, 7.9, and 9.3 X_0, we can then integrate Equation 8.1 in each layer, assuming different initial radiation lengths before EM1, and observe the effect on all layers. An initial estimate of 2.0 X_0 before EM1 was taken as a benchmark value (the design estimate quoted in [18] is $2.31X_0$). In order to better calibrate the model, a set of "sampling weights" was derived using the benchmark estimate so that the benchmark layer profile matched that of the data, and applied to all estimates:

$$W_n = \frac{F^n_{data}}{F^n_{2.0X_0}} \tag{8.2}$$

This weighting was meant to add in the effect of "optimized" sampling weights as are present in the data; however, since the quantities of interest here are relative shifts between different pre-EM1 estimates, the weighting had little effect on the results.

Figure C.3 shows the fractional energy deposited in each layer for several values of pre-EM1 material. Note that an increase in material results in increased energy in the first two layers, and a decrease in layers 3 and 4 (and in layer 5, though this is not distinguishable in Figure C.3 due to the small fraction of energy deposited there). Also plotted are the data (identical to the $2.0X_0$ points) and Monte Carlo fractional energies. Figure C.4 shows the percent (of the total shower) change for each layer between several combinations of pre-EM1 estimates, and also between the Monte Carlo and the data. For example, going from $2.0X_0$ to $1.5X_0$ results in a loss of ~1% of the total shower energy from EM1, and a gain of ~1% in EM3. Note that a difference of $0.5X_0$ results in a change in EM1 fractional energy similar to that seen between the data and the Monte Carlo; this difference is consistent between assumptions of $1.5\text{-}2.0X_0$ and $3.5\text{-}4.0X_0$, implying that

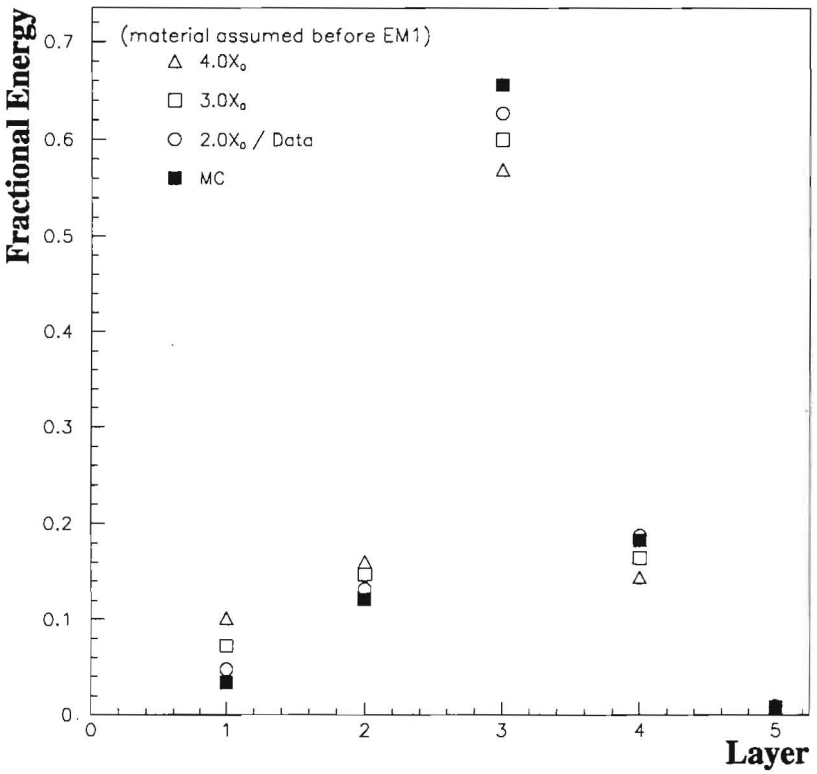

Figure C.3: Fraction of energy deposited in each EM layer for several pre-EM1 estimates (simple model), data, and Monte Carlo.

the observed changes are fairly stable over the range of realistic pre-EM1 estimates. The data/Monte Carlo EM3 difference, however, is not consistent with a $0.5X_0$ change, but with a larger change of $\sim 1.0X_0$. Most importantly, whereas the model shows that a decrease in material results in an increase in the EM4 and FH1 energies, the data/Monte Carlo difference shows a decrease in those two layers. While the model in Equation 8.1 is fairly basic, these results indicate that the difference in EM1 is not wholly due to a failure of the Monte Carlo to account for pre-EM1 material correctly. Also, since $0.5X_0$ is roughly

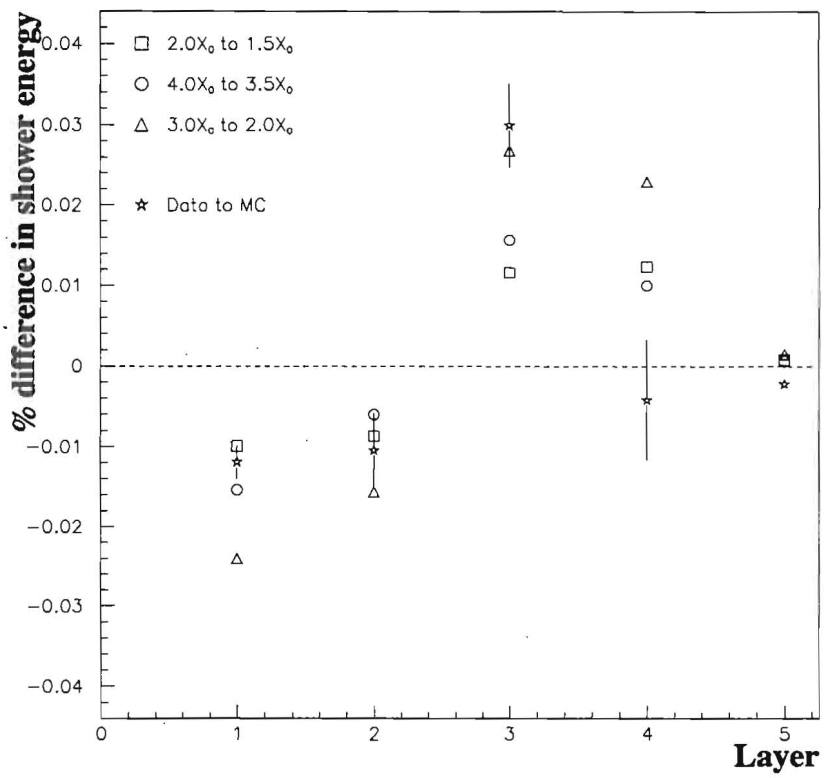

Figure C.4: Change in percent of total energy in each layer between different material estimates, and between data and Monte Carlo.

20-25% of the expected pre-EM1 material, and corresponds to roughly 1cm of steel, it is unlikely that the DØGEANT simulation would exclude this much material.

C.4 Final Calibration Determination

In order to arrive at a final correction with which to calibrate the Monte Carlo EM1 distributions, the offset was examined separately in the North and South endcap calorimeters. While the same sampling fractions are applied in both the North and South,

in calibration studies the two endcaps have been found to differ by about 2% in total response, and are separately calibrated offline. While the Monte Carlo sample was found to be consistent between the two endcaps, the data *W* EM1 distribution peaks were found to differ by a statistically significant amount, resulting in different offsets in the two regions: 0.147 ± 0.013 (North), and 0.094 ± 0.013 (South). In order to achieve the best calibration of the EM1 energy deposition, the cryostats were therefore corrected separately.

This difference was again qualitatively checked by separating the Monte Carlo photon/jet and data photon candidates into North and South samples, and rerunning the purity fitter to attempt to fit the offset separately in each cryostat. While the results of the fits (Figure C.5) show the effects of the reduced statistics, a difference can be seen which is consistent with a greater offset in the North endcap than in the South. Note that since the EM1 layer energy is such a small fraction of the total energy, the difference in total response between the two endcaps may, depending on its origin, affect the EM1 significantly. Also, while the overall offset seems unlikely to be caused by conversion material differences, and there is no expected asymmetry in the detector between the North and South, a slight difference may also contribute to the relative shift.

For completeness, the CC *W* EM1 distributions were examined in similar detail to the EC, and the data and Monte Carlo peaks were found to differ by only 0.014 ± 0.005. While this is a small difference compared to the EC offset, to maintain a consistent calibration method the CC Monte Carlo was adjusted by this factor, which resulted in a slight (~ 5%) increase in the CC cross section.

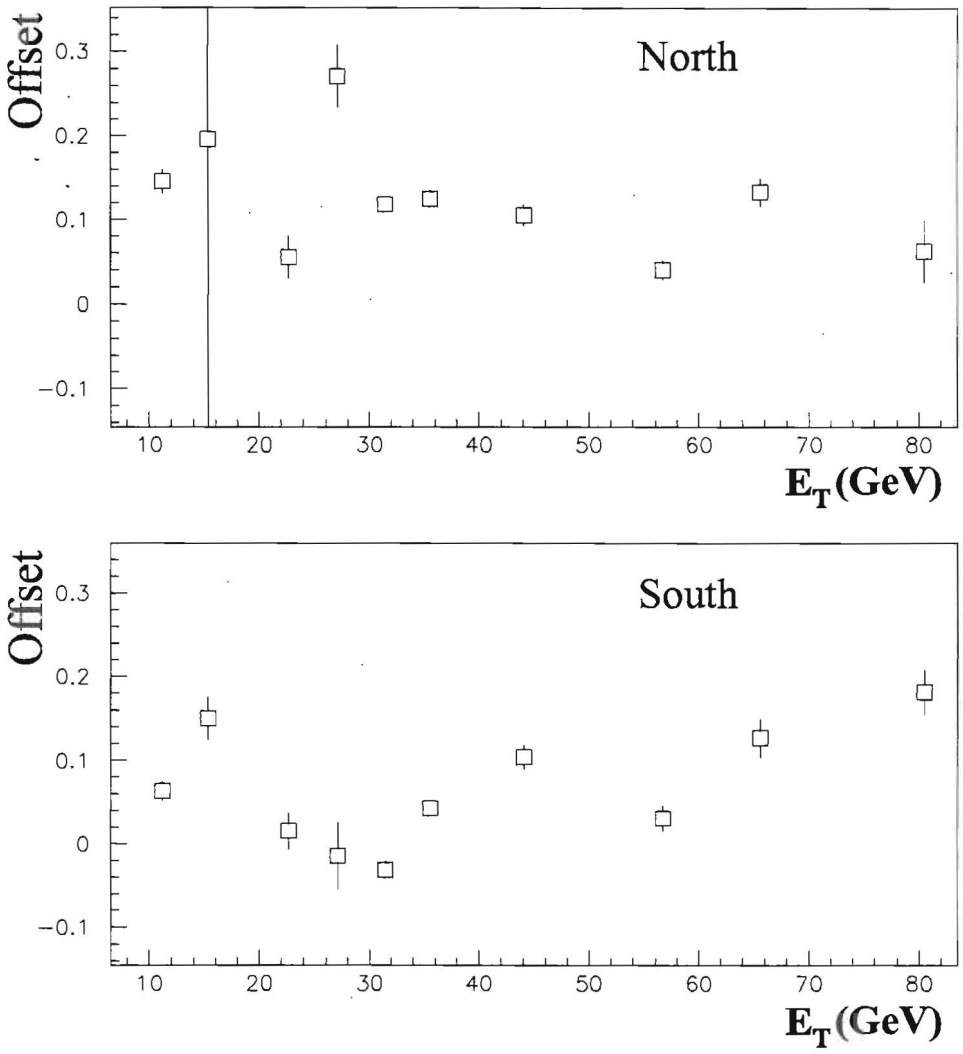

Figure C.5: Values of EC EM1 offset produced by the purity fitting routine for EC North (top) and South (bottom) samples.

C.5 Summary

The observed offset in log(EM1/E) distributions between Monte Carlo and data W electrons has been investigated, and was found to be consistent with a variation in EM1 sampling weight between data and Monte Carlo. Also, the offset does not appear to be consistent with incorrect modeling of pre-EM1 material in the Monte Carlo. In order to calibrate Monte Carlo photons and EM jets for use in determining the photon purity, we derive from the W electron comparisons a set of additive constants in log(EM1/E)

Table C.1: Additive constants used to calibrate the Monte Carlo log(EM1/E) distributions.

Calorimeter	log(EM1/E) correction
CC	0.014 ± 0.005
ECN	0.147 ± 0.013
ECS	0.094 ± 0.013

(multiplicative constants in EM1 energy). These were determined separately for the North, South, and Central calorimeters (Table C.1), and applied to the photon and EM jet Monte Carlo log(EM1/E) distributions.

Appendix D

Comparison with Run 1A Results

To compare this analysis with the Run 1A inclusive photon analysis [3], the cross section was rebinned to match that of [3] and the ratio of 1A/1B was formed (Figure D.1). In both the central and the forward regions, the Run 1A results are found to be significantly below the Run 1B measurement. It is therefore important to consider the sources of the disagreement.

D.1 Corrections to the 1A Analysis

To investigate this difference, the Run 1A analysis was reviewed, and several discrepancies were found. First, the calculated acceptance for the central region was found to be higher in the 1A analysis than in the 1B. This was found to be attributable to the IETA acceptance, which was found in the 1A analysis [16] to be 97.5% compared to the updated value (Section 4.2) of 91.7% for identical IETA cuts - a difference of 6%. Note

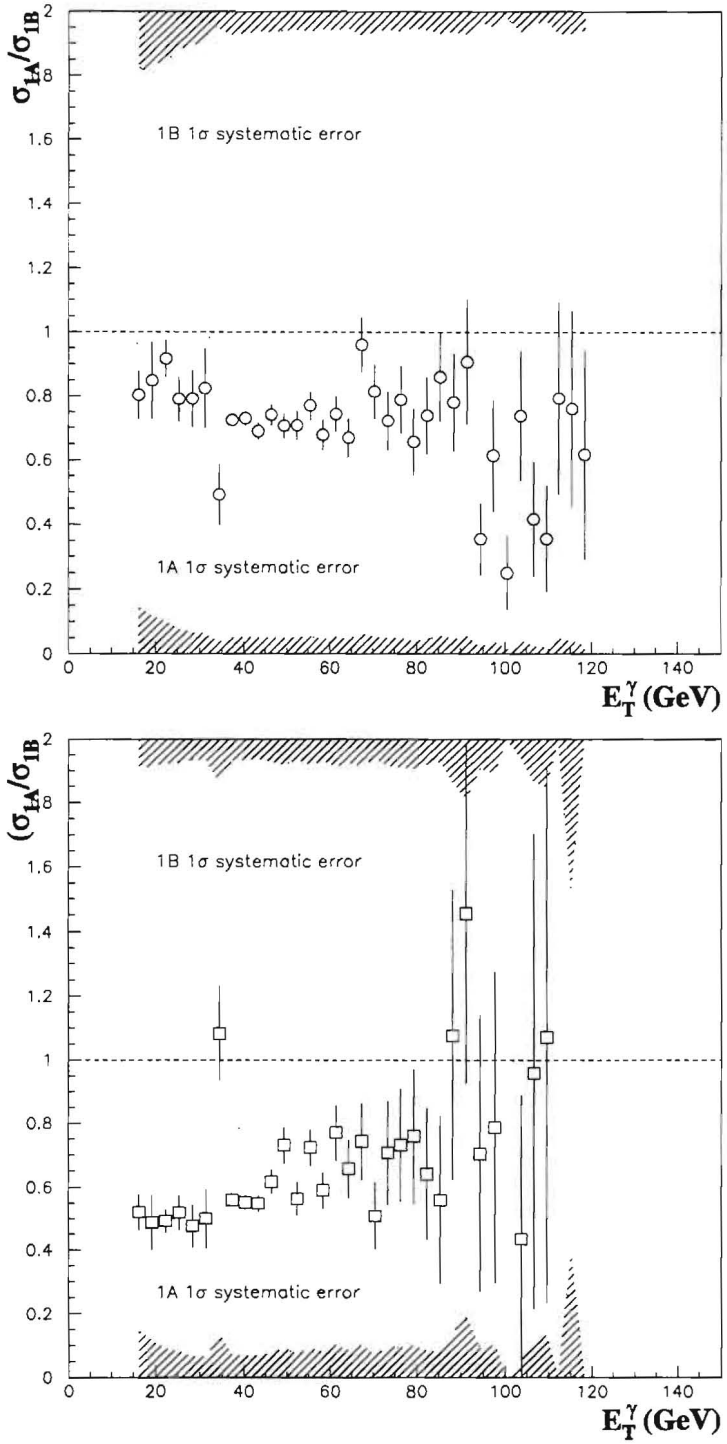

Figure D.1: Ratio of the Run 1A inclusive cross sections to the Run 1B results in the central (top) and forward (bottom) regions.

that while the 1A vertex was more off-center than the 1B vertex, in fact this should serve to lower the acceptance rather than increase it. It was verified that the actual cut used in the 1A analysis was $0 < |\text{IETA}| \leq 9$; however, the acceptance quoted in the 1A analysis is more consistent with the looser cut $0 < |\text{IETA}| \leq 10$, which had been used in earlier versions of the 1A analysis. Applying the 1B acceptance to the 1A cross section would raise the 1A result and bring it closer to the 1B.

Also, since the Production Database (which stores all run and luminosity information) has been improved since the 1A analysis was completed, the integrated luminosities for the triggers and filters used in the 1A analysis were recalculated. For the lowest E_T filters, the new numbers are 3.2% greater than those quoted in [3], which is consistent with the shift expected from a re-analysis of the DØ luminosity calculation [39]. The highest filter, however, used above ~ 30 GeV, was found to be a factor of 2.7% lower than the old, implying a 5.9% discrepancy. It was found that luminosity values for a minimum-bias filter were used for the 1A analysis rather than those calculated explicitly for the photon filters, due to Production Database difficulties existing at the time. Correcting the 1A luminosity would increase the 1A cross section above ~30 GeV by 2.7%, bringing it closer to the 1B result.

Another discrepancy is related to the fact that the 1A analysis fit a function to the efficiency-corrected purity (purity divided by efficiency), rather than simply the purity. Though the maximum value of the purity/efficiency quantity is therefore approximately 1.23, the fit was made assuming a maximum of 1.0, as would apply to the purity alone. Figure D.2 shows the effect of refitting the 1A central region purity points to allow for the

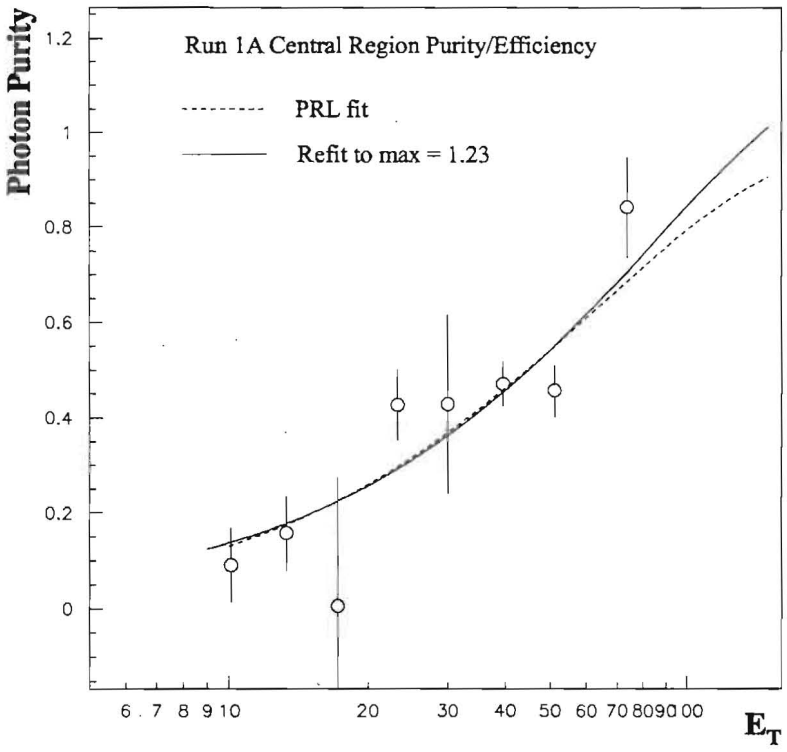

Figure D.2: Effect of refitting the Run 1A central region Purity/Efficiency to allow for the proper maximum value at higher E_T values.

proper maximum; while only the region of $E_T > 70$ GeV is affected, it is in this region that the 1A central cross section was found to deviate below the theory by 20-40%. Refitting the purity in the forward region yields no significant change, however, as the forward purity/efficiency was lower and therefore less sensitive to the maximum allowed value.

D.2 Effects of Changes in Background Modeling

The remaining discrepancies are consistent with the change in the jet background

modeling between the 1A and 1B analyses, and the statistical improvement in the number of purity points. In the forward region, of course, the dominant change is the calibration of the EM1 distribution between Monte Carlo and data, which was not performed in the 1A analysis, and therefore causes the 1A result to be lower than the 1B result. This also produces a difference in the central region, though much smaller (~ 5%).

It is expected that the "messier" nature of the PYTHIA EM jets compared to the single particle backgrounds used in the 1A analysis will tend to increase the purity of a given sample: the messier jets leave slightly more energy in EM1, increasing the difference between signal and background, as well as data and background. Since the difference between the data and the signal behavior remains the same, this results in a higher purity.

In the 1A analysis, it was found that when the fitter was allowed to compose the background sample with no restriction on the η to π^0 ratio, it chose a much higher fraction of ηs than than the expected value. This indicated that the fitter preferred more complex, multiphoton showers when trying to reproduce the data, as the η decay modes include significant $3\pi^0$ and $\pi^0\pi^+\pi^-$ states, whereas the π^0 decays almost exclusively to $\gamma\gamma$. This, along with examination of quantities such as the single particle isolation E_T distributions, gave evidence that the single particle Monte Carlo did not perfectly approximate EM jet behavior, and (along with an increase in available processing power) led to the generation of PYTHIA jets as an improvement for the 1B analysis.

To demonstrate the improvement in background modeling, a "composite" sample was created by combining the 1B Monte Carlo photon and jet candidates in the fractions indicated by the 1B purity, and then plotting other quantities of interest (EM fraction, H-

matrix χ^2, and isolation E_T) and comparing to the data distributions. These comparisons are presented in Appendix F; one example of interest is the composite isolation E_T distribution. There is generally good agreement between the Monte Carlo and data; when compared to a similar study done in the 1A analysis [16], the improvement from the 1A analysis can be seen.

In another study [43], the Run 1B PYTHIA Monte Carlo was used in place of the Run 1A single particle Monte Carlo to refit the 1A candidate sample and rederive purity points in the CC. Figure D.3 (left) shows the original 1A purity points (without the efficiency

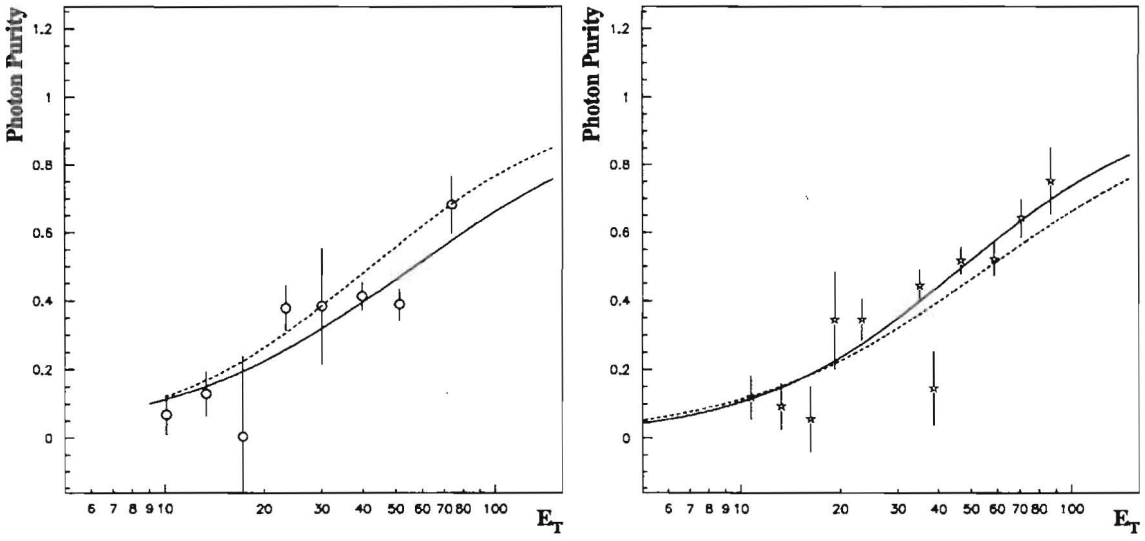

Figure D.3: Left: Run 1A CC purity points and resulting fit (solid line), along with the 1B CC purity fit (dashed line). Right: 1A purity points and fit (solid line) using the 1B Monte Carlo, along with the 1A fit (dashed line, same as solid line on left).

correction), along with a fit to these points (solid line) and, for comparison, the 1B purity fit (dashed line). Figure D.3 (right) shows the new purity points determined using 1A data with 1B Monte Carlo, along with the resulting fit (solid line). Note that the rederived purity points and resulting fit are about 10-20% higher than the 1A result (the 1A fit is plotted again as a dashed line, for reference). This indicates that the single particle Monte Carlo used in the Run 1A analysis may have underestimated the purity, resulting in a lower cross section.

D.3 Conclusions

In order to estimate the combined effect of these differences, a rough correction of the Run 1A cross sections was made by applying the above factors. To estimate the effect of the EM1 calibration on the 1A data, the Run 1B cross section was calculated without the calibration and a rough parametrization of the difference versus E_T was employed. The resulting ratio of "corrected" 1A to 1B is shown in Figure D.4. While only a reanalysis of the Run 1A data will provide a more exact comparison, the corrected 1A result and the 1B result appear consistent.

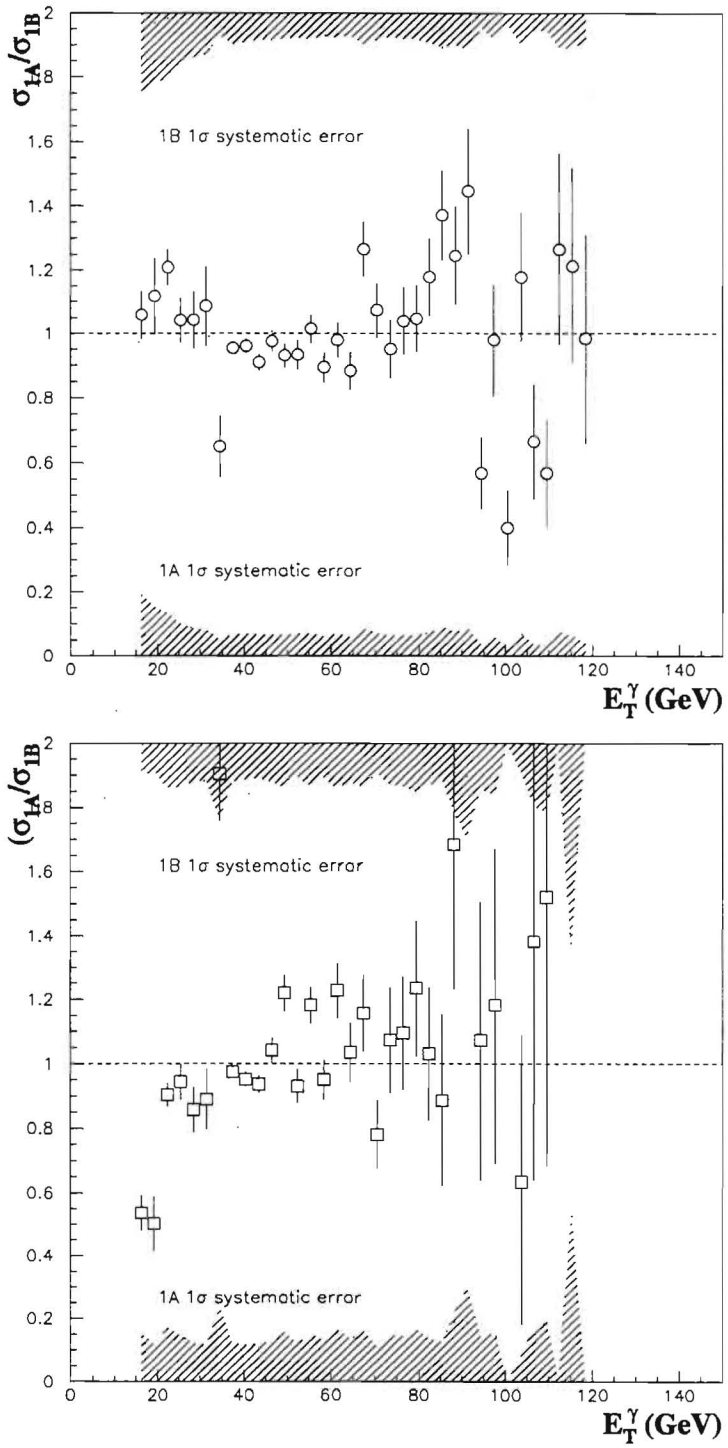

Figure D.4: Ratio of the "corrected" Run 1A inclusive cross sections to the Run 1B results in the central (top) and forward (bottom) regions.

Appendix E

Purity Fits

In the purity fits which follow, the mean E_T of the sample is given by the fit parameter P1, the fit purity as the parameter P2. For clarity, statistical errors are not included on the Monte Carlo points.

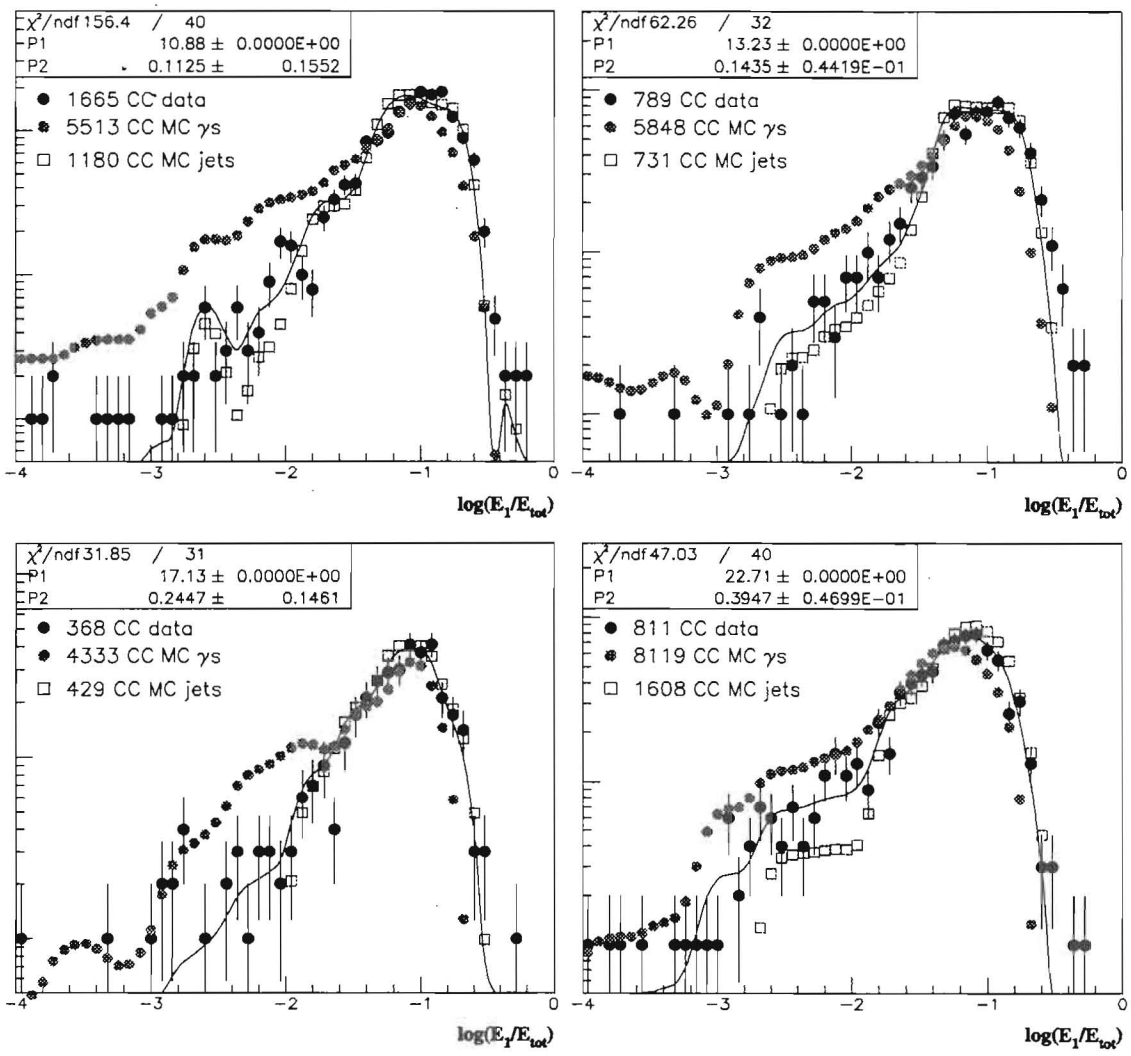

Figure E.1: CC purity fits for E_T bins of 10-12, 12-15, 15-21, and 21-25 GeV.

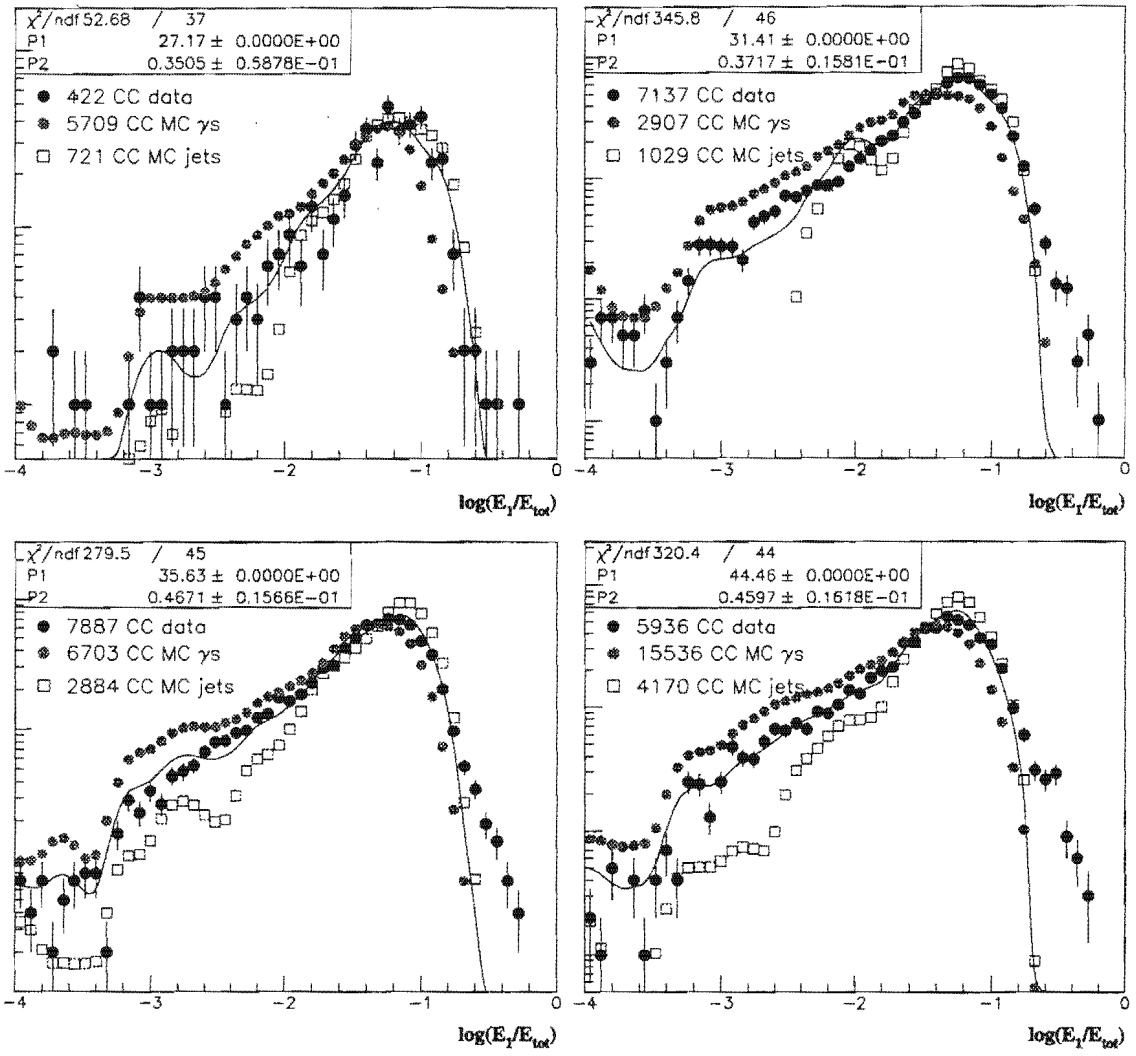

Figure E.2: CC purity fits for E_T bins of 25-30, 30-33, 33-39, and 39-54 GeV.

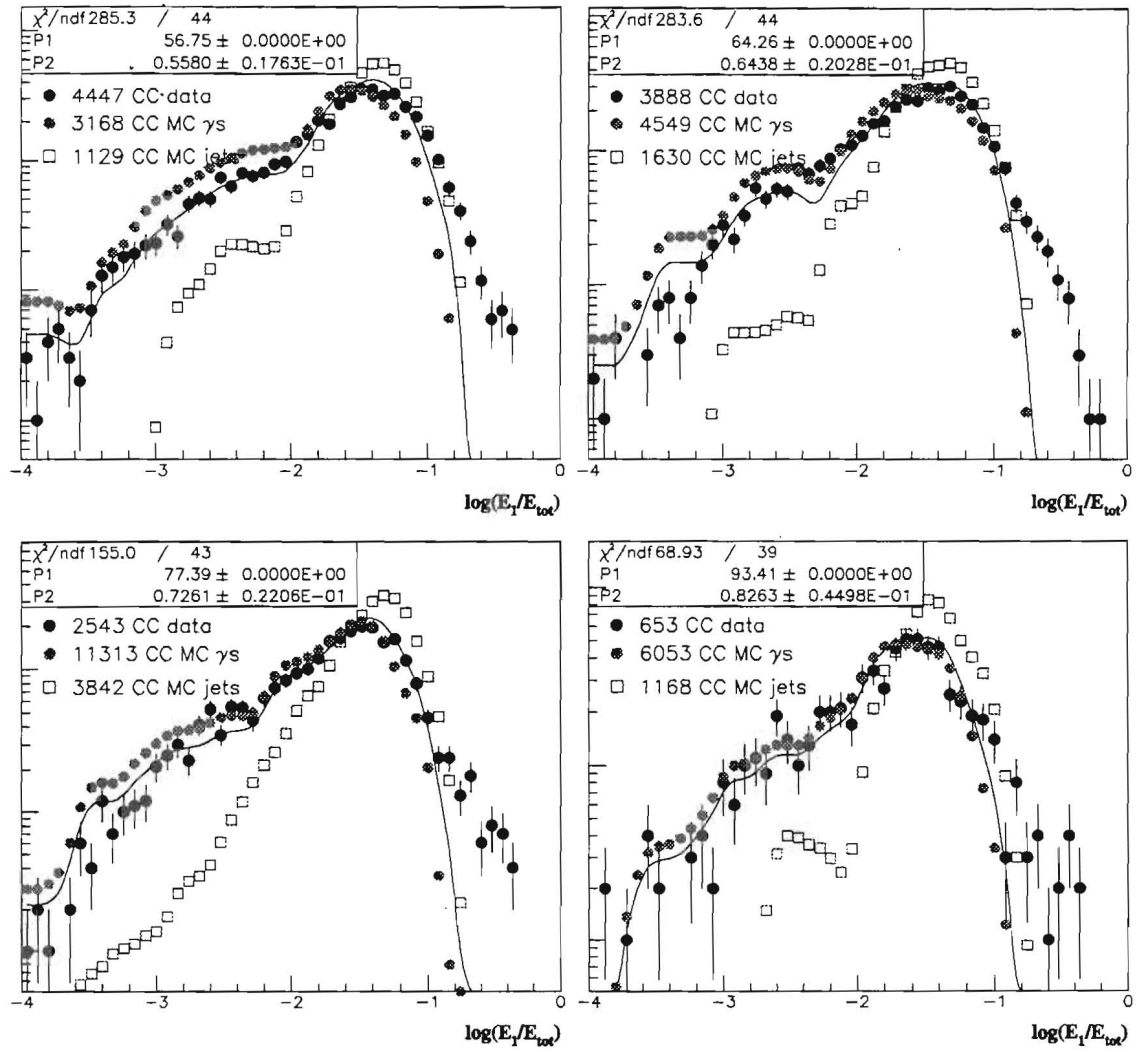

Figure E.3: CC purity fits for E_T bins of 54-60, 60-70, 70-88, and 88-100 GeV.

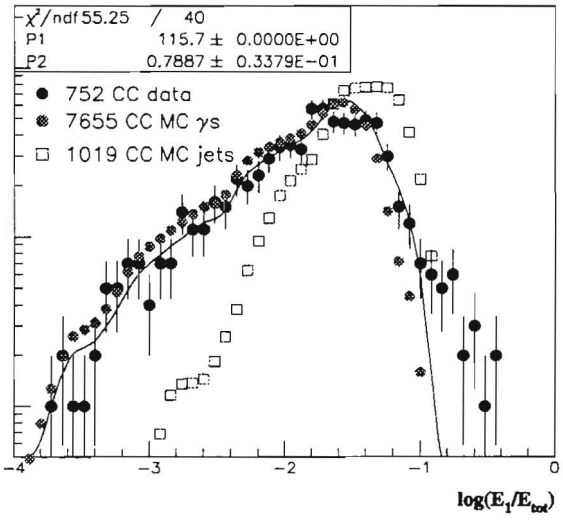

Figure E.4: CC purity fits for the E_T bin of 100-150 GeV.

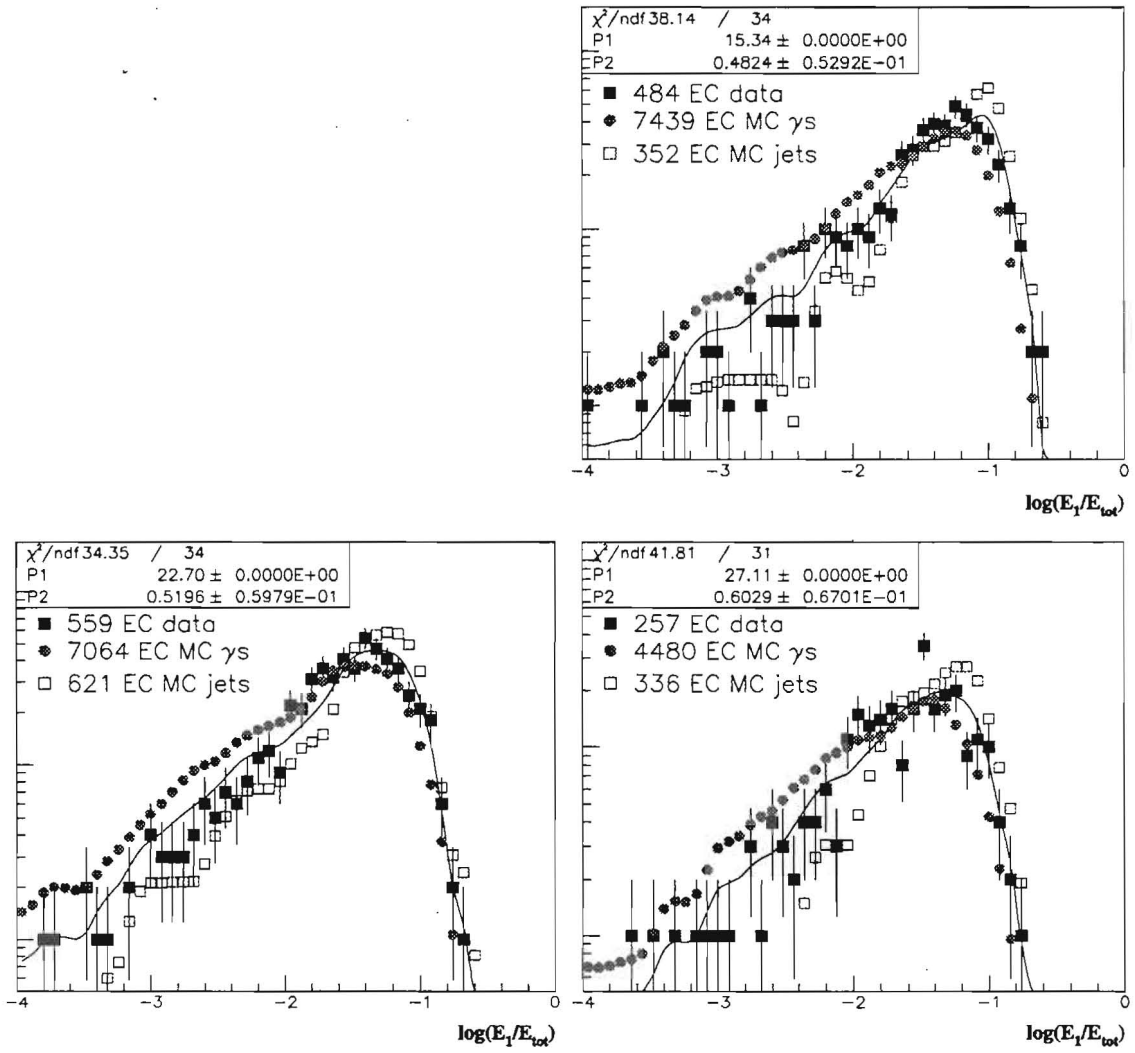

Figure E.5: EC purity fits for E_T bins of 10-13, 13-21, 21-25, and 25-30 GeV.

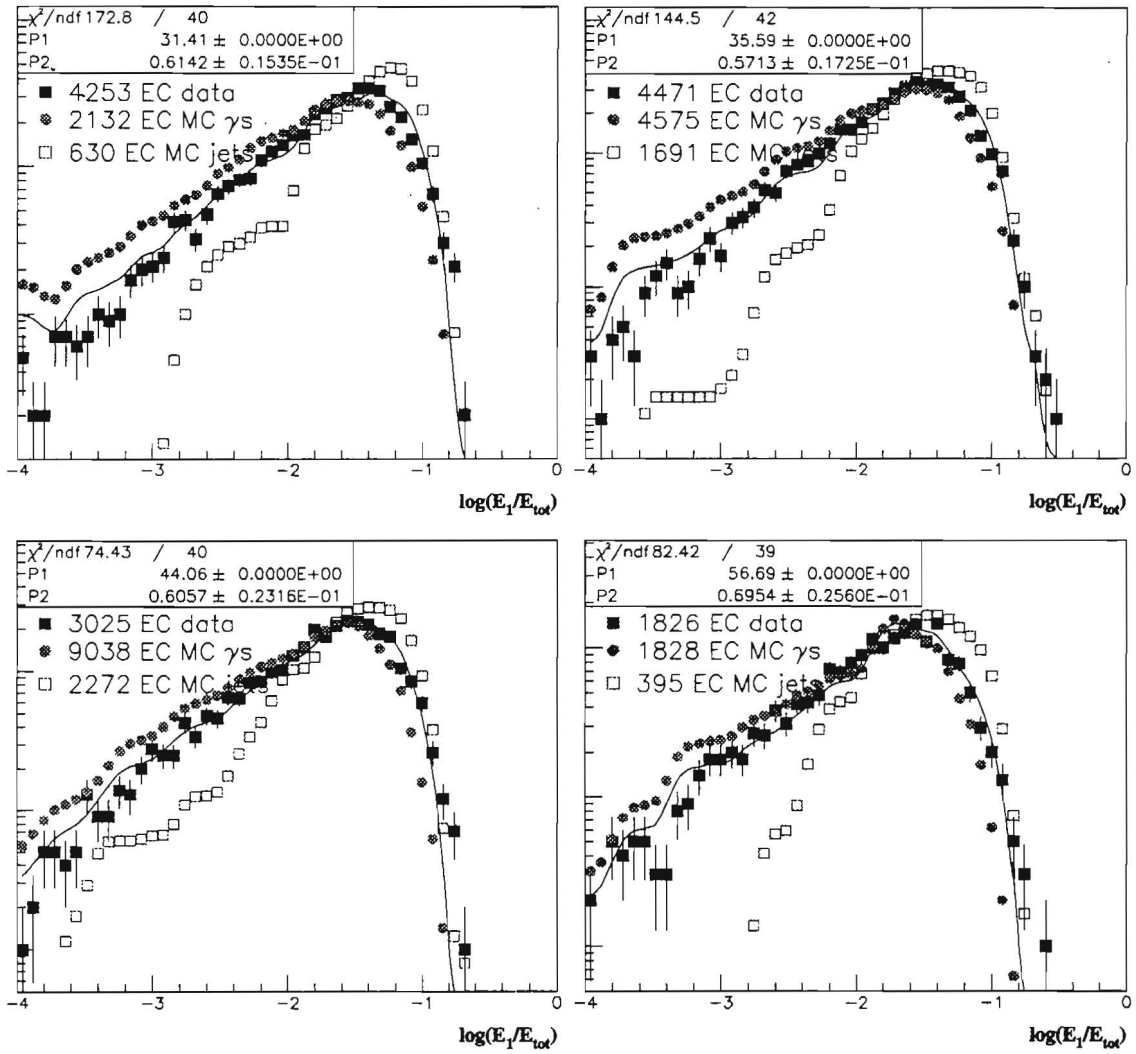

Figure E.6: EC purity fits for E_T bins of 30-33, 33-39, 39-54, and 54-60 GeV.

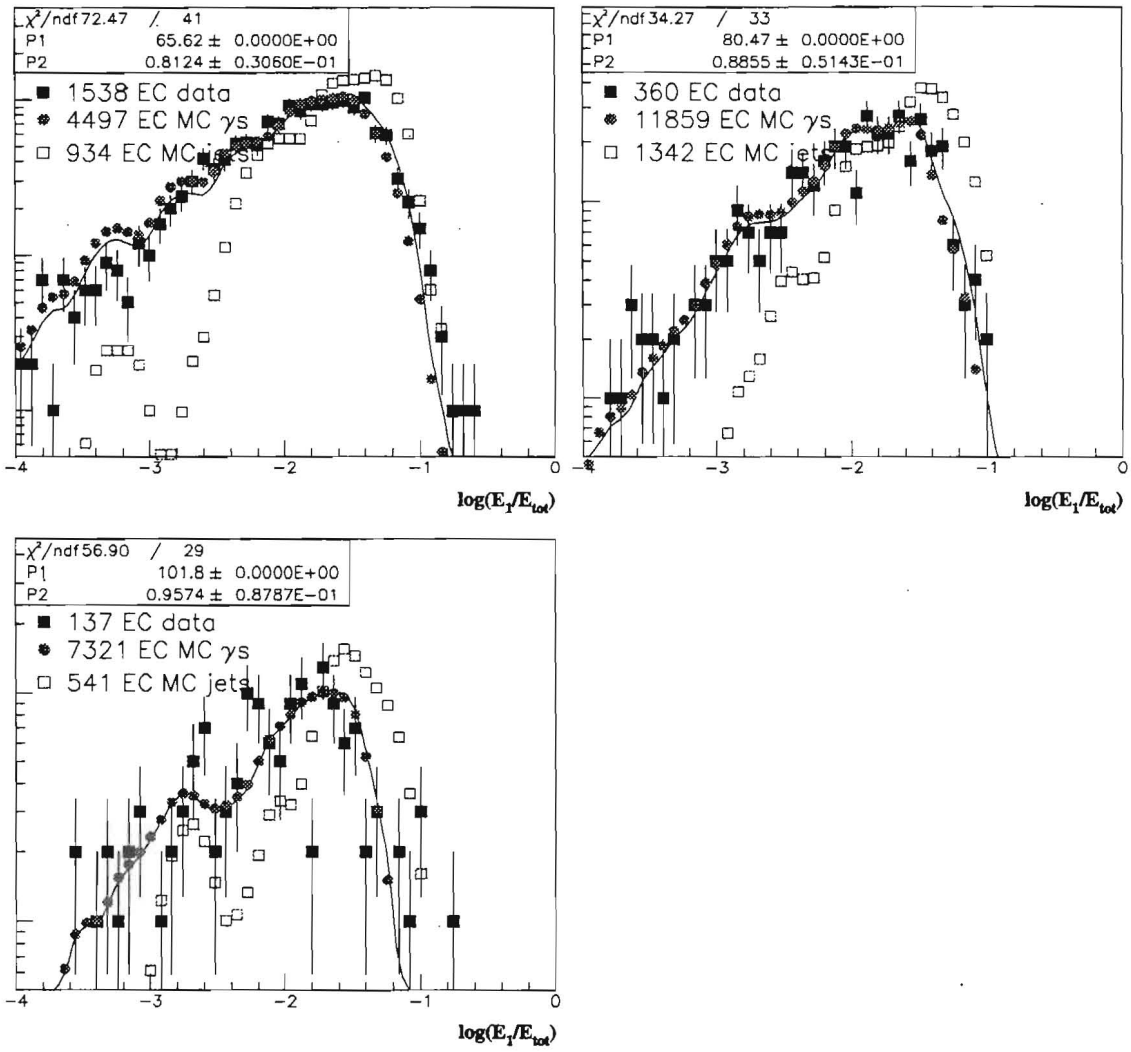

Figure E.7: EC purity fits for E_T bins of 60-75, 75-90, 90-150 GeV.

Appendix F

Monte Carlo Composites

Following are comparisons of data (points) to a composite of Monte Carlo photons and jets (histogram) combined using the purity calculated for each bin. Bins are the same as for the purity calculation in each region.

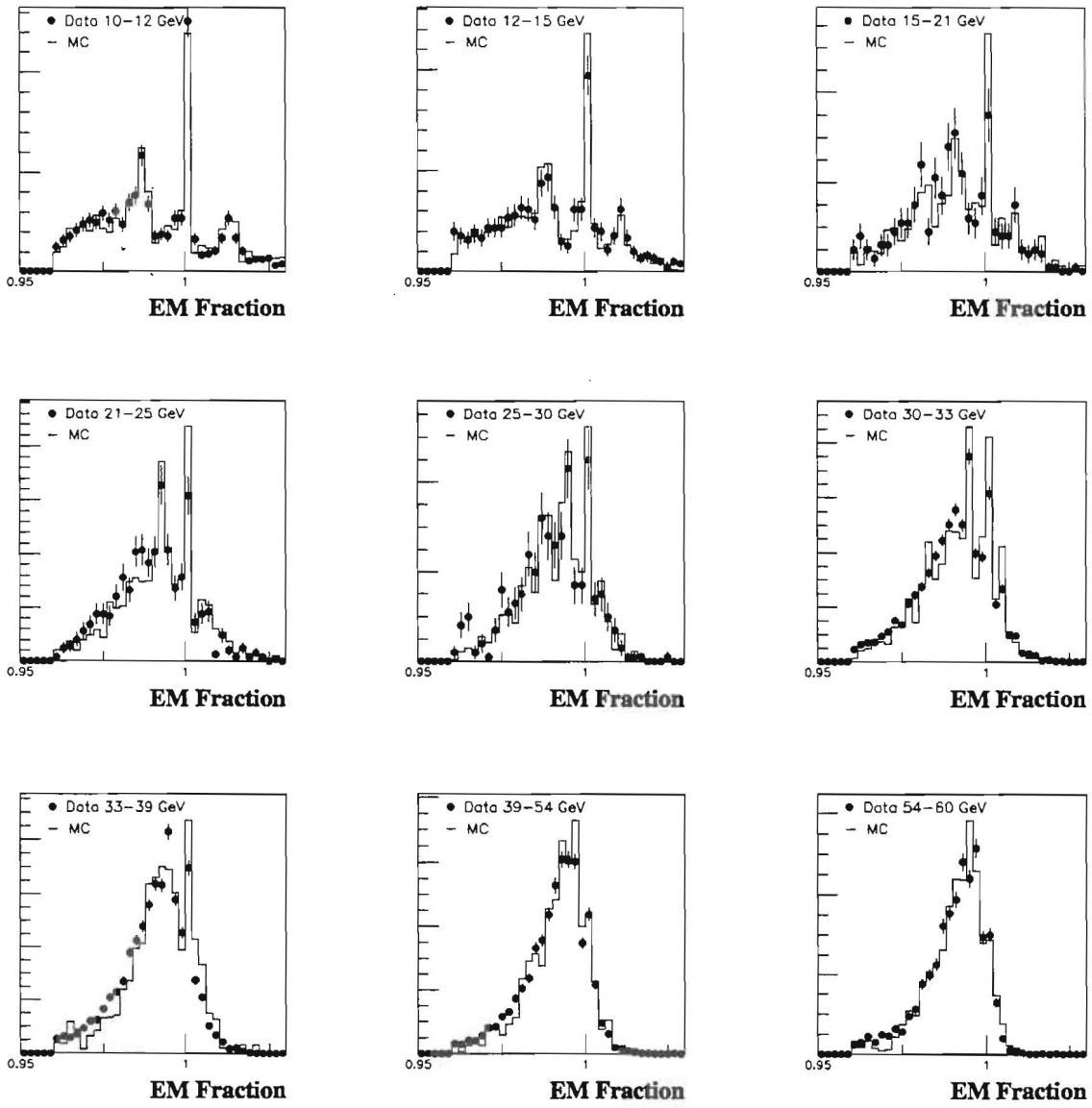

Figure F.1: Comparison of data (points) and composite Monte Carlo (histogram) EM fraction distributions in the central region.

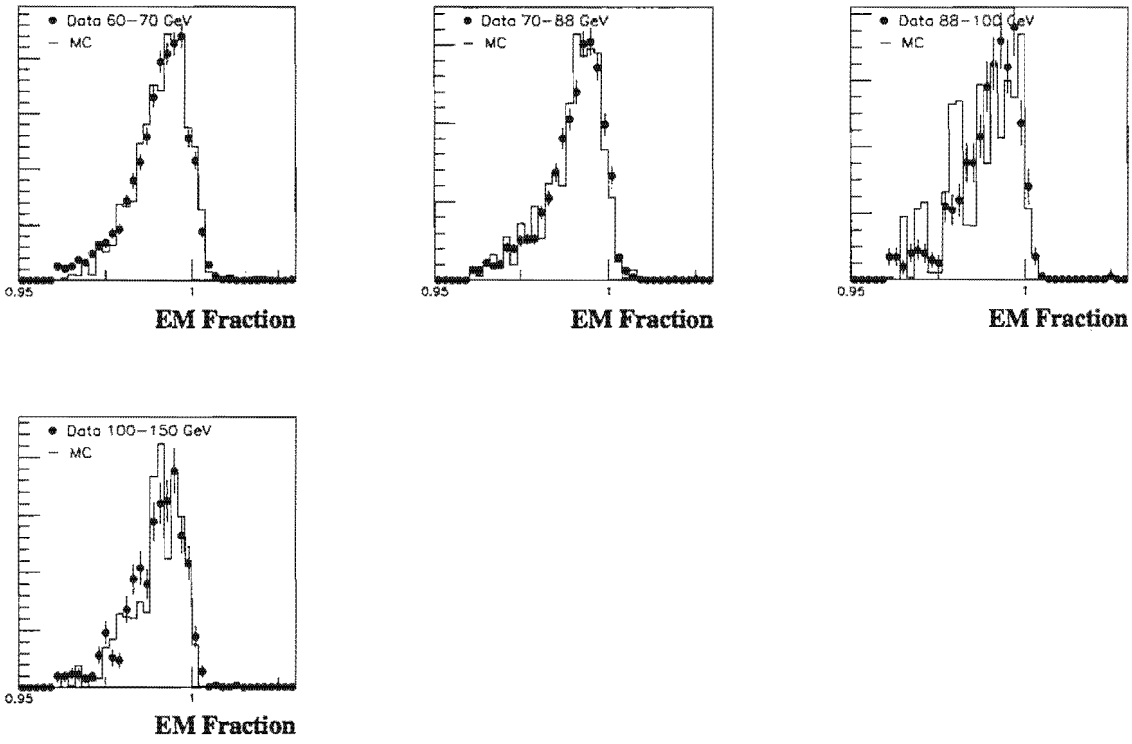

Figure F.1 (cont'd)

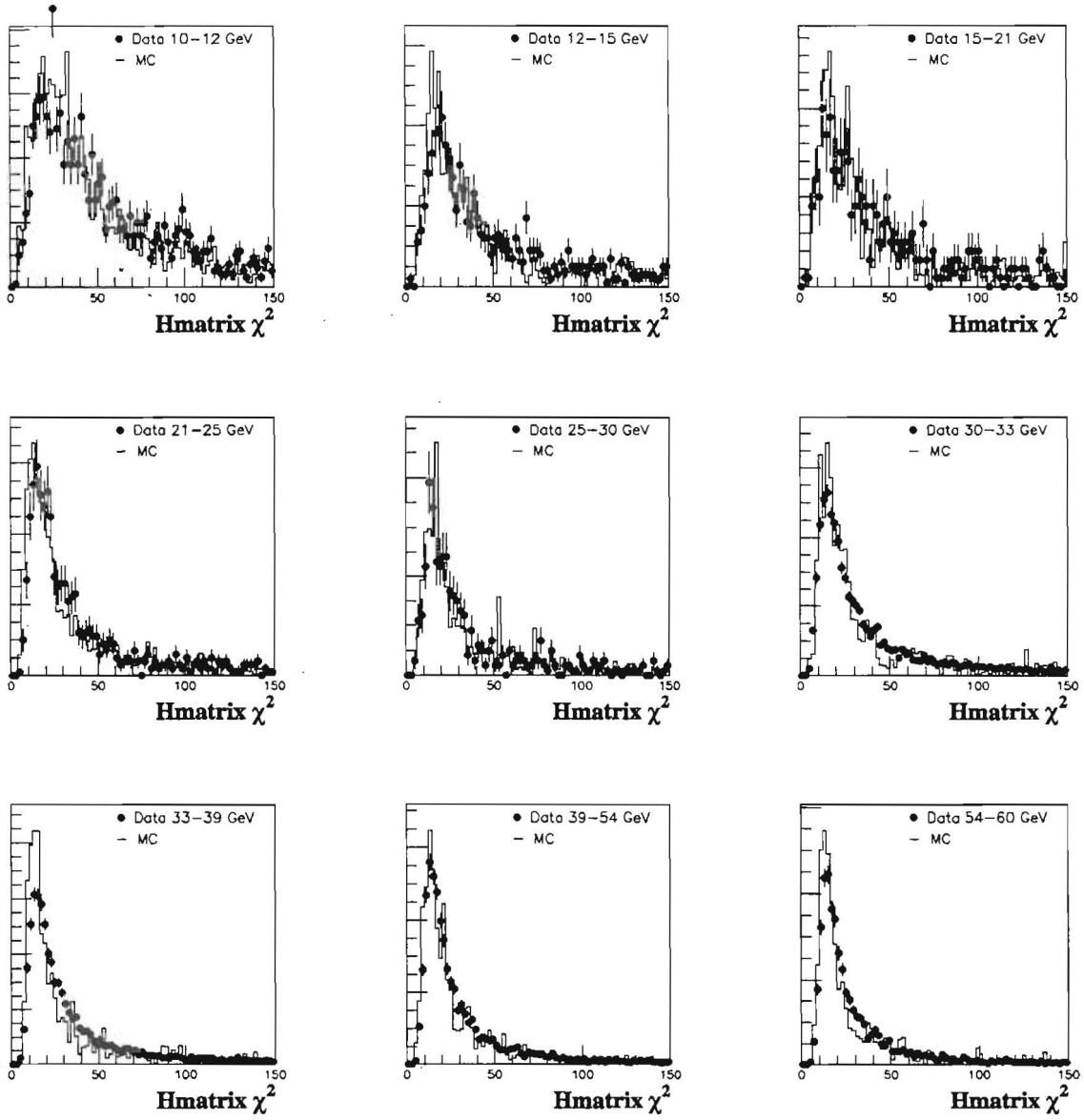

Figure F.2: Comparison of data (points) and composite Monte Carlo (histogram) Hmatrix χ^2 distributions in the central region.

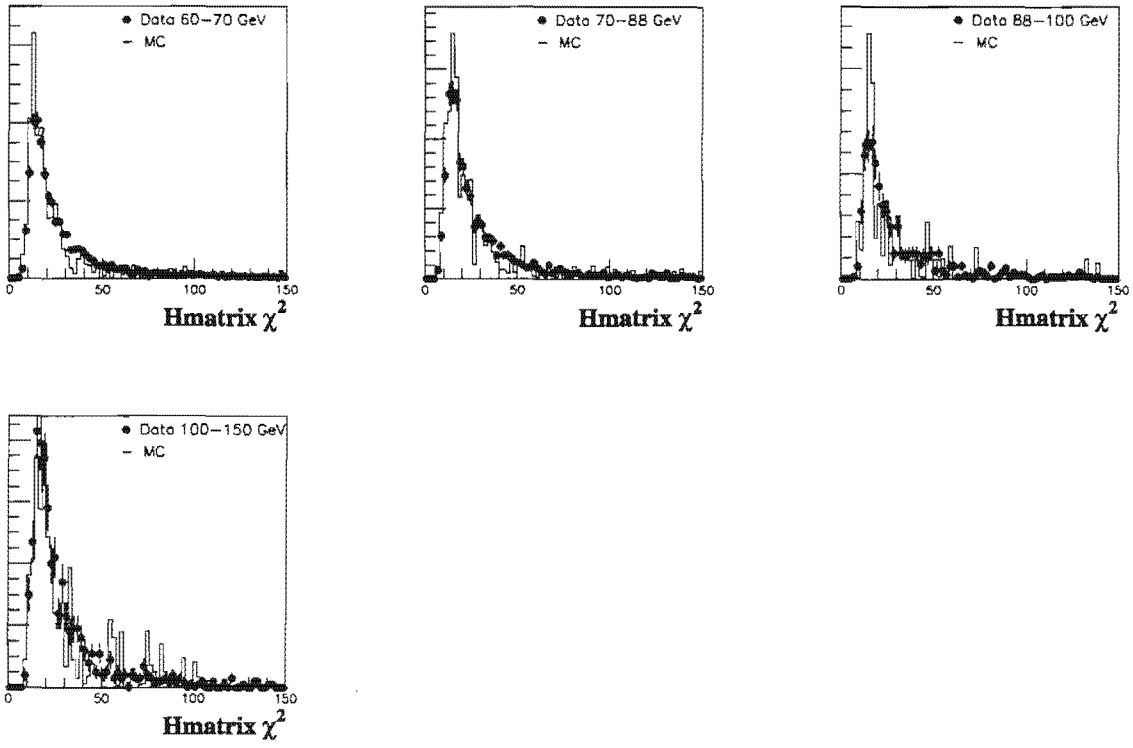

Figure F.2 (cont'd)

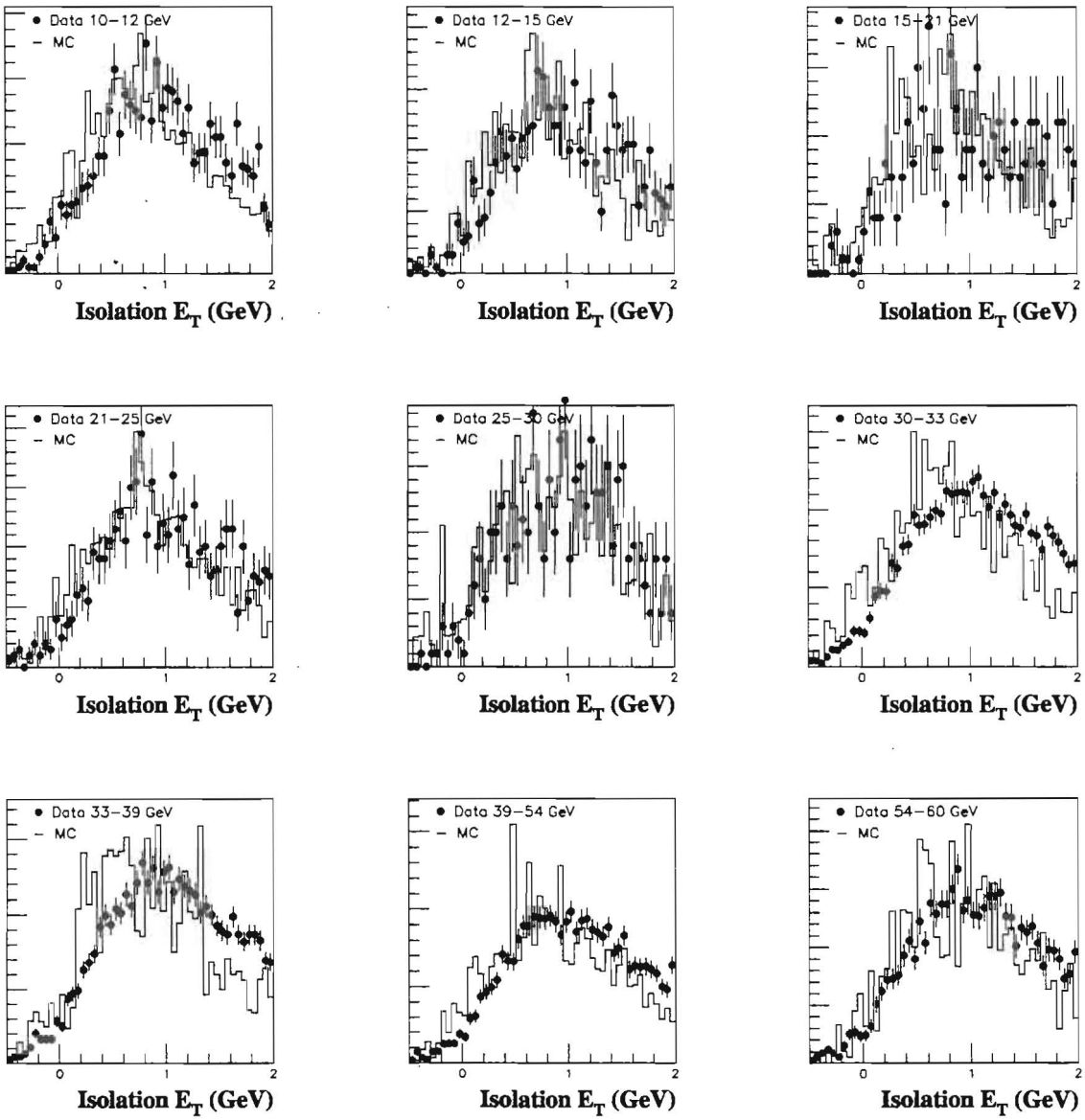

Figure F.3: Comparison of data (points) and composite Monte Carlo (histogram) isolation E_T distributions in the central region.

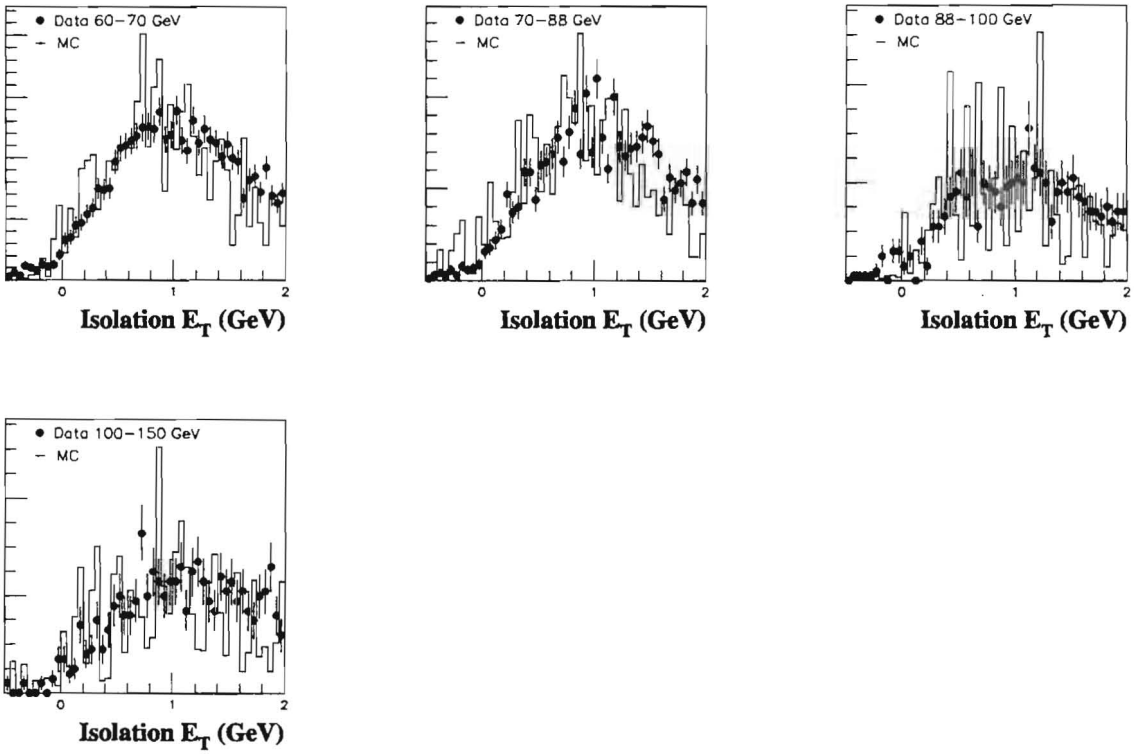

Figure F.3 (cont'd)

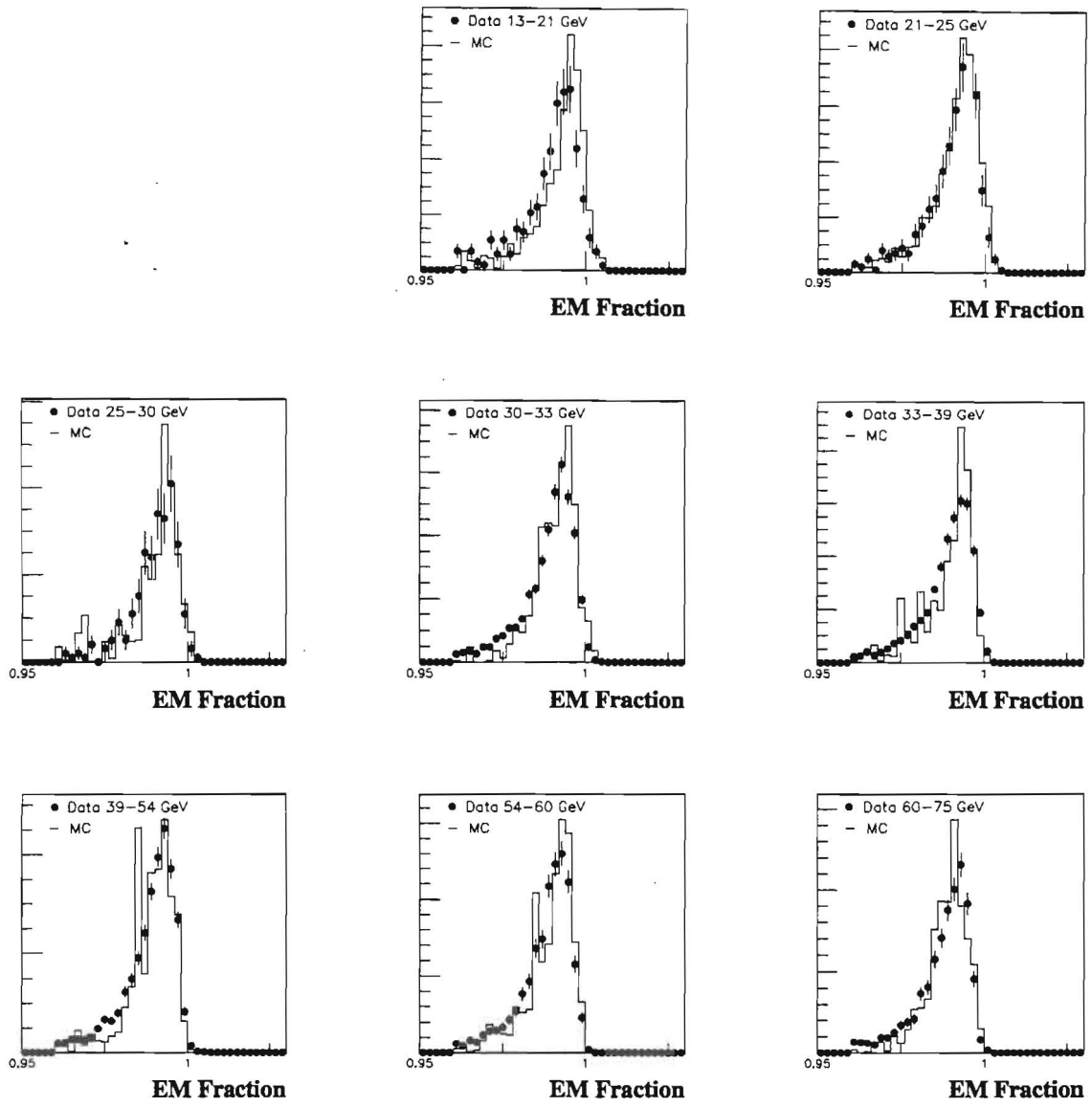

Figure F.4: Comparison of data (points) and composite Monte Carlo (histogram) EM fraction distributions in the forward region.

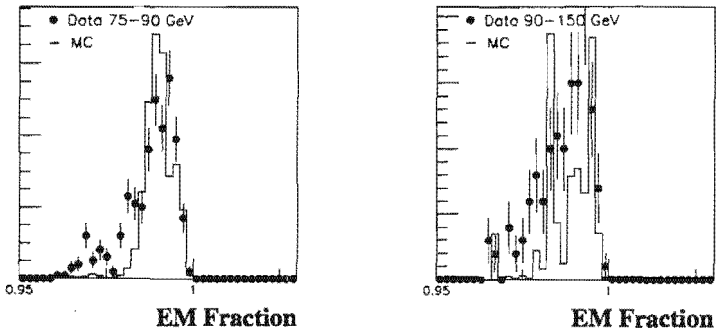

Figure F.4 (cont'd)

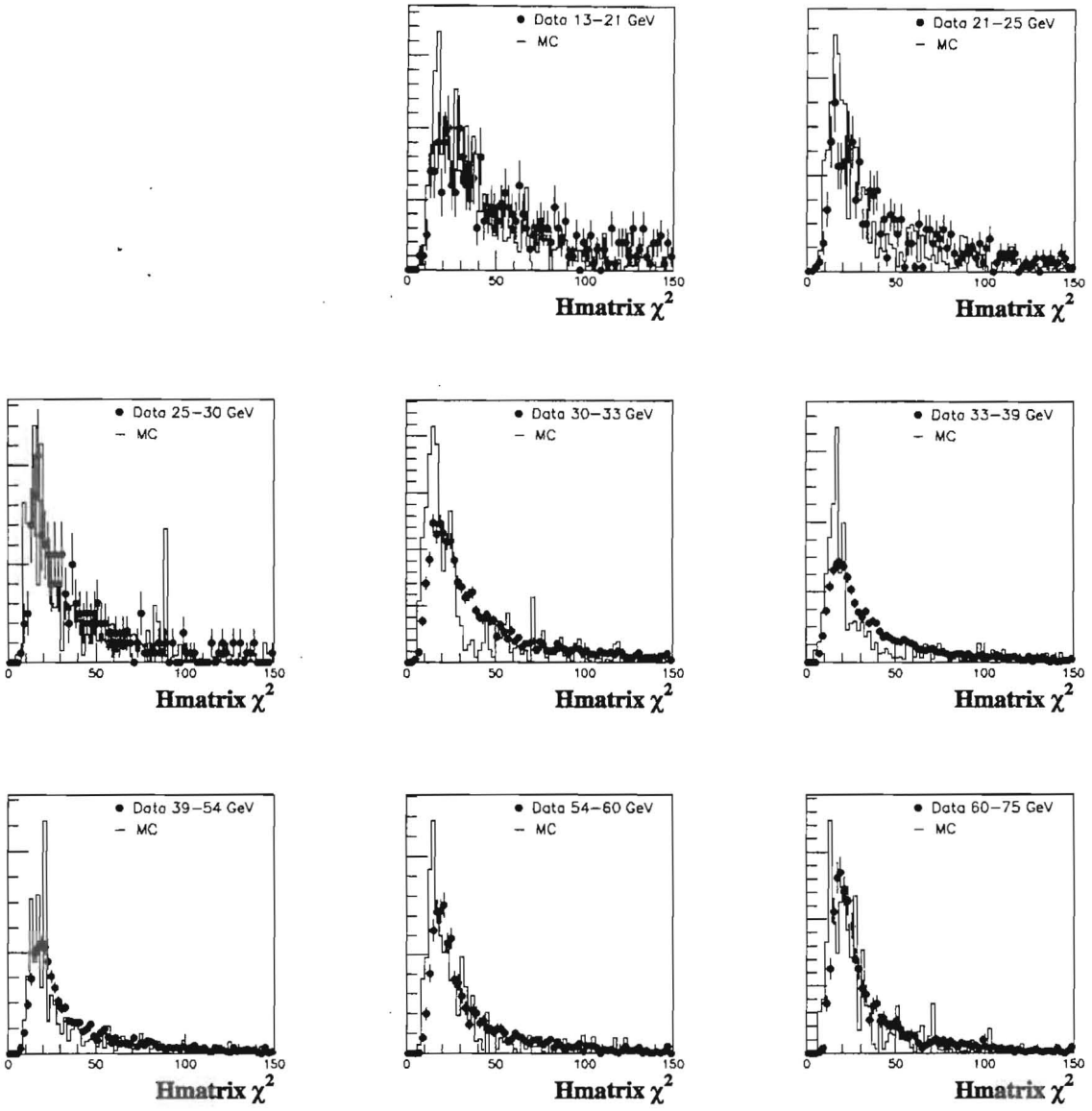

Figure F.5: Comparison of data (points) and composite Monte Carlo (histogram) Hmatrix χ^2 distributions in the forward region.

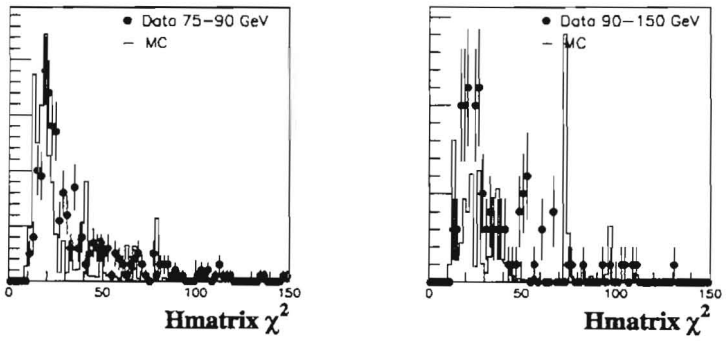

Figure F.5 (cont'd)

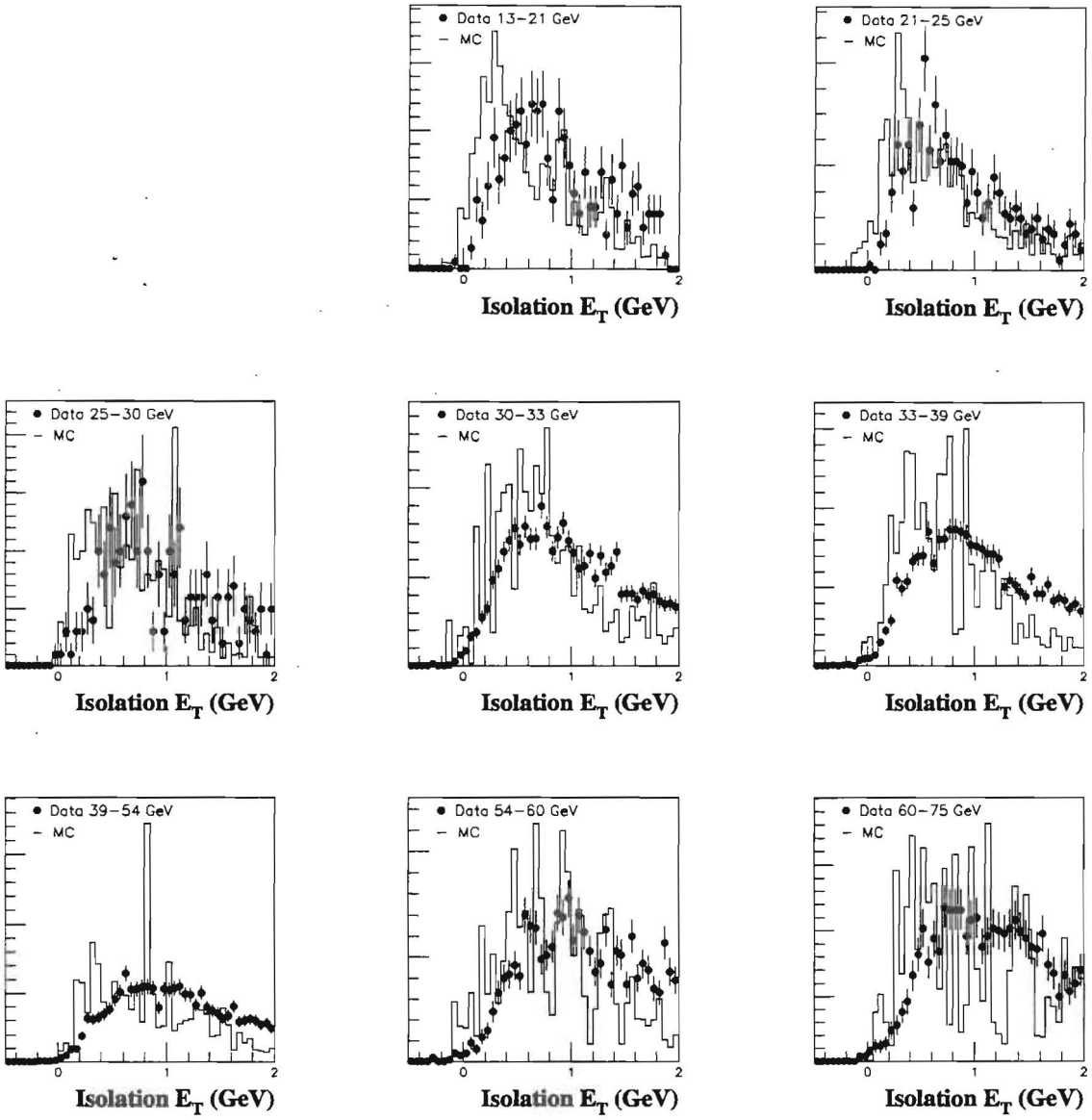

Figure F.6: Comparison of data (points) and composite Monte Carlo (histogram) isolation E_T distributions in the forward region.

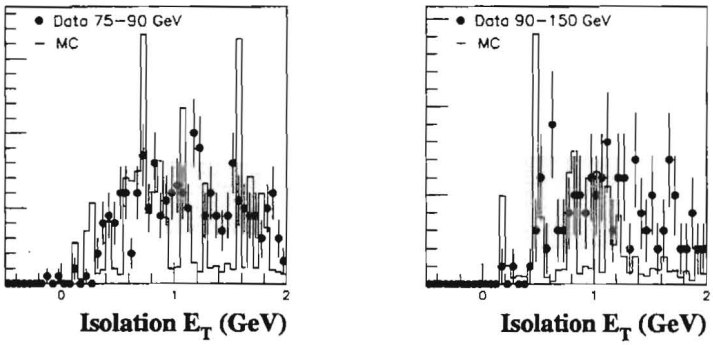

Figure F.6 (cont'd)

REFERENCES

[1] T. Ferbel and W. Molzon, Rev. Mod. Phys. **56**, 181 (1984)

[2] S. Fahey, Ph.D. Thesis, Michigan State University (unpublished) (1995)

[3] S. Abachi, et al., Phys. Rev. Lett. **77**, 5011 (1996)

[4] *Review of Particle Properties*, Physical Review **D54**, Part 1 (July, 1996)

[5] S. Glashow, Nucl. Phys. **22**, 579 (1961);S. Weinberg, Phys. Rev. Lett. **19**, 1264 (1967); A. Salam, in *Elementary Particle Theory*, W. Svartholm, ed., Almquist and Wiksell, Stockholm (1968); J.D. Bjorken, E.A. Paschos, Phys.Rev.**185** 1975 (1969)

[6] I. Hinchcliffe and J. Womersley, FERMILAB-Conf-96/432

[7] E.D. Bloom, et al., Phys. Rev. Lett. **23**, 930 (1969); M. Breidenbach et al., Phys. Rev. Lett. **23**, 935 (1969)

[8] F. J. Hasert, et al., Phys. Lett. **46B**, 138 (1973)

[9] J.J. Aubert, et al., Phys. Rev. Lett. **33**, 1404 (1974); J.E. Augustin, et al., Phys. Rev. Lett. **33**, 1406 (1974); G. Goldhaber, et al., Phys. Rev. Lett. **37**, 255 (1976); S.W. Herb, et al., Phys. Rev. Lett. **29**, 252 (1977); D. Andrews, et al., Phys. Rev. Lett. **45**, 219 (1980)

[10] R. Brandelik, et al., Phys. Lett. **86B**, 243 (1979); D.P. Barber, et al., Phys. Rev. Lett. **43**, 830 (1979); C. Berger, et al., Phys. Lett. **86B**, 418 (1979); W. Bartel, et al., Phys. Lett. **91B**, 142 (1980)

[11] G. Arnison, et al., Phys. Lett. **122B**, 103 (1983); M. Banner, et al., Phys. Lett. **122B** 476 (1983)

[12] S. Abachi, et al., Phys. Rev. Lett. **74**, 2632 (1995); F. Abe, et al., Phys. Rev. **D52**, 2605 (1995)

[13] W. Vogelsang and A. Vogt, Nucl. Phys. **B453**, 334 (1995)

[14] M. Glück, et al, Phys. Rev. Lett. **73**, 388 (1994)

[15] S. Abachi et al, Nucl. Inst. and Meth. **A338**, 185 (1994)

[16] S. Linn, "The Inclusive Cross Section For Isolated Photons in Run 1A," DØ Internal Note 2745 (unpublished) (1995)

[17] M. Abolins, et al., Nucl. Inst. and Meth. **A280** 36 (1989)

[18] A. Spadafora, "Analysis of the Electron Energy Scans from Test Beam Load 1," DØ Internal Note 1378 (unpublished) (1992)

[19] I. M. Adam, Ph.D. Thesis, Columbia University (unpublished) (1997)

[20] M. Narain, et. al, in *Proceedings of the American Physical Society Division of Particles and Fields Conference, Fermilab, 1992*, R. Raja and J. Yoh, ed., World Scientific, Singapore (1993)

[21] C. Shaffer, "The Photon Plus One and Two Jets Cross Section," DØ Internal Note 3104 (unpublished) (1997)

[22] T. Sjöstrand, Comp. Phys. Comm. **82**, 74 (1994)

[23] A. Jonckheere, W. Merritt, "DØGEANT User's Guide," DØ Internal Note 969a (1995)

[24] F. Carminati et. al., *GEANT Users Guide*, CERN Program Library (1991)

[25] H.Baer, J. Ohnemus, and J.F. Owens, Phys Rev. **D42**, 61 (1990)

[26] T. Ferbel and W.R. Molzon, Rev.Mod.Phys. **56**, 181 (1984)

[27] S. Linn, "The Photon Purity in the Central Rapidity Region," DØ Internal Note 2326 (unpublished) (1994)

[28] A. Spadafora, private communication

[29] A. Peryshkin & R. Raja, "On Sampling Fractions and Electron Shower Shapes," DØ Internal Note 1215 (unpublished) (1991)

[30] A. Kotwal, private communication.

[31] H.L. Lai, et al., Phys. Rev. **D55**, 1280 (1997)

[32] CDF Collaboration, F. Abe et al., Phys. Rev. **D48**, 2998 (1993); CDF Collaboration, F. Abe et al., Phys. Rev. Lett. **73**, 2662 (1994)

[33] J. Huston et al., Phys. Rev. **D51**, 6139 (1995)

[34] H.Baer and M. H. Reno, Phys. Rev. **D54**, 2017 (1996)

[35] E. Berger et al., hep-ph/9610497

[36] S. Linn, private communication.

[37] Nang, F., Ph. D. Thesis, Brown University (unpublished) (1996)

[38] McKinley, J. and Linnemann, J., "Description of the Level 2 Electromagnetic Filter Algorithm and Study of the Effects of Shower Generation Method, Zero Suppression, and Event Generation Method on the Level 2 Electromagnetic Filter for D0," DØ Internal Note 1354 (unpublished) (1992)

[39] Bantly, J. et al., "DØ Luminosity Monitor Constant for the 1994-1996 Tevatron Run," Fermilab TM-1995 (1997)

[40] Chopra, S., Heintz U., and Narain, M., "Comparison of Electron ID Efficiencies in Run 1A and Run 1B," DØ Internal Note 2351 (unpublished) (1994)

[41] Melanson, H., "Electron Efficiency Studies," DØ Internal Note (in preparation)

[42] Womersley, J., "Random Charged Track Overlap Probability in the Central and Forward Direct Photon Samples," DØ Internal Note 2106 (unpublished) (1994)

[43] S. Linn, private communication